AD A131252

AFWAL-TR-83-2031

PERMANENT MAGNET GENERATOR ROTOR CONTAINMENT STUDY

GENERAL ELECTRIC COMPANY
P O BOX 5000
BINGHAMTON NEW YORK 13902

MAY 1983

FINAL REPORT FOR PERIOD SEPTEMBER 1980 - NOVEMBER 1982

APPROVED FOR PUBLIC RELEASE; DISTRIBUTION UNLIMITED

AERO PROPULSION LABORATORY
AIR FORCE WRIGHT AERONAUTICAL LABORATORIES
AIR FORCE SYSTEMS COMMAND
WRIGHT-PATTERSON AIR FORCE BASE, OHIO 45433

A

83 08 08 005

20000802025

CR W. U. BORGER
PROJECT ENGINEER
POWER SYSTEMS BRANCH
AEROSPACE POWER DIVISION

DAVID H. SCHORR, MAJOR, USAF
CHIEF, POWER SYSTEMS BRANCH
AEROSPACE POWER DIVISION
AERO PROPULSION LABORATORY

FOR THE COMMANDER

J. D. REAMS
CHIEF, AEROSPACE POWER DIVISION
AERO PROPULSION LABORATORY

REPORT DOCUMENTATION PAGE		READ INSTRUCTIONS BEFORE COMPLETING FORM
1. REPORT NUMBER AFWAL-TR-83-2031	2. GOVT ACCESSION NO. *A131252*	3. RECIPIENT'S CATALOG NUMBER
4. TITLE (and Subtitle) PERMANENT MAGNET GENERATOR ROTOR CONTAINMENT STUDY		5. TYPE OF REPORT & PERIOD COVERED Final Report for Period Sep 80 - Nov 82
		6. PERFORMING ORG. REPORT NUMBER
7. AUTHOR(s) DR. E.U.A. SIDDIQUI		8. CONTRACT OR GRANT NUMBER(s) F33615-80-C-2032
9. PERFORMING ORGANIZATION NAME AND ADDRESS GENERAL ELECTRIC COMPANY P.O. BOX 5000 BINGHAMTON, N.Y. 13902		10. PROGRAM ELEMENT, PROJECT, TASK AREA & WORK UNIT NUMBERS PE 62203F 31452962
11. CONTROLLING OFFICE NAME AND ADDRESS AERO PROPULSION LABOATORY (POO) AIR FORCE WRIGHT AERONAUTICAL LAB, (AFSC) WRIGHT PATTERSON AFB, OHIO 45433		12. REPORT DATE May 1983
		13. NUMBER OF PAGES 142
14. MONITORING AGENCY NAME & ADDRESS(If different from Controlling Office)		15. SECURITY CLASS. (of this report) UNCLASSIFIED
		15a. DECLASSIFICATION/ DOWNGRADING SCHEDULE

16. DISTRIBUTION STATEMENT (of this Report)

APPROVED FOR PUBLIC RELEASE; DISTRIBUTION UNLIMITED.

17. DISTRIBUTION STATEMENT (of the abstract entered in Block 20, if different from Report)

18. SUPPLEMENTARY NOTES

19. KEY WORDS (Continue on reverse side if necessary and identify by block number)

ROTOR CONTAINMENT
VSCF (VARIABLE SPEED CONSTANT FREQ.)
PERMANENT MAGNET
SHRINK RING
BIMETALLIC

20. ABSTRACT (Continue on reverse side if necessary and identify by block number)

THE DESIGN, DEVELOPMENT AND TESTING OF AN ADVANCED CONTAINMENT STRUCTURE FOR HIGH SPEED PERMANENT MAGNET MACHINES IS PRESENTED. THE PRIMARY INTENT OF THE PROGRAM WAS TO ACHIEVE A REDUCTION IN SYSTEM WEIGHT, VOLUME AND COST THROUGH THE USE OF AN IMPROVED CONTAINMENT DESIGN. A SECONDARY OBJECTIVE WAS TO MINIMIZE ROTOR POLE FACE LOSSES AND, THUS IMPROVE GENERATOR EFFICIENCY.

DD _{1 JAN 73} FORM 1473   EDITION OF 1 NOV 65 IS OBSOLETE

20. THE CONTAINMENT STRUCTURE CONSISTS OF A BIMETALLIC SHRINK RING MADE UP OF ALTERNATE MAGNETIC AND NON-MAGNETIC SEGMENTS. IN ORDER TO REDUCE THE ROTOR POLE FACE LOSSES, THE MAGNETIC SEGMENT OF THE SHRINK RING IS CONSTRUCTED FROM THIN LAMINATIONS. AN AMORTISSEUR CIRCUIT COMPRISING OF THREE BARS PER POLE IS INCORPORATED TO REDUCE THE COMMUTATING INDUCTANCE OF THE GENERATOR.

iii/iv

Table of Contents

SECTION I

INTRODUCTION

1.1   OBJECTIVE

The objective of this program was to design, develop and
test an advanced containment structure for high speed permanent
magnet generators used in aircraft power systems. The primary in-
tent of the program was to achieve a reduction in system weight,
volume and cost through the use of an improved containment structure.
A secondary objective of the program was to minimize rotor losses
and thus improve generator efficiency. The containment design was
to be demonstrated in a breadboard generator of 30/40 KVA system
rating having a minimum speed range of 1.7:1. Although the generator
was to be designed for a standard 115V, 3 phases, 400 Hz aircraft
power system, the program did not entail the development of the
associated frequency conversion circuitry.

This program is part of a series of Air Force programs
directed towards the development of light weight, low cost, high
performance motors and generators for advanced aerospace applications.
Over the past decade, the availability of high strength Samarium
Cobalt magnets has enabled permanent magnet machines to equal con-
ventional wound rotor machines from a weight standpoint while offering
substantial gains in efficiency and electrical performance. The Air
Force recognized the potential of permanent magnet machines and spon-
sored several development programs. The first contract F33615-74-C-
2037 was awarded to General Electric Company for the development of
a 150 KVA permanent magnet VSCF starter generator system. This
generator was designed with Samarium Cobalt magnets which were retain-
ed in compression by a bimetallic shrink ring. Although the electro-
magnetic and mechanical performance of this ring were adequate, it
was difficult to produce because of the need for cold working to
attain desirable material properties.

1

The successful completion of the 150 KVA program led to another contract (F33615-78-C-2200) to General Electric Company for a 60 KVA VSCF starter generator system. The materials selected for the bimettalic shrink ring obviated cold working which was an improvement from a producibility standpoint. In continuation, this program was initiated to further advance the state-of-the-art and yield weight, volume and performance gains over permanent magnet generators that employ present day containment methods.

1.2 SCOPE

The objectives of this program were accomplished in three consecutive phases:

Phase I-Design

In this phase the containment structure was designed to achieve optimization of the total system. The factors considered were:

a) system requirements of generator output and commutating inductance.

b) generator requirements of weight, volume, rotor losses and thermal capabilities.

c) rotor dynamics, stresses and critical speed characteristics.

d) containment structure producibility and reliability.

After the selection of the containment structure was made, the rotor and stator were designed in detail. Advanced analytic techniques were employed to insure the validity of the design and predict the generator performance.

A rotor spin test fixture was also designed for evaluation of the rotor integrity. The fixture contained bearings and a lubrication system and was designed to provide heating to achieve the maximum temperature preducted for full load generator operation. The fixture had the capability of containing the rotor in the event of rotor mechanical failure.

2

The final task of this phase was the experimental verification of all critical parameters of the containment design. A considerable amount of component development work was done to determine the producibility of the containment design and to insure that the mechanical requirements would be met. The successful completion of this task reduced the risk of the program and guaranteed success.

Phase I was completed in 9 months.

Phase II - Rotor Fabrication and Spin Test

Three separate tasks were accomplished as part of this phase. These were:

a) fabrication of the rotor and the spin test fixture.
b) establishment of the generator test procedure for Phase III.
c) 50 hour comprehensive rotor test.

After the fabrication of the rotor and the spin test fixture were completed, the rotor was assembled in the fixture and provisions were made for monitoring oil flows and temperatures and the outboard vibrational level of the unit. Some adjustments to the oil flow were required to achieve the desired temperature of the unit. The rotor was spun for 64 hours at maximum speed with a 5 minute excursion to overspeed. The rotor was very stable throughout the speed range and no resonances occurred. At the conclusion of the test, the rotor was disassembled and inspected. No changes in dimensions or rotor balance were noted.

Phase II was completed in 10 months.

Phase III-Stator Fabrication and Generator Test

The tasks completed in this phase were:

a) fabrication of the stator.

b) test of the generator.

Since all the rotor components had been fabricated in the previous phase of the program, only the stator parts were built in this phase. The generator was assembled and tested according to the test plan established in Phase II.

The design of all generator components and the materials selected were such as to yiled an apparatus suitable for aerospace application. The quality assurance program was that adopted for hardware fabricated for research purposes. The hazards of testing this high rpm machine were assessed and frame was designed to contain the rotor in the event of a failure.

Phase III was completed in 8 months.

1.3   SUMMARY

All objectives of the program were acccmplished as outlined in the previous section. The containment structure, shown in Figure 1.1 is an extension of the type used in the 60 KVA program (USAF Contract F33615-78-C-2200). The magnets are retained in compression by the bimetallic shrink ring made up of alternate magnetic and non-magnetic segments welded together. In order to reduce the rotor pole face losses, the magnetic segment of the shrink ring is constructed from thin laminations. The amortisseur circuit comprising of three bars per pole is incorporated to reduce the commutating inductance of the generator and, thus, improve system performance. This containment design presents the best balance between the factors taken into account. It offers to reduce the system weight and volume while improving the electrical performance.

A great deal of component work was performed in Phase I to insure the producibility of the shrink ring. Since the design required

4
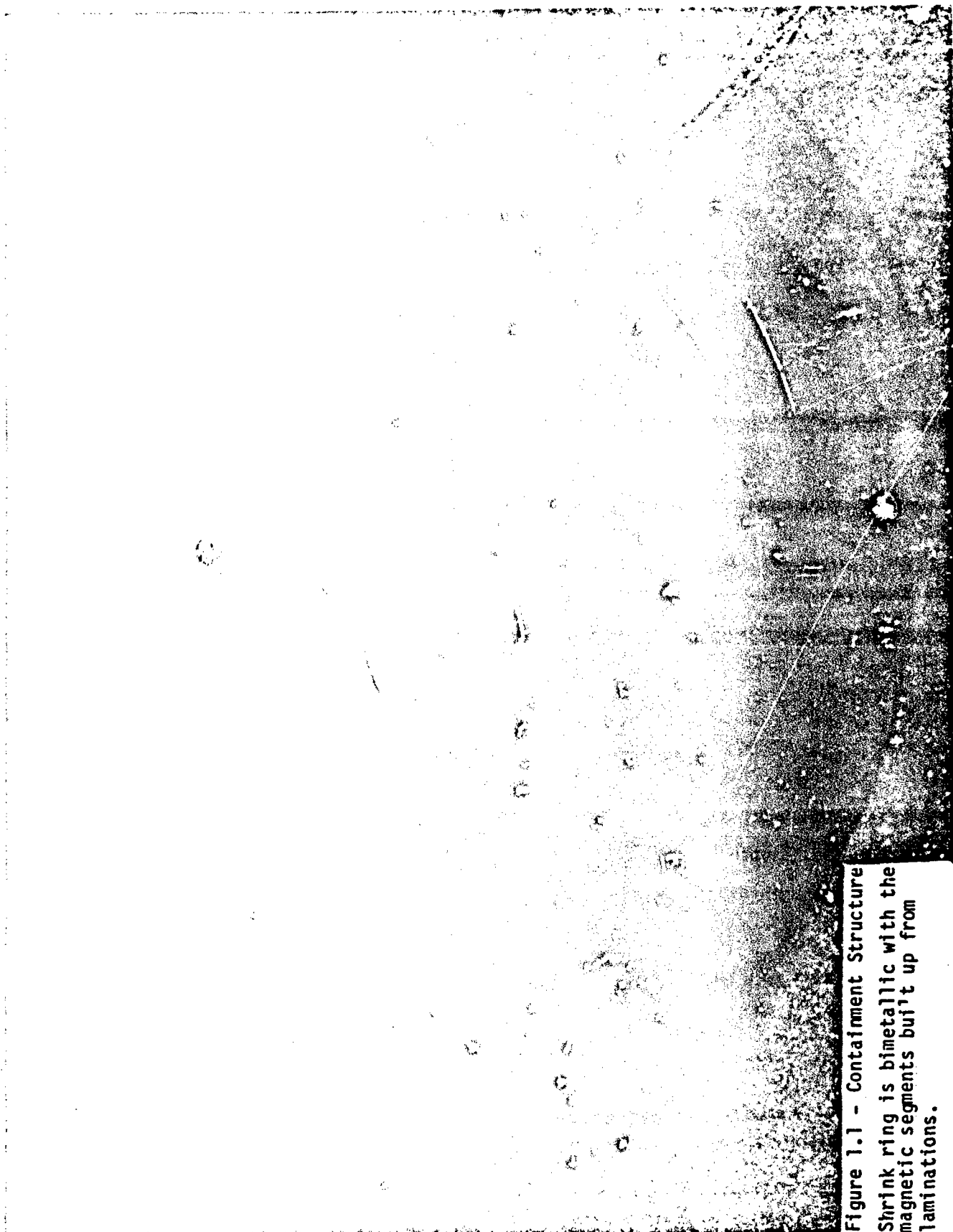
Figure 1.1 - Containment Structure

Shrink ring is bimetallic with the magnetic segments built up from laminations.

laminations being welded to solid pieces, a major concern was the tensile strength of the weld. Several tensile samples were made and tested. The results of the test indicated that the yield strength would be much above the maximum stress that would be realized in operation. A second concern was the lineup of the amortisseur holes of the three rotor discs to permit easy insertion of the amortisseur bars. A simple fixture designed to position the discs using the amortisseur holes during the surface and bore grinding guaranteed the lineup of the holes. In short, all development work required to re-duce the risk of the program was completed in Phase I.

The rotor consists of three discs shrunk on the shaft as shown in Figure 1.2. The stator and the rotor are assembled inside a F-18 frame for testing purposes. The bearings, high speed seals and shear disconnect are proven technology having been used on other VSCF systems.

During the generator testing, the system load at the specified power factor was provided by a linear load bank. In order to determine the efficiency of the generator; a 100 in-lb torque tube was used. The ratings used for the generator are given in Table 1.

Table 1
Generating Rating

SYSTEM LOAD	GEN. CURRENT PER PHASE	GEN. PF
0 PU	27 A	0.1
½ PU	40 A	0.75
1 PU	47 A	0.74
1 PU	57 A	0.76
1½ PU	53 A	0.74
1½ PU	63 A	0.78
2 PU	74 A	0.74
2 PU	83 A	0.83

The input power to the generator was measured at various speeds and load conditions using the torque tube. While the input power at load was measured at base speeds, no load input power was measured at speeds of upto 21,000 rpm. Some of the efficiency data is given in Table 2.
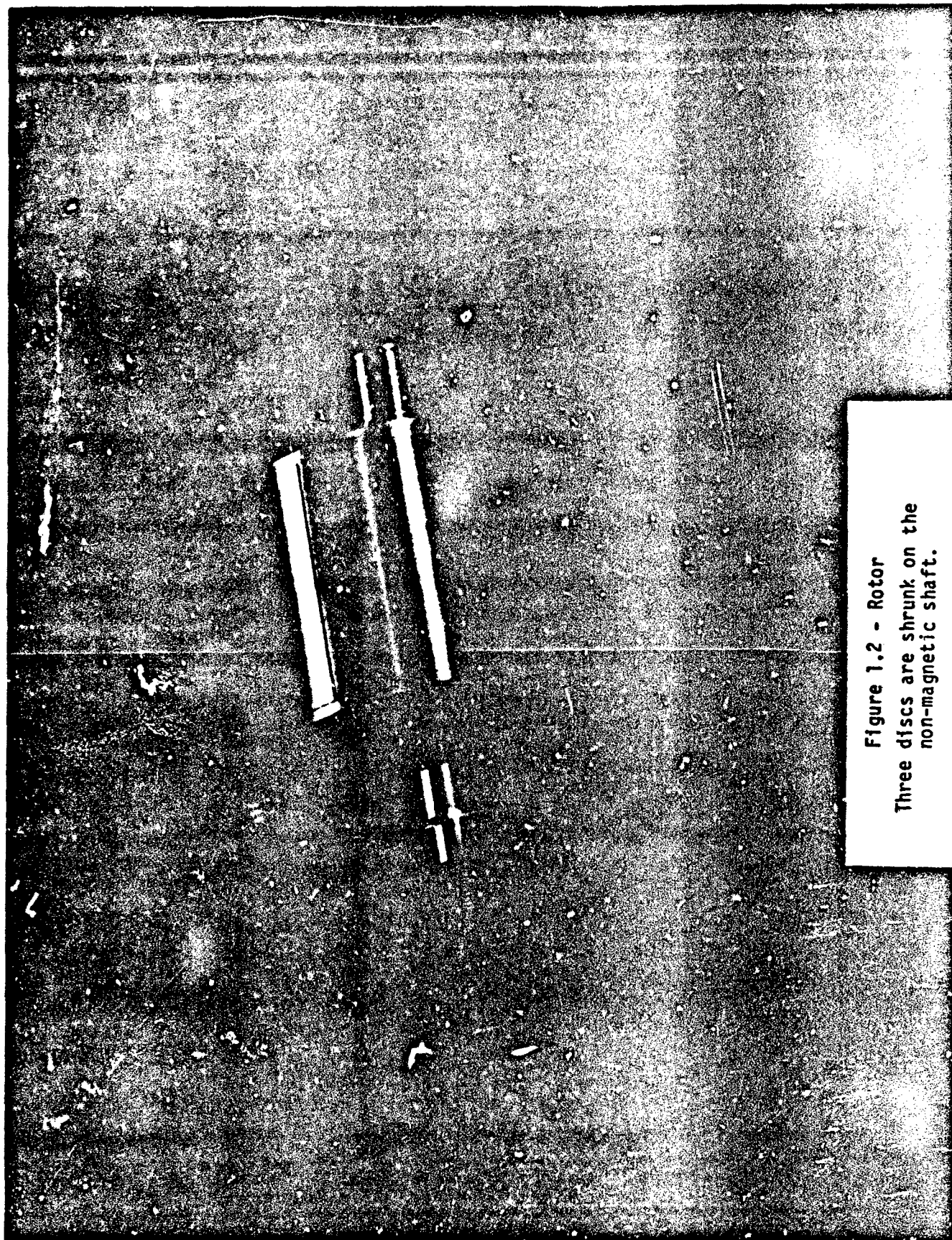
Figure 1.2 - Rotor
Three discs are shrunk on the non-magnetic shaft.

Table 2
Generator Efficiency
(15,300 RPM)

GEN. KVA	PF	GEN. KW	INPUT KW	EFF.
45.6	.757	34.5	36.8	0.94
52.2	.742	38.8	41.1	0.94
61.1	.766	46.8	50.2	0.93

The rotor pole face losses depend on the stator slot opening, air gap and the materials used. These factors were considered in minimizing the pole face losses. Table 3 shows that these losses were reduced by approximately 40% if compared to the solid segment design.

Table 3
Rotor Pole Face Losses
(Computed)

SYSTEM KVA	LOSSES-POLE SEGMENTS	
	LAMINATED	SOLID
40	0.57	1.0
45	0.59	1.0
60	0.60	1.0

The weight of the generator package is 39.5 lbs. distributed as follows:

Rotor	18.44 lbs.
Stator	11.00 lbs.
Assy. Comp.	7.81 lbs.
	37.25 lbs.
Disconnect	2.25 lbs.
Total Package	39.50 lbs.

Since an existing stator frame was utilized, the packaging of the generator is not optimized from a weight standpoint. It is estimated that a 2.0 lb. reduction is possible in the anti-drive end bell and the disconnect components. Further reduction in weight and volume can be realized by designing a new stator frame and the required housing.

In summary, this program reflects an advancement in the containment technology for high speed permanent magnet machines. The rotor pole face losses are significantly reduced and the lower commutating inductance will reduce the losses in the converter during commutation thus improving the overall system efficiency.

SECTION II

DESIGN CONCEPTS

2.1 BACKGROUND

A variable speed constant frequency (VSCF) generator is a high speed, high frequency synchronous machine. The conventional generator design is composed of a main synchronous generator, an exciter, and a permanent magnet "pilot" generator. The main generator is a wound rotor, salient pole, brushless machine whose output is fed into a static cycloconverter. The exciter is an inside out synchronous main generator field. The pilot generator supplies power to the exciter and system controls.

Although permanent magnet generators have been used in power systems, their function has been limited to providing excitation for the exciter and power for the system controls. The availability of high strength Samarium Cobalt magnets has, however, rendered permanent magnet generators a viable alternative to the wound rotor generators. The use of the permanent magnet generator eliminates the pilot generator, exciter and the rectifiers. This significantly reduces the parts count and improves the reliability of the system.

The negative aspects of permanent magnets have been eliminated with the advent of rare earth Samarium Cobalt magnets. These magnets exhibit an almost ideal magnetization curve and provide high energy product in conjunction with a high coercive force. These characteristics permit optimization of the generator with respect to the overall performance. A relatively small portion of the rotor volume is occupied by the magnets thus allowing a larger amount of volume for mechanical support.

Figure 2.1 is a block diagram of a VSCF system using a permanent magnet machine. At the center of the page is the main power path from the

10

Figure 2.1 - Block diagram of a VSCF system comprising a permanent magnet generator.

11

PMG through the converter and filter to the 400 Hz terminals. In the generator mode, six or nine phase variable frequency, variable voltage power from the PMG is converted to three phase, 400 Hz power at 115 volts. The voltage output of the PMG does not affect the system output as long as it is above a minimum value to avoid saturation of the amplifiers. The converter SCR's are programmed such that the average value of the voltage selected from each generator phase is that required to provide the 115 V output.

At higher speeds where the generator voltage is much greater than that required to develop the system output, the average retard of the SCR's is increased. This causes additional losses in the snubbers and the interphase transformers (IPT). The snubbers which limit the dv/dt of the SCR's have, for a contant value of dv/dt, losses approximately proportional to the fourth power of voltage for a fixed machine commutating inductance and frequency. Thus, snubber losses might approach several kilowatts for the PMG system at maximum speed and no load. These losses have to be taken into account to determine system efficiency.

The key to an efficient, trouble free operation of a high speed generator lies in the magnet containment. Since the density of rare earth magnets is high, a considerable centrifugal force has to be borne by the shrink ring. The magnitude of this centrifual force can be estimated by idealizing the poles and magnets to be an annulus of uniform density and thus

$$F_c = \frac{2\pi\rho\omega^2}{gc}\int_{r_i}^{r_o} r\ dr$$

where F_c is the centrifugal force on a unit length basis. For a 5" OD rotor as shown in Figure 2.2, F_c is in the vicinity of 125,000 lbs/in at 28,900 rpm and would govern the dimensions of the shrink ring. However, with the poles solidly attached to the hub by a process like electron beam welding, a portion of the pole centrifugal force is borne by the hub.

12

PERMANENT MAGNET
MAGNETIZATION DIRECTION

NON-MAGNETIC
MEMBER

BIMETALLIC
SHRINK
RING

PERMANENT
MAGNET

MAGNETIC
MEMBER

HUB
(NON-MAGNETIC)

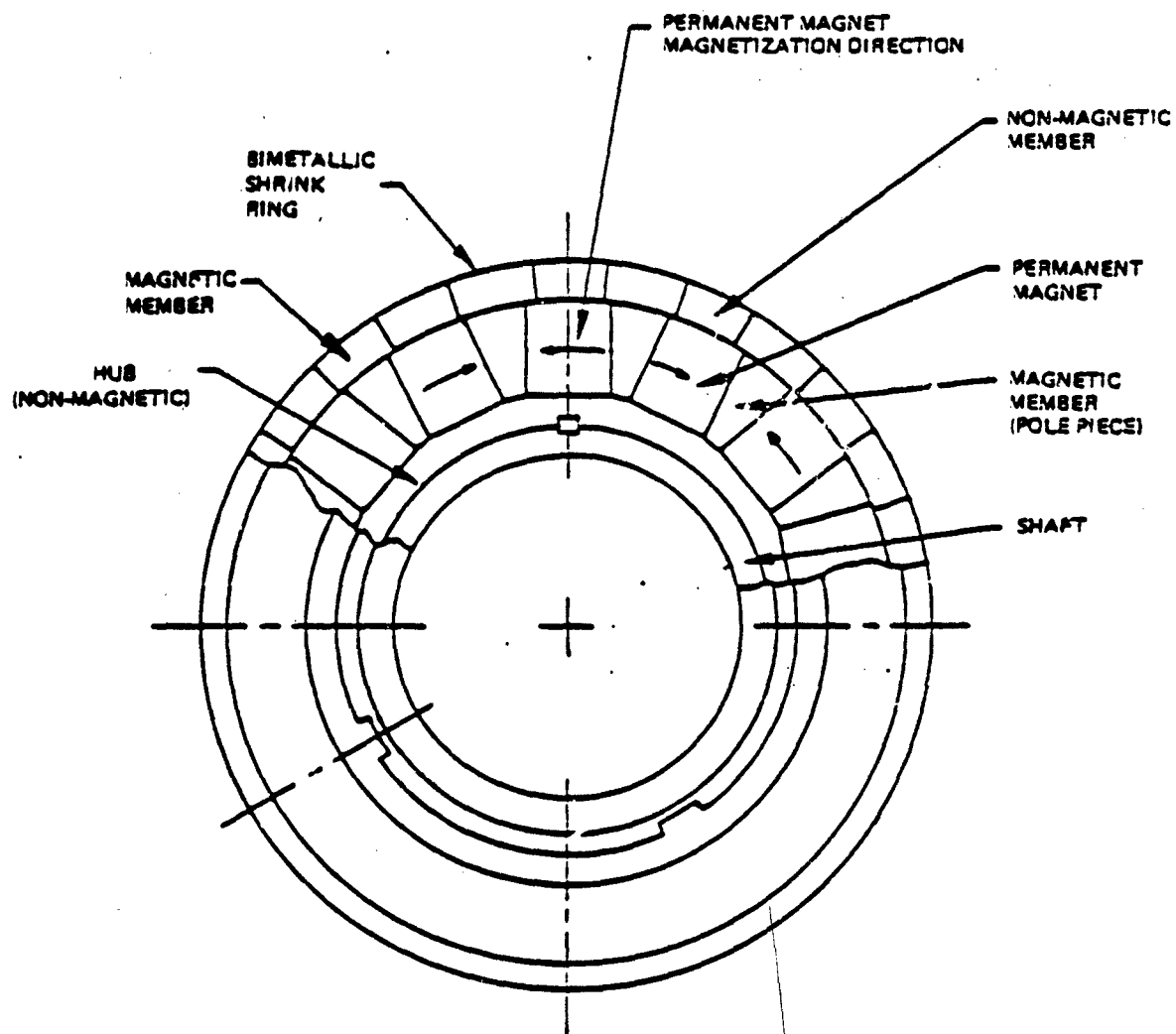MAGNETIC
MEMBER
(POLE PIECE)

SHAFT

Figure 2.2. - Cross-sectional view of a permanent magnet rotor

Since the shrink ring is assembled over the magnets with a predetermined interference, a hoop stress is induced in it. As the rotor speed is increased this interference reduces resulting in a corresponding decrease in the initial stresses. However, the stress level in the ring stays at about the same level as the decrease in stresses due to decrease in interference is compensated by the stresses due to rotation. Thus the stress cycling in the ring is minimized preventing fatigue failures. Moreover, there is little growth of the shrink ring and thus the air gap, which is an important electromagnetic parameter, remains virtually unchanged throughout the entire speed range.

2.2 STATE-OF-THE-ART

Small PMG's used for supplying excitation power in conventional wound rotor generators employ a thin, homogeneous hoop band for retaining magnets. Since these hoop bands are non-magnetic, the electrical air gap is excessive resulting in a lower air gap flux density, and, thus, a lower power to weight ratio. A band of this type used in the PMG for the F-18 electrical system is shown in Figure 2.3.
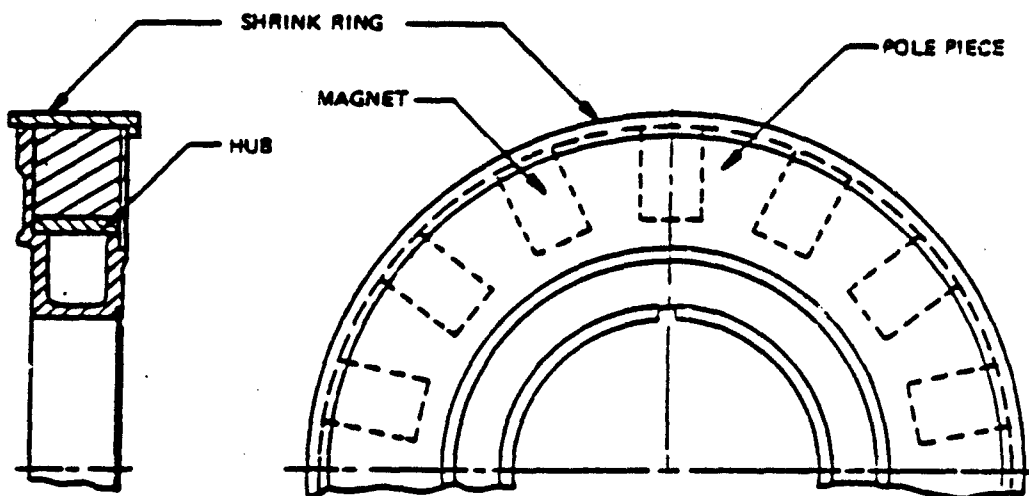

Figure 2.3 - Homogeneous Band used in the F-18 PMG.

This non-magnetic shrink ring is acceptable at lower ratings but imposes an excessive weight penalty as system KVA is increased.

In 1974, General Electric Company, under contract to the US Air Force, embarked on an alternate design for a shrink ring. The objective was to provide an extension of the poles by incorporating a magnetic segment. Thus, the ring was to be bimetallic with alternate magnetic and non-magnetic segments welded together as shown in Figure 2.4. When developing this type of a shrink ring for a 150 KVA VSCF system, a thorough research of the available materials was conducted. It was found taht the combination of Latrobe's MP35N alloy and maraging steel 300 was most suitable. MP35N is non-magnetic with the following nominal composition:

35% Ni
38% Co
20% Cr
10% Mo

Maraging steel 300 is marketed under several trade names and has the following nominal composition

67% Fe
18% Ni   plus fractional percentages of C, Si, Mn, Al and
9% Co   Ti
5% Mo

This combination had the advantage that both alloys responded to a final hardening treatment consisting of aging in the temperature range of 900°F to 1000°F for about four hours. The maraging steel hardens (following solution treatment) by transformation to martensite and aging. The MP35N alloy, however, must be solution treated and cold worked prior to aging. Without cold working, this alloy does not respond to aging. The hardening mechanism is believed to rely upon precipitation of hard intermetallic compound Co_3Mo particles in a hexagonal close packed phase. The hexagonal close packed phase forms only upon cold working the solution treated material.
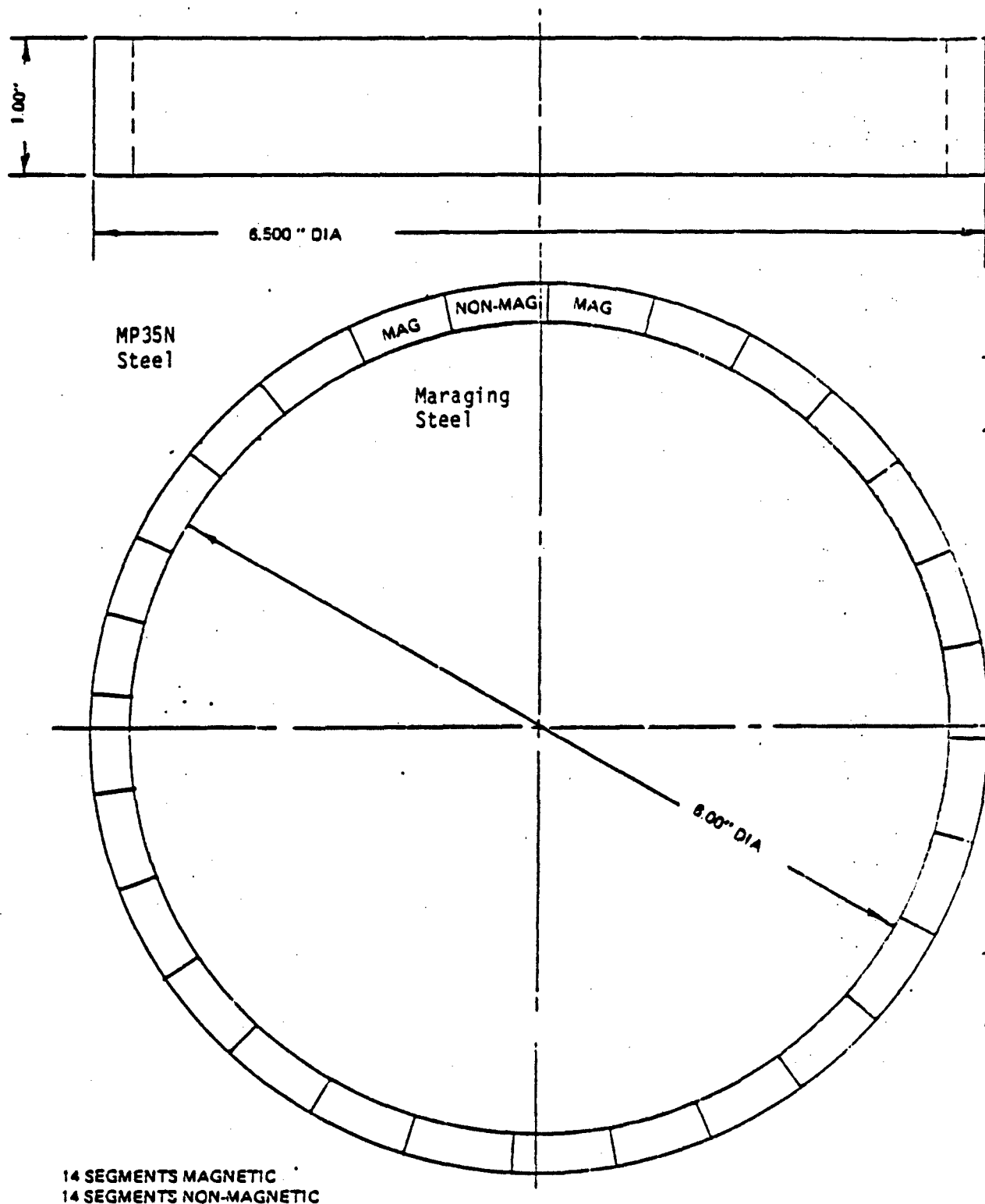
15

1.00"

6.500 " DIA

MP35N
Steel

NON-MAG   MAG

MAG

Maraging
Steel

8.00" DIA

14 SEGMENTS MAGNETIC
14 SEGMENTS NON-MAGNETIC

Figure 2.4 - Composite shrink ring developed for the
150 KVA permanent magnet generator.

16

The necessity for cold working the MP35N meant that the
joining of the magnetic and non-magnetic segments be done by a pro-
cess which would not reheat the MP35N above 1200°F. This, then,
eliminates cold working the MP35N alloy after joining. The cold work-
ing of the joined pieces would, however, not affect the maraging
steel segments since this segment would have aged following the
solution heat treatment.

The need for cold working the MP35N alloy made the process
cumbersome, time consuming and expensive. Thus, for the 60KVA PM
starter/generator, the selected pair of alloys were the nickel chromium
T18 and Carpenter steel CTX-1. These alloys have the following
nominal compositions.

Inconel 718:   52.5% Ni
                18.5% Fe
                19.0% Cr   plus fractional percentages of C,
                5.3% Cb   Mn, Si, B, Ti and Al
                3.0% Mo

CTX-1:   37.7% Ni
                40.0% Fe
                16.0% Co   plus fractional percentages of C,
                3.0% Cb   Mn, Si, Cr, Mo and B
                1.8% Ti
                1.0% Al

This combination of alloys does not require any cold working and can
be solution heat treated at about the same temperature. However,
prior thermo-mechanical history of both alloys has a significant
effect on their strength after aging. The 60 KVA bimetallic shrink
ring is shown in Figure 2.5. This ring was tested for strength using
an expandable arbor and split mandrel, as shown in Figure 2.6, and
found to have a yield strength of over 160,000 psi. Because of the
success of this shrink ring, it was used as a base design in evalua-
ting other design concepts.

17

SHRINK RING

HUB POLE ASSEMBLY

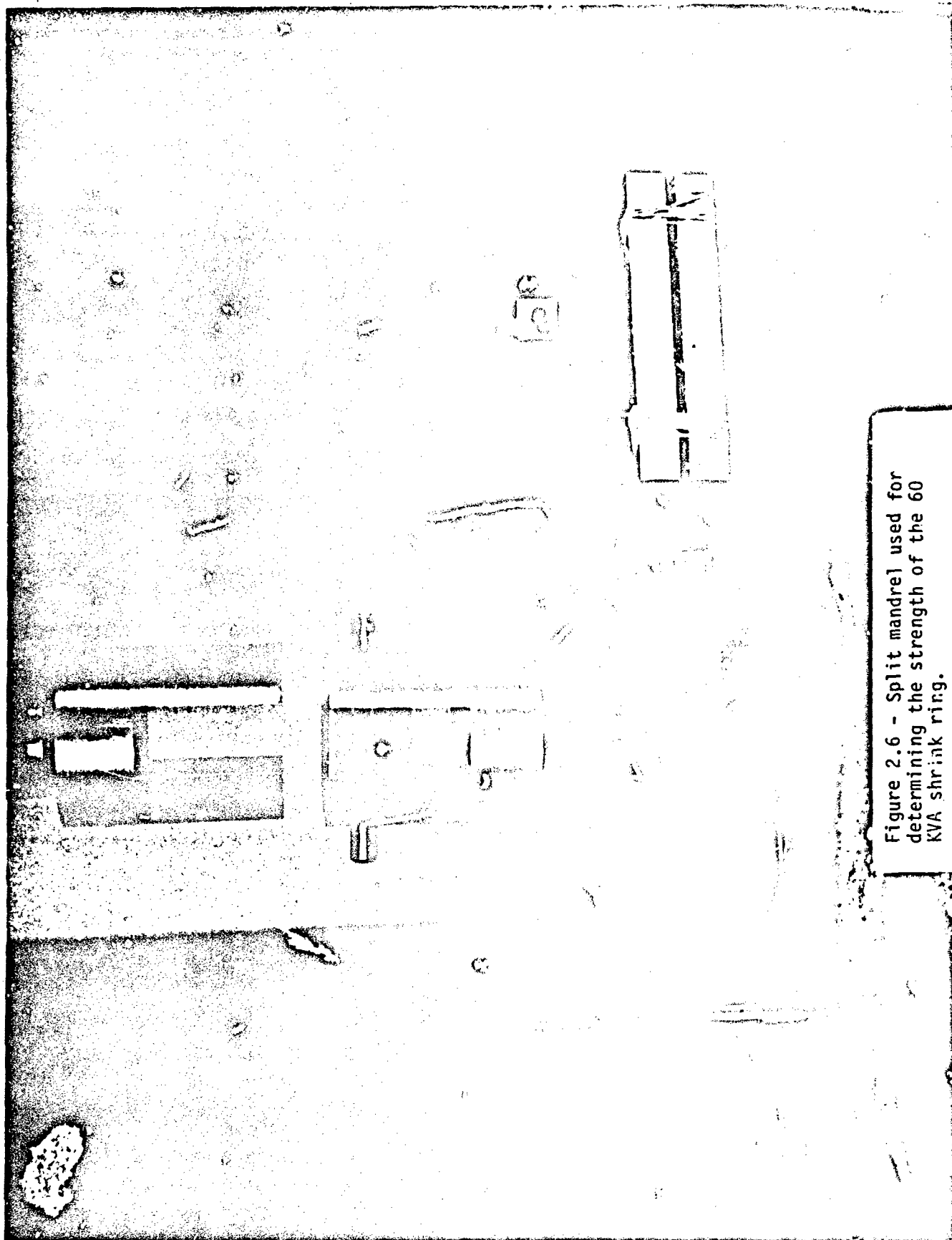Figure 2.5 - 60 KVA shrink ring and hub-pole assembly

Figure 2.6 - Split mandrel used for determining the strength of the 60 KVA shrink ring.

2.3 DESIGN CONCEPTS

Several designs were considered for the purpose of this study and evaluated on the basis of the following factors:

a) **System requirement of commutating inductance**. Designs with per unit commutating inductance greater than 1.0 were not preferred. In general, designs that incorporated a damper winding had lower commutating inductance. The per unit commutating inductance is the ratio of the calculated inductance to the maximum inductance specified for the converter.

b) **System weight**. All designs considered had minor weight differences except for the non-magnetic shrink ring design.

c) **Rotor losses**. Design with laminations in the magnetic segment of the containment ring had the lowest pole face losses.

d) **Rotor dynamics, stresses and critical speed charateristics**.

e) **Containment structure producibility, reliability and cost**.

A general assessment of the five designs is tabulated in Table 2.1. Design 5 which is the selected approach will be described in the next section. The remaining four designs, for a 30/40 KVA system, are discussed here.

2.3.1 Bimetallic Shrink Ring (Design 1, Table 2.1)

The containment method which is identical to that used on the 60 KVA generator served as a base design. The ring consists of 10 magnetic segments of CTX-1 welded to 10 non-magnetic segments made from Inconel 718 as shown in Figure 2.7. The ring designed for a speed

DESIGN	STATOR OD INCH	ROTOR OD INCH	AIR GAP IN.	HT. OF IRON INCH	EM WEIGHT LBS.	TOTAL GEN. WT.LBS.	LOSSES KW				SHRINK RING	GEN. EFF.	COMMUTATING INDUCTANCE PU
							POLE FACE	I²R	CORE	TOTAL			
1. Bimetallic Shrink Ring 60 KVA Design	6.06	5.00	.045	3.0	23	38	1.0	1.86	1.94	6.92	.3	86.1	1.16
2. Non-Magnetic Shrink Ring	5.3	4.16	.1	4.5	27	42	.7	2.77	2.0	7.49	.08	85.2	1.33
3. Pole Retained Magnets with Amortisseur Circuit	5.84	5.0	.03	3.9	24	39	.3	1.96	1.97	6.19	-	87.4	0.96
4. Bimetallic Shrink Ring with Surface Amortisseur	6.06	5.0	.063	3.2	24	39	.9	1.9	1.8	6.52	.27	86.8	0.65
5. Bimetallic Shrink Ring with Laminated Poles and Amortisseur Circuit (Selected Design)	6.05	5.0	.045	2.88	19.9	39	.3	1.9	1.7	5.9	.325	89.4	0.90

NOTES:

1. Losses are based at 40 KVA, 0.95 PF and 26,250 RPM

2. 1 PU commutating inductance is 52.3 uH/Ø

Table 2.1 Comparison of Alternate Designs
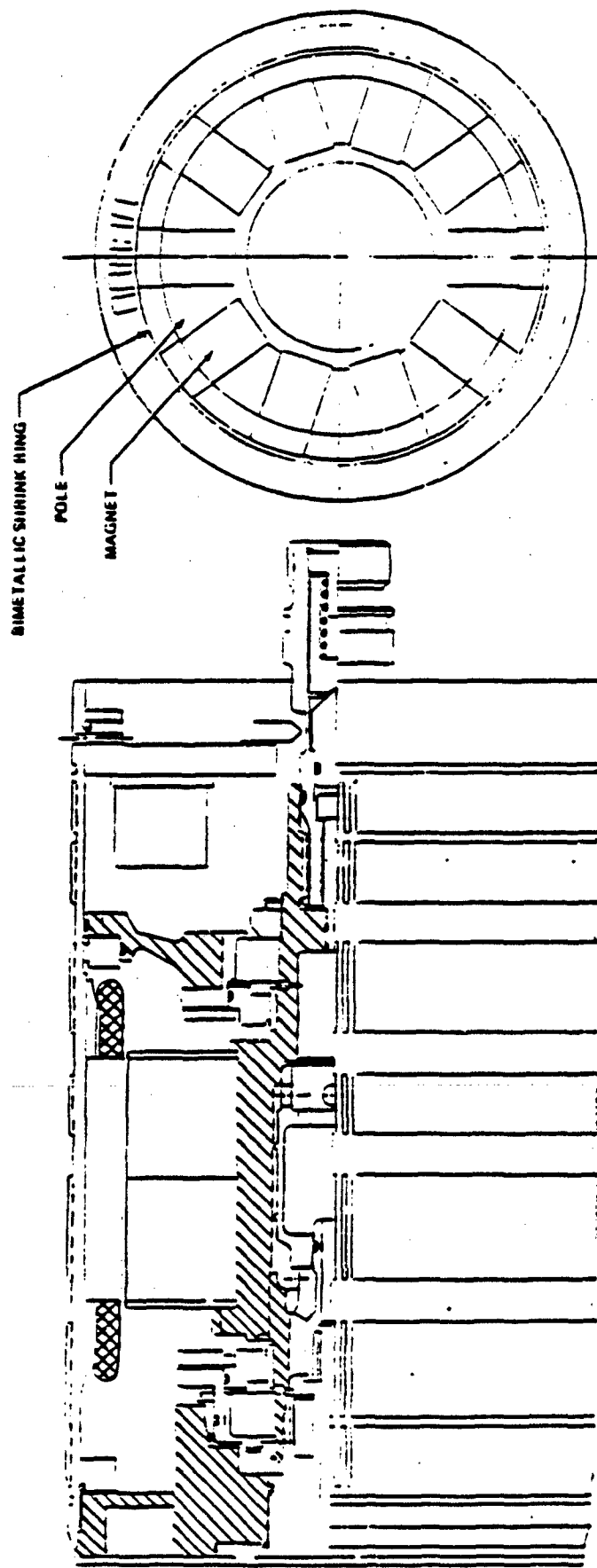
21

BIMETALLIC SHRINK RING

POLE

MAGNET

Figure 2.7 - 30/40 KVA generator with the 60KVA type bimetallic shrink ring

range 15,300-26,250 rpm has a thickness of 0.3 in. For a 30/40 KVA system, the 5" OD rotor is made up of two 1.5" wide discs. The Samarium cobalt magnets have an energy product of 21×10^6 gauss oersted.

The stator made from .006 in. Vanadium Cobalt Iron has an OD of 6.06 in. The losses for this design at rated load and maximum speed (26,250 rpm) were calculated as follows:

Stator copper	1.86 KW
Stator core	1.94 KW
Pole face	1.00 KW
Mechanical	2.12 KW
Total	6.92 KW

The calculated commutating inductance was 61 uH/phase which exceeded the system requirement of 52 uH/phase maximum. Thus, additional optimization would be required to meet this specficiation. The rotor critical speed was much above the overspeed (29000 rpm) due to the stiff shaft.

2.3.2 Non-Magnetic Shrink Ring (Design 2, Table 2.1)

This design uses a non-magnetic hoop band thus obviating the extensive welding required for the bi-metallic type. The material selected was Latrobe MP35N steel due to it's excellent resistivity properties combined with a yield strength in excess of 200,000 psi. The layout of a generator using this type of containment is shown in Figue 2.8.

The radial thickness of .08 in. for the ring combined with the .02 in. air gap resulted in a significantly lower air gap flux densciy in comparison with the other designs. Consequently , a 4.5 in. height of iron was required for a 30/40 KVA rating. Total generator losses were estimated as 7.49 KW at rated load and maximum speed. The commutating inductance far exceeded the maximum value of 52 uH/phase specified for the converter.
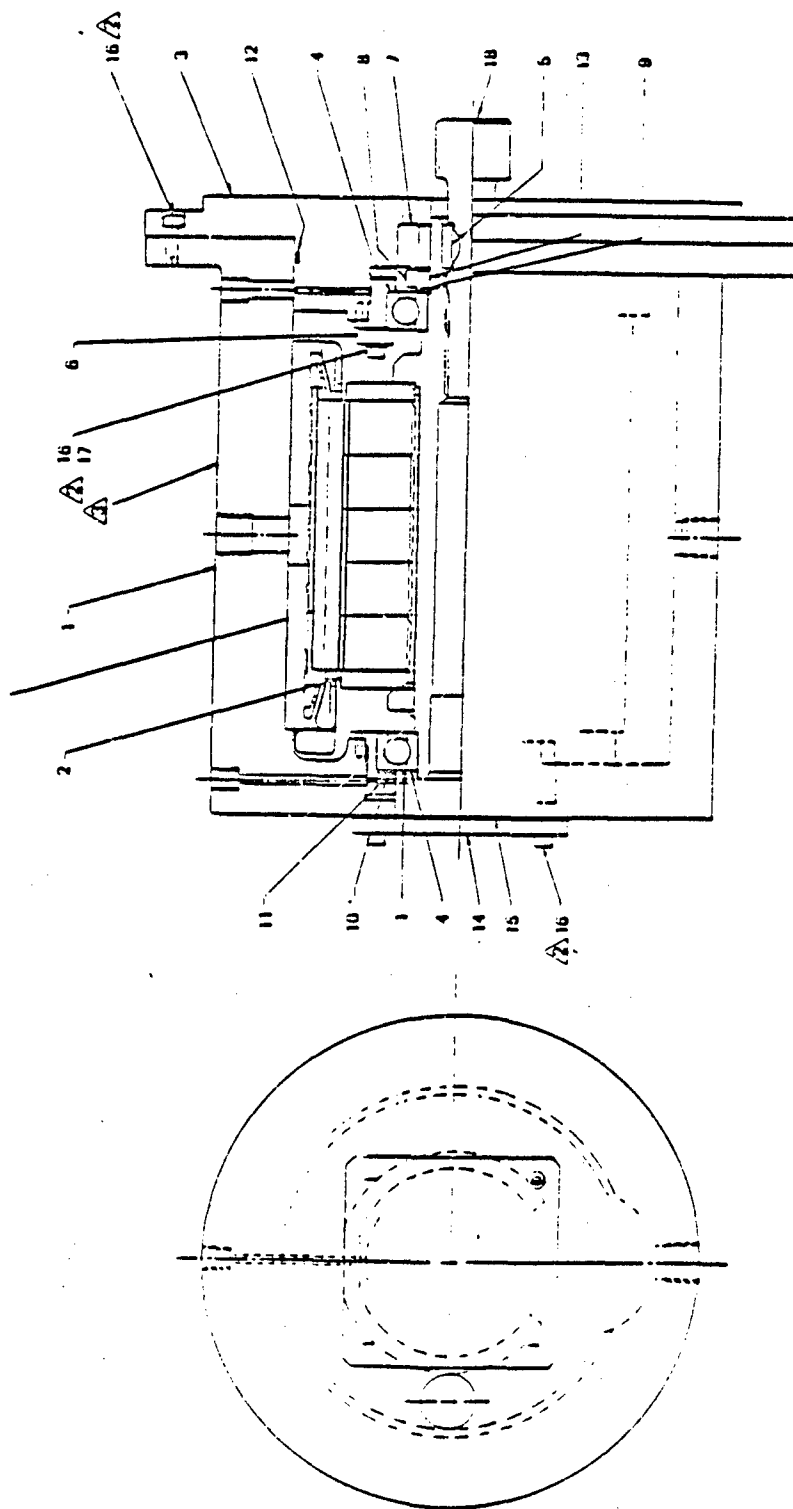
Figure 2.8 – 30/40 KVA generator with a non-magnetic shrink ring

Although, this approach is feasible, it is not competitive with the other designs for higher system ratings. The inherently low flux density achievable with this design imposes a severe weight and volume penalty. Moreover, the longer stack length required significantly lowers the generator critical speed.

2.3.3 Pole Retained Magnets (Design 3, Table 2.1)

The arrangements studied for this design are shown in Figure 2.9. The poles, which are welded to the non-magnetic hub, are shaped such that they provide support to the magnets. In one configuration, the magnet has straight sides and the load is transfered to the pole by the top sticks. In the other approach shown, the magnet is tapered and the load is transfered because of the wedge effect.

Since the entire centrifugal force of the magnets and poles are to be supported by the weld at the hub, it is imperative that a high yield strength is attained at that junction. Also, due consideration must be given to the stress concentration effect resulting from the radius at the base of the pole. Consequently, the strength of the weld determines the size and weight of the generator.

Although the top stick retained magnet approach is favored from a producibility standpoint, it produces a higher stress at the pole tips. The tapered magnet design reduces the pole tip stresses but introduces several manufacturing problems. Since the outer edge of the magnet needs to be contained, a non-magnetic clip needs to be bonded on prior to the grinding of the magnetic taper. Also, very close tolerances need to be held to insure the proper positioning of the magnets for electro-magnetic and mechanical balance.

At maximum speed, the stresses in the hub were in the neighborhood of 145,000 psi. While this stress appears excessive, the design is feasible if materials like Inconel-718 are used for the hub. A corresponding material for the pole could be CTX-1. The generator
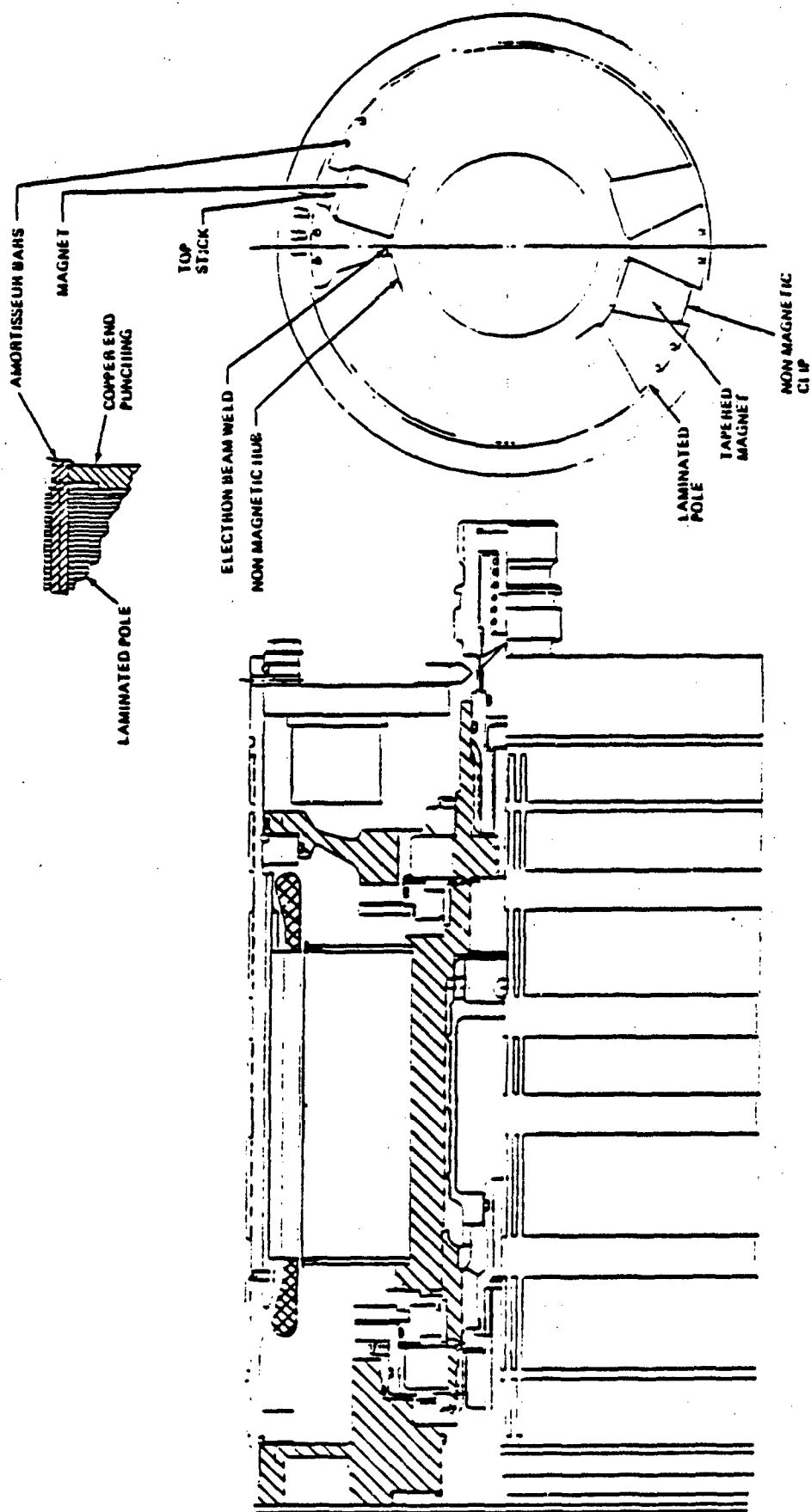
25

Figure 2.9 - 30/40KVA generator with pole retained magnets.

AMORTISSEUR BARS

MAGNET

COPPER END PUNCHING

TOP STICK

LAMINATED POLE

ELECTRON BEAM WELD

NON MAGNETIC HUB

NON MAGNETIC CLIP

TAPERED MAGNET

LAMINATED POLE

26

layout is shown in Figure 2.9 for a 30/40 KVA system rating. The commutating inductance is low because of the presence of amortisseur bars in the poles.

Although this design is feasible, it lacks the precise control required for high speed rotors. The preloading, which is essential to minimize stress cycling, is difficult to achieve with this configuration. Tapered shims may be used for preloading but the preload level cannot be precisely controlled.

2.3.4 Bimetalic Shrink Ring with Surface Amortisseur Circuit (Design 4, Table 2.1)

The use of an effective amortisseur circuit considerably reduces the commutating inductance. This design, shown in Figure 2.10, uses a "wrap around" amortisseur cage on the outside of the rotor shrink ring. Three .02" x .1" copper bars are placed on each of the pole faces and brazed to the copper end plate. This case is then wrapped with high strength non-magnetic binding wire supported at each end with Inconel 718 rings. The case and the rings are designed to be self supporting and do not affect the rotor mechanics. The rotor, as shown in Figure 2.10 has the following dimensions:

Rotor diameter over shrink ring	5.0"
Amortissuer cage thickness	0.02"
Binding wire diameter	0.02"
Rotor diameter over binding wire	5.08"
Mechanical gap	0.023"
Electromagnetic air gap	0.063"

This design is similar to the simple bimetallic ring approach discussed earlier except that the presence of the amortisseur circuit leads to an increase in air gap. This results in an increase in the size and weight of the generator. This design is feasible but not very favorable from a producibility standpoint. One of the risks associated with this approach is the unwrapping of the steel wires at high speeds and loading conditions.
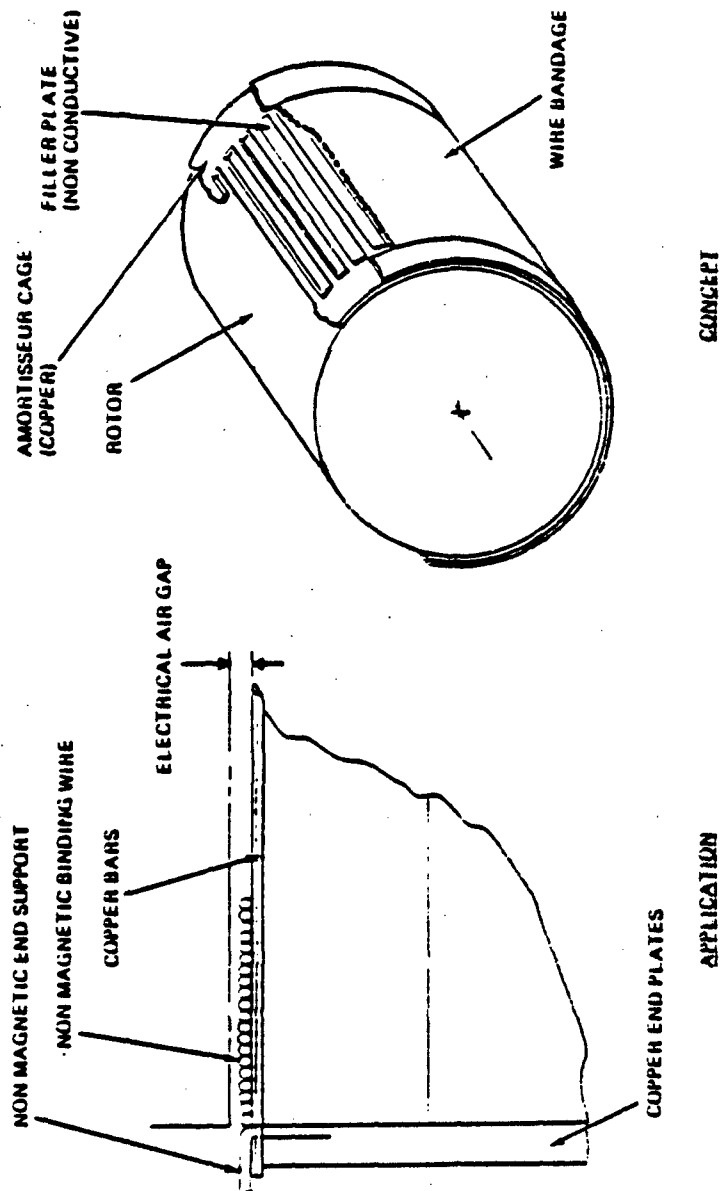
27

CONCEPT

APPLICATION

Figure 2.10 - 30/40 KVA generator with surface amortisseur cage retained with binding wire.

28

2.4 SELECTED DESIGN

The selected approach, shown in Figure 2.11, consists of a bimetallic shrink ring with laminated magnetic segments and an amortisseur circuit. This design offers the best balance between the several factors considered in evaluating alternate designs as assessed in Table 2.1. The rotor containment is based on a well developed shrink ring design and uses the CTX-1/Inconel 718 combination for the magnetic and non-magnetic segments. This results in a ductile weld with a yield strength approaching that of the base materials.

The use of .02" CTX-1 laminations to form the magnetic segments reduces the rotor pole face losses by approximately 40% compared to the solid design. During the aging of the shrink ring to develop the mechanical properties, an oxide coating is formed on the laminations thus providing interlaminar insulation and reducing the eddy currents. Thus, the magnets operate at a cooler temperature because of the lower pole face losses. This minimizes the derating of the magnets and leads to an increase in the generator output.

The amortisseur circuit comprised of three .057" diameter copper bars per pole brazed at each end to a thin copper ring. The incorporation of these amortisseur bars results in a significant reduction in the commutating inductance of the generator, and, consequently, the converter losses.

The development work conducted to insure the producibility of the design is discussed in the next section.
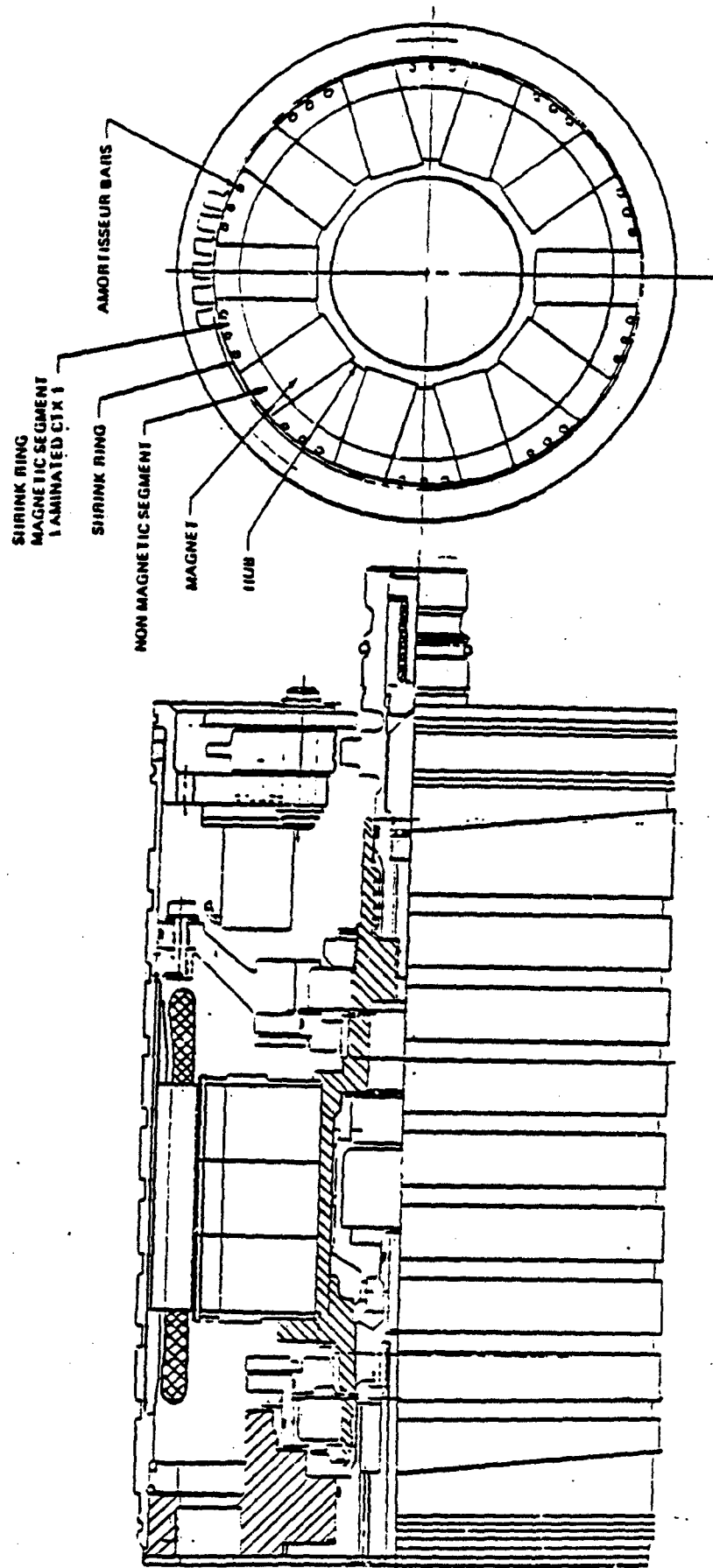
29

Figure 2.11 - 30/40 KVA generator with the selected containment structure.

AMORTISSEUR BARS

SHRINK RING

MAGNETIC SEGMENT LAMINATED (1 X 1)

SHRINK RING

NON MAGNETIC SEGMENT

MAGNET

OIL/80

SECTION III
COMPONENT DEVELOPMENT

3.1   METALLURGICAL EVALUATION

The component development task was performed during the first phase of the program to determine the producibility of the containment structure and to insure that the mechanical requirements would be met. The design called for a strong yet ductile weld between the CTX laminations and the solid Inconel segments. Moreover, the amortisseur holes needed to be bored in the laminations and precisely positioned to allow insertion of the amortisseur bars. These all appeared to be manufacturing challenges and needed to be resolved in order to reduce the risk of the program.

General Electric's Corporate Research and Development Center was contracted to roll CTX-1 plates down to .02" strips. The strips were then stamped using an existing die to produce the laminations shown in Figure 3.1. The shoulders were undesirable and were machined off after the laminations were stacked up and held in place by TIG welding.

The Inconel 718 pieces were machined to form the segments as shown in Figure 3.2. The laminated pole was placed in between the Inconel segments and electron beam welded on both sides. The equipment used for electron beam welding permitted very precise tracking of the beam resulting in a 100% joint. The fusion and refreezing of the weld was rapid and, thus, an extremely fine metallographic structure was formed. Electron beam welding offered versatility in joint configuration and a quick turn around time in component processing.

After welding, the samples were milled to 0.31 in. thickness with a circular cutter to remove the rivet hole in the laminated pole and the lip of the Inconel pieces. During machining, the laminations

31

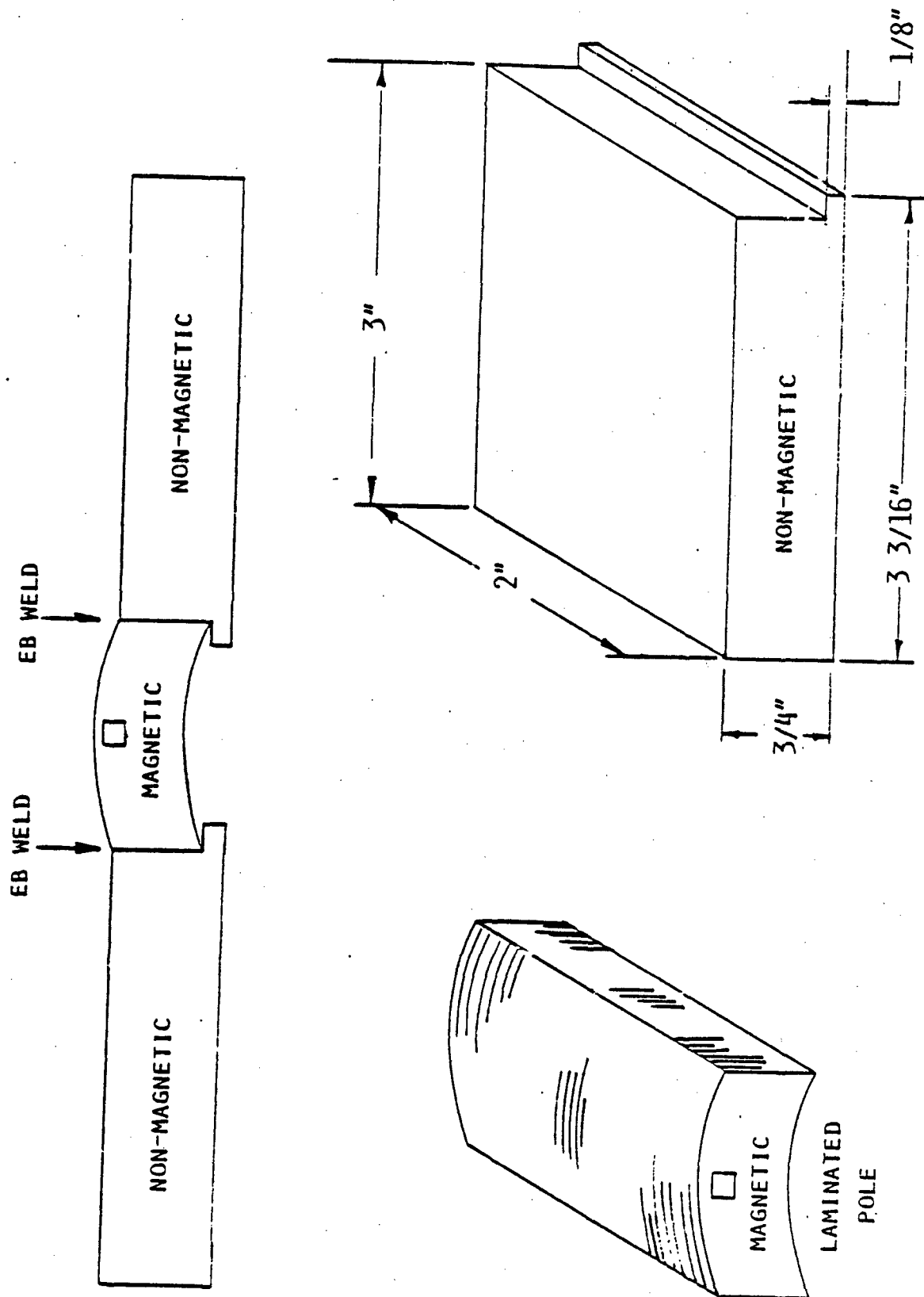Figure 3.1 - Laminations of CTX-1
from .02" thick strips

Figure 3.2 - Tensile test samples

33

were securely clamped to control distortion. Figure 3.3 shows a
sample prior to and after machining. Finally, the samples were
ground to 0.272 in. thickness removing equal amounts of material
from both sides.

At this stage of machining, a dye penetrant check was made
which revealed a lack of fusion at one side of one of the samples
evident in Figure 3.4. Another .022" of material was ground which
eliminated this lack of fusion indication. The two samples were then
sectioned to provide four tensile test bars and two metallographic
sections from each sample. Table 3.1 gives the dimensions of each
of the test bars. Precise sectioning of the samples was possible by
using a travelling wire electrical discharge machine. About 15 to
16 laminations were included in each test bar which were 0.25 in. by
0.325 in. in cross-section. Some of the laminations were partly cut
by the EDM wire and these are indicated in the table as "fractional
laminations".

The metallographic samples were mounted polished and etched
to show the weld and microstructure on planes parallel and perpendicu-
lar to the lamination plane. The microstructure is shown in Figures
3.5 through 3.12. Some small porosities were observed in the fusion
zone which had not been detected on the radiographs. The CTX-1 was
recrystallized about .015 in. back from the fusion zone and many of
the tensile failures occurred in this recrystallized zone. No change
was observed in the Inconel 718 microstructure immediately adjacent
to the fusion zone.

During tensile testing, the plastic deformation before frac-
ture was confined entirely to the relatively soft fusion zone and
the heat affected zone of the weld. The load extension curves showed
a total plastic extension of only .003 in. for most samples.

34

1A	.250	X	15-1/2 Laminations
	.3224		.0806 Sq.in. (A)
1B	.250	X	15-1/2
	.3215		.080375 (C)
1C	.250	X	16 Laminations
	.3207		.080175 (E)
1D	.250	X	15 Laminations
	.3265		.08163 (G)
2A	.2497	X	15 Laminations
	.3278		.08185 (B)
2B	.2497	X	15 Laminations
	.3255		.08128 (D)
2C	.2499	X	15-1/3 Laminations
	.3257		.08139 (F)
2D	.2498	X	15-1/2 Laminations
	.3262		.08148 (H)

Table 3.1

Dimensions of Test Bars
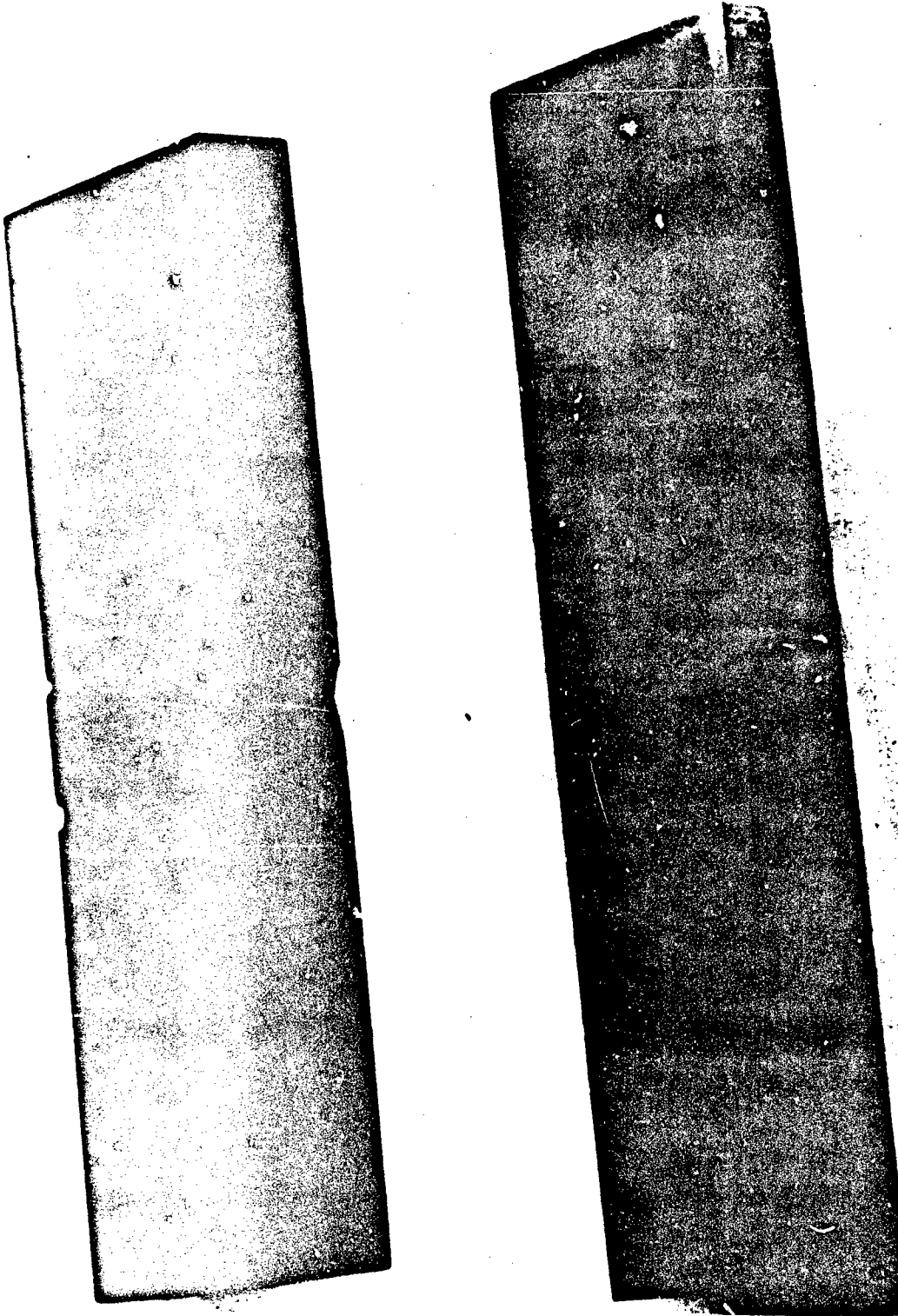
Figure 3.3

As received sample #1 at top.
Rough milled sample #2 at bottom.

36
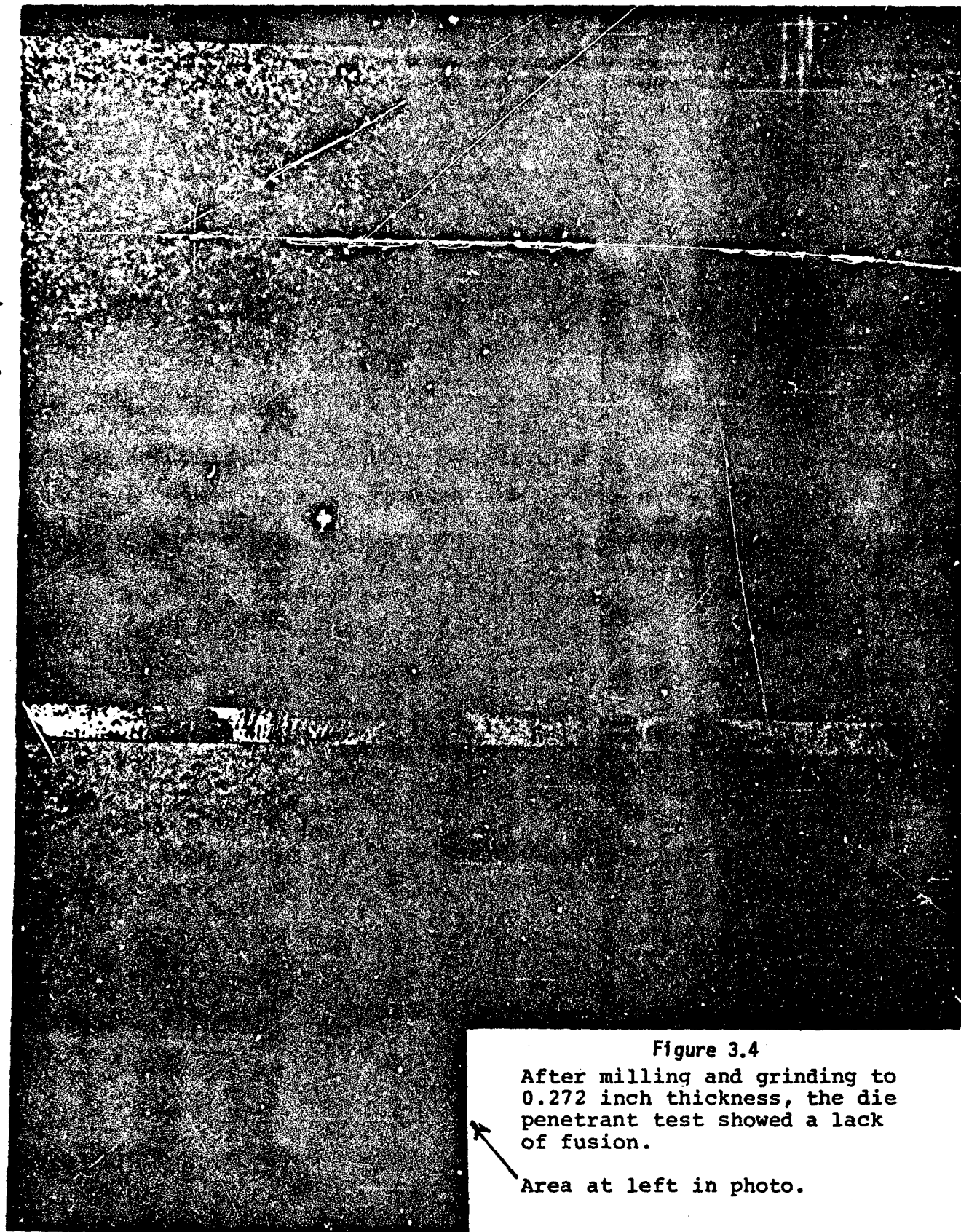
Figure 3.4
After milling and grinding to
0.272 inch thickness, the die
penetrant test showed a lack
of fusion.

Area at left in photo.
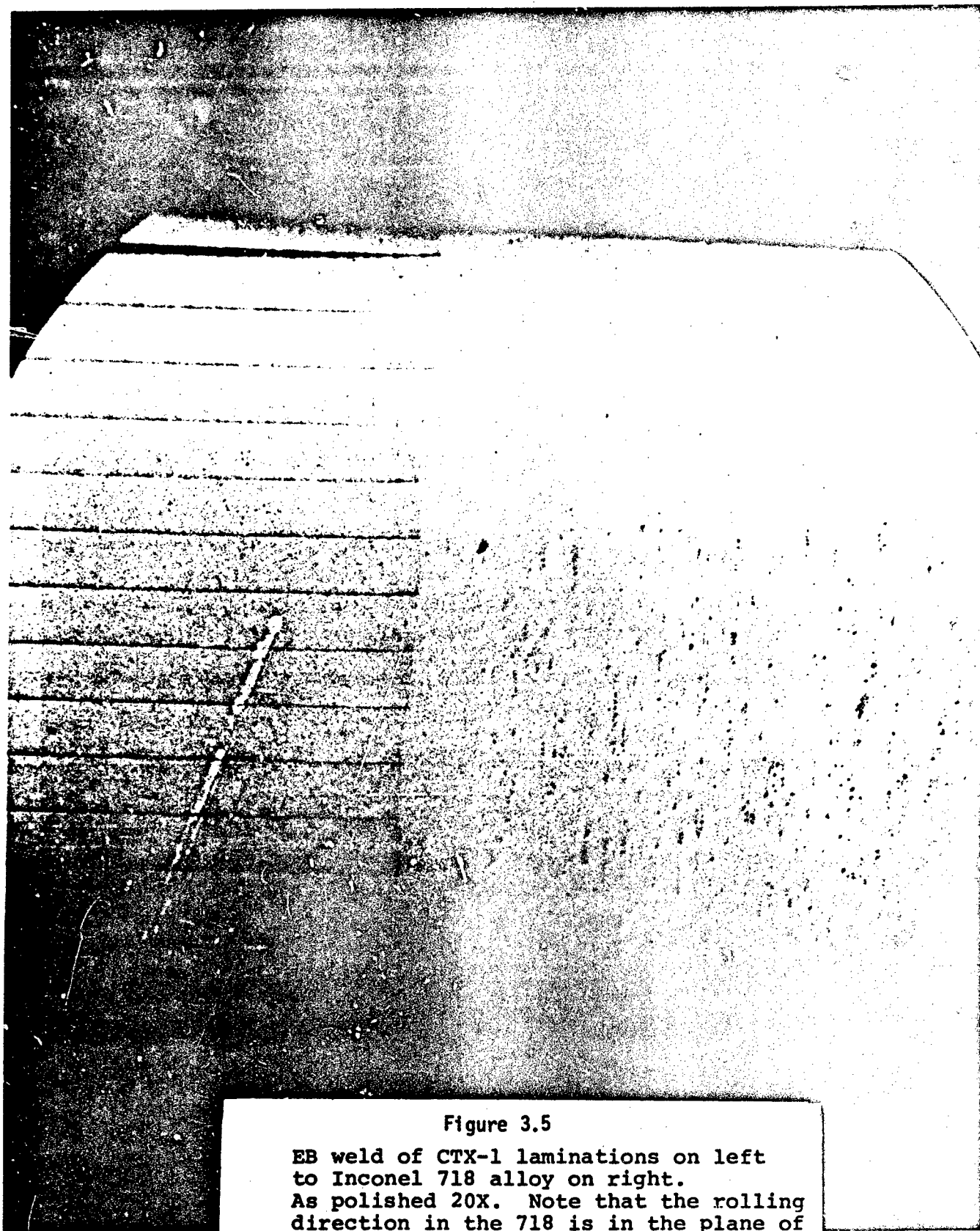
Figure 3.5

EB weld of CTX-1 laminations on left
to Inconel 718 alloy on right.
As polished 20X. Note that the rolling
direction in the 718 is in the plane of
the picture. Welds showed generally
good quality with very little porosity.
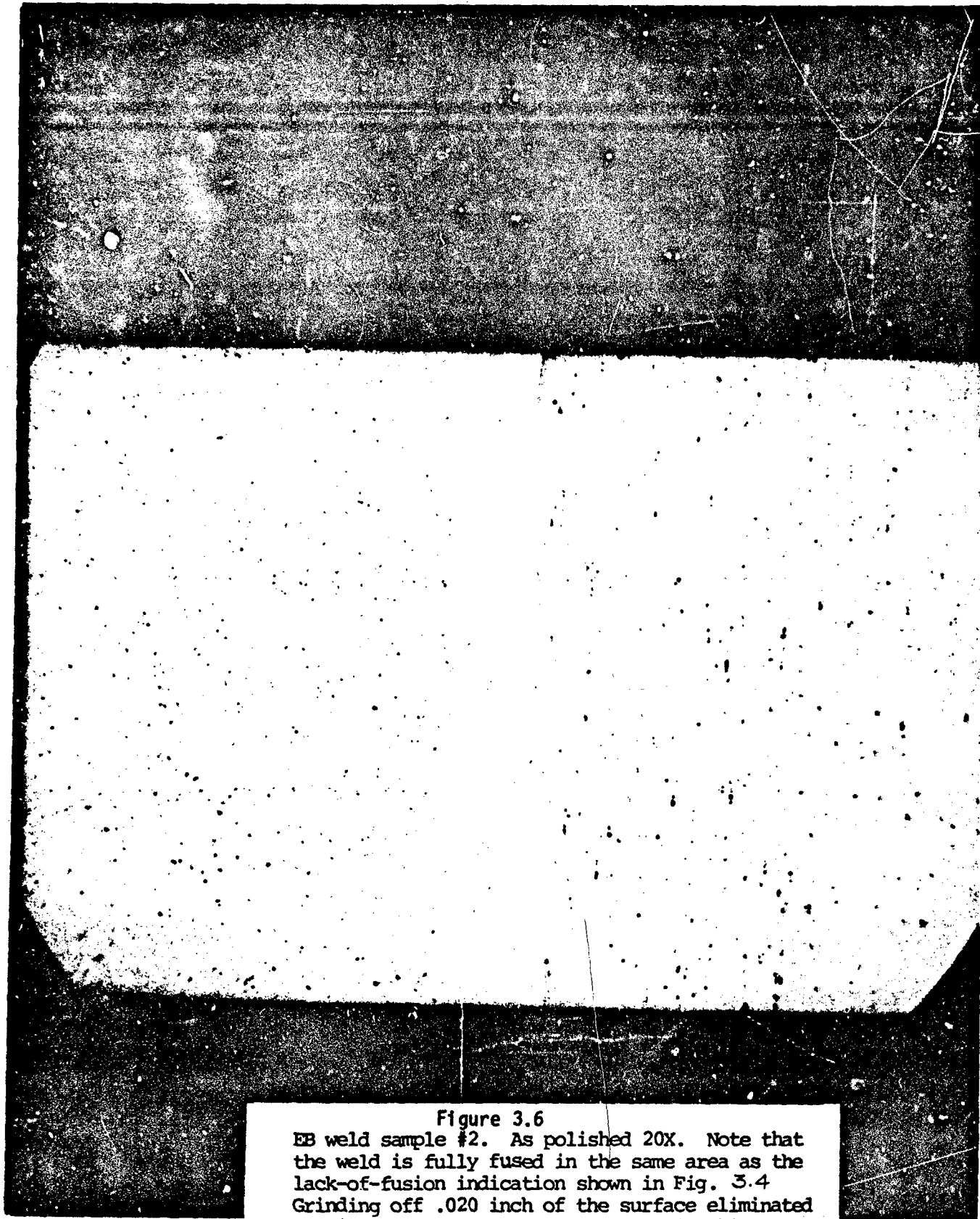
Figure 3.6
EB weld sample #2. As polished 20X. Note that
the weld is fully fused in the same area as the
lack-of-fusion indication shown in Fig. 3.4
Grinding off .020 inch of the surface eliminated
the indication completely as shown in this
photo. This section does not reveal the CTX-1
laminations at left because it was taken at
90° to the section shown in Fig. 3.5
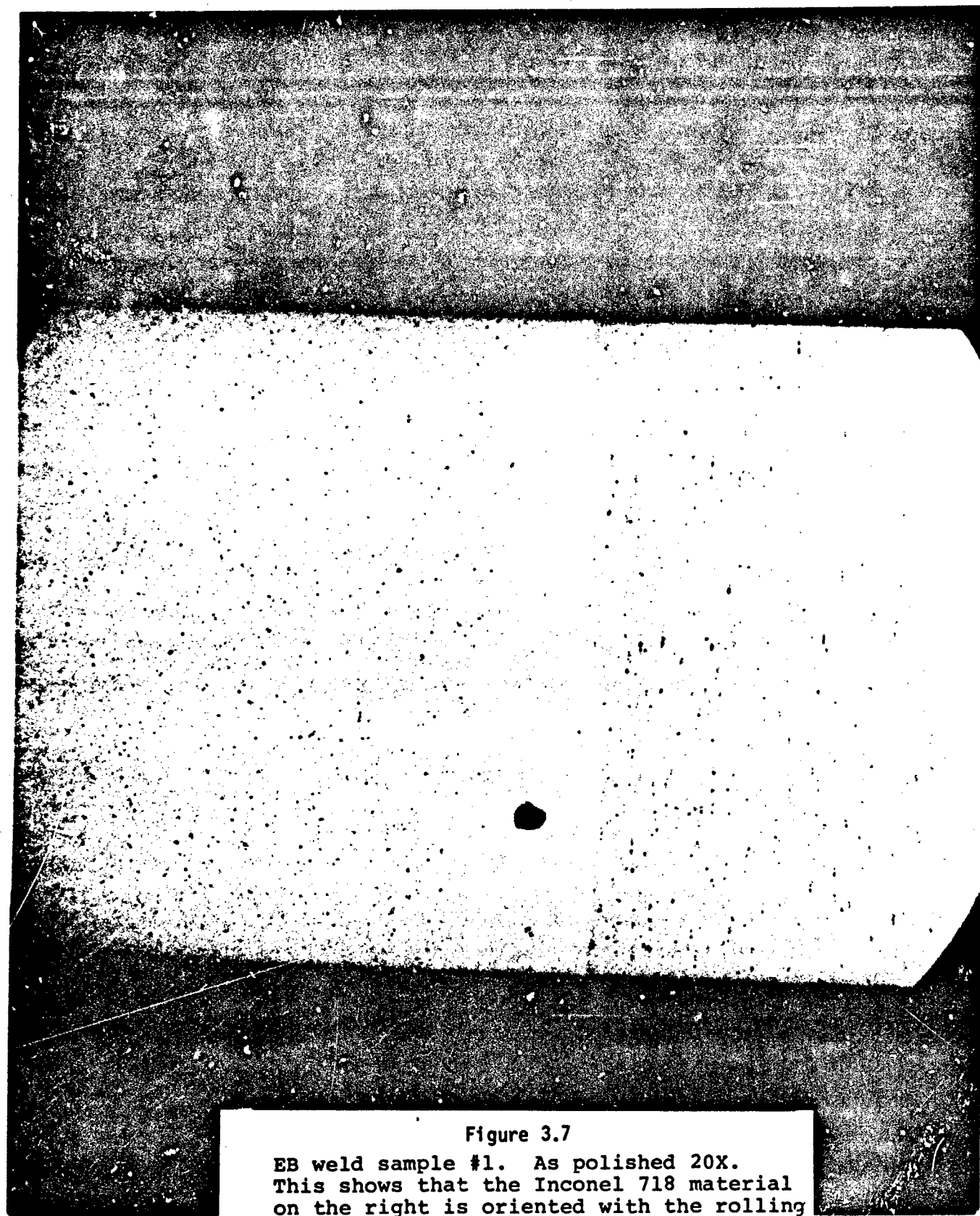
Figure 3.7

EB weld sample #1. As polished 20X.
This shows that the Inconel 718 material
on the right is oriented with the rolling
direction perpendicular to the lamination
plane. The rolling plane is parallel to
the plane of the weld.

40
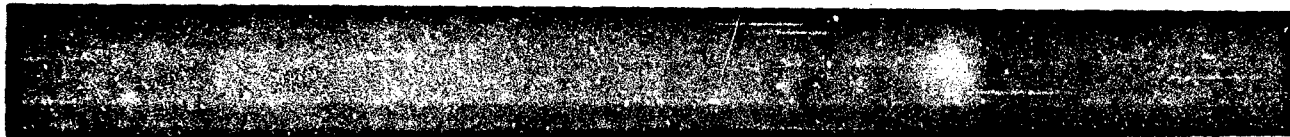
Figure 3.8
EB weld sample #1. As polished 200X.
Some diffusion welding occurred between
the laminations as shown in the center
of the photo. This short-circuiting
extends back about .02 to .03 inches
into the lamination stock.   41
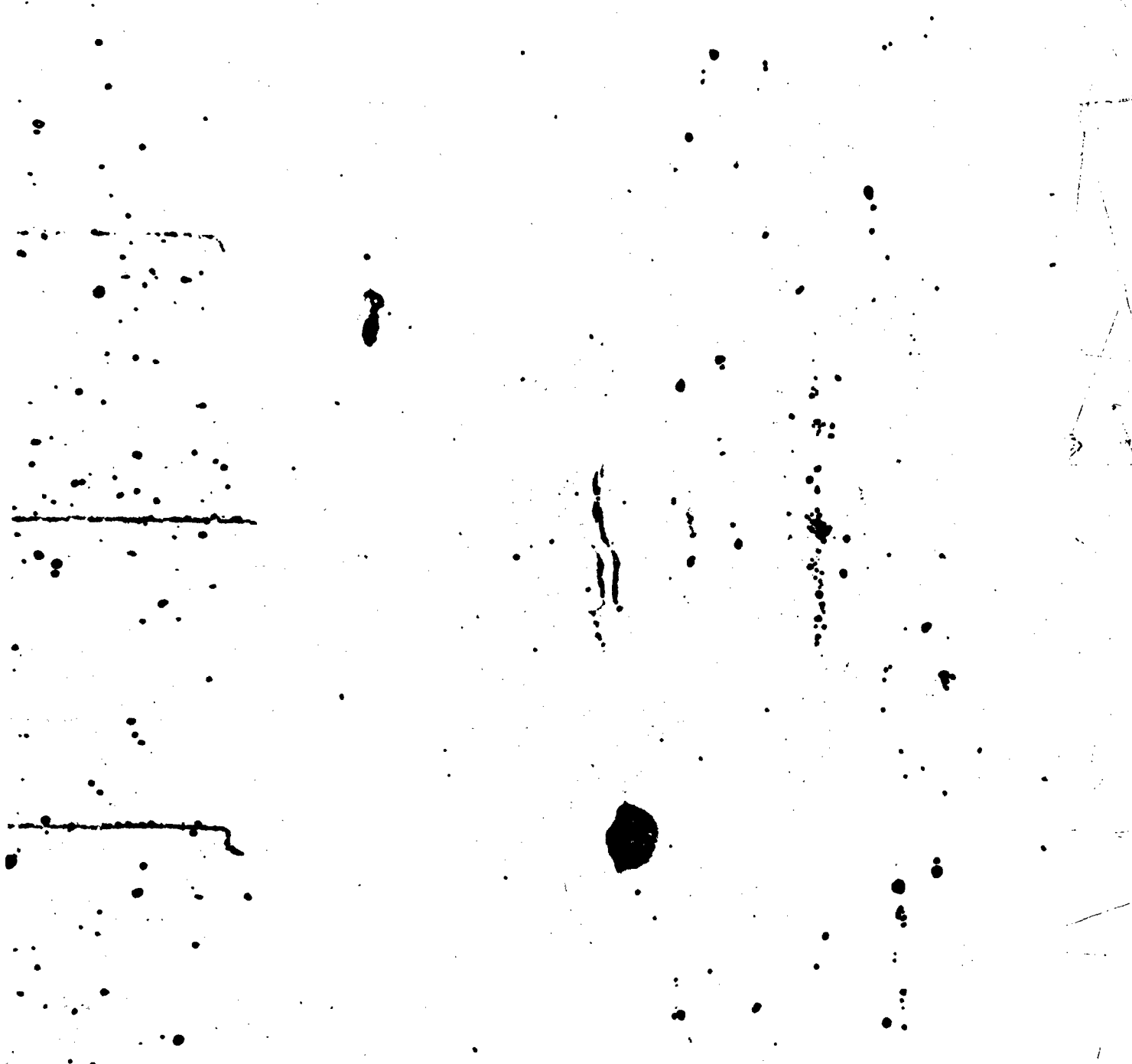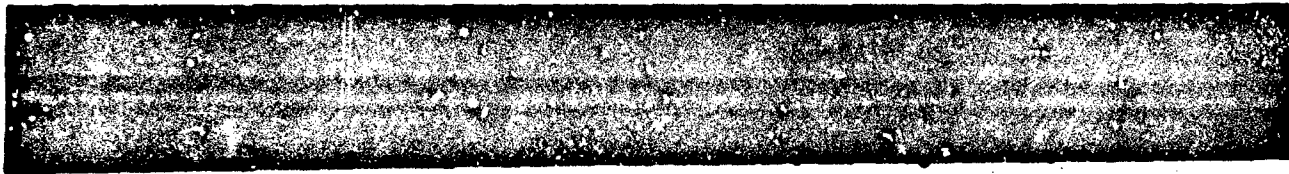
Figure 3.9

EB weld sample #2. As polished 100X.
The stringer inclusions in the 718 alloy
appear to cause weld defects in the
fusion zone.   42
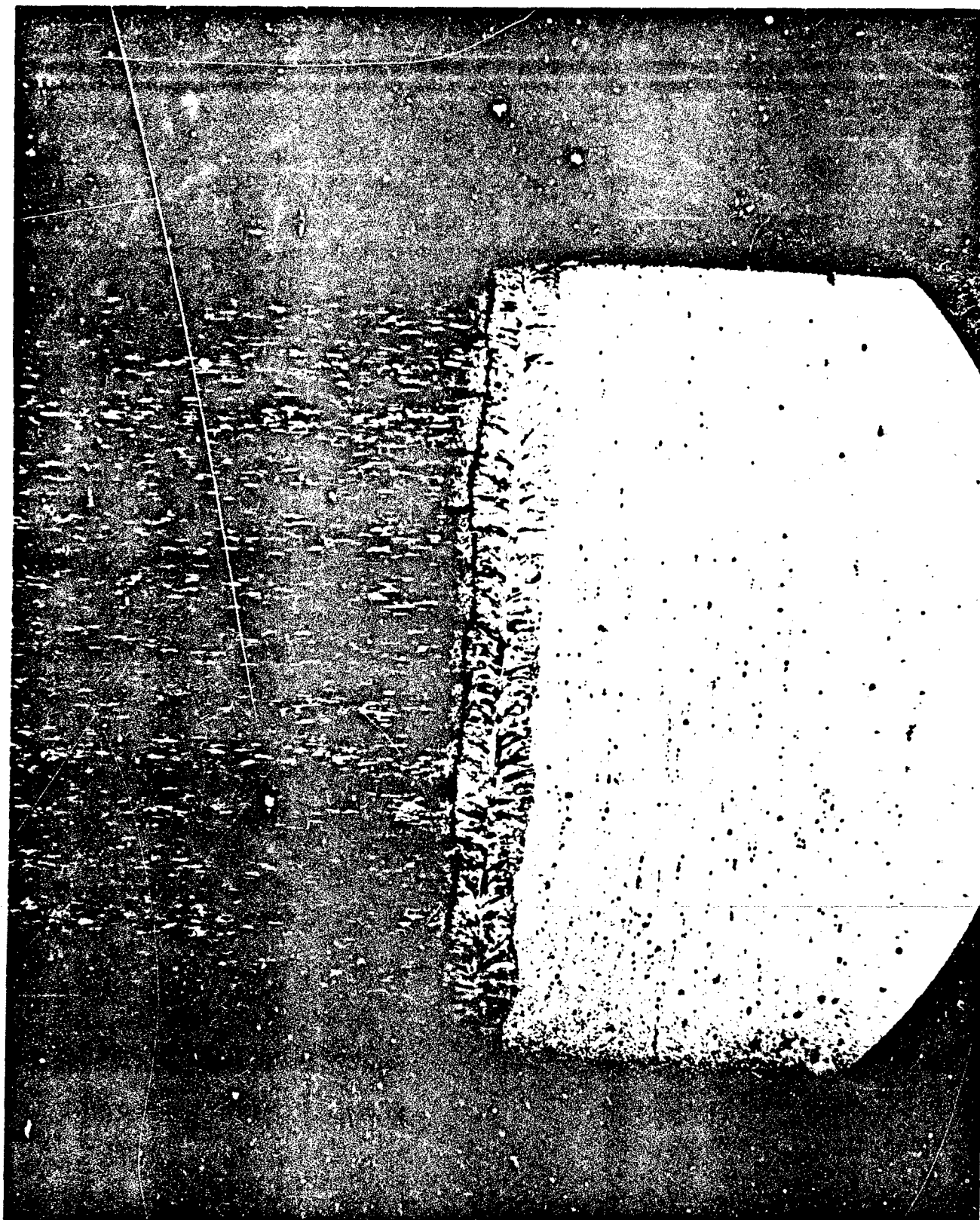
Figure 3.10
Weld sample #1. Mixed acids etch 20X.
Recrystallized zone in CTX-1 alloy
shows plainly next to the fusion zone.

43

Figure 3.11

Weld sample #1. Mixed acids etch, 20X.
CTX-1 on left has a typical cold worked
structure except for the recrystallized
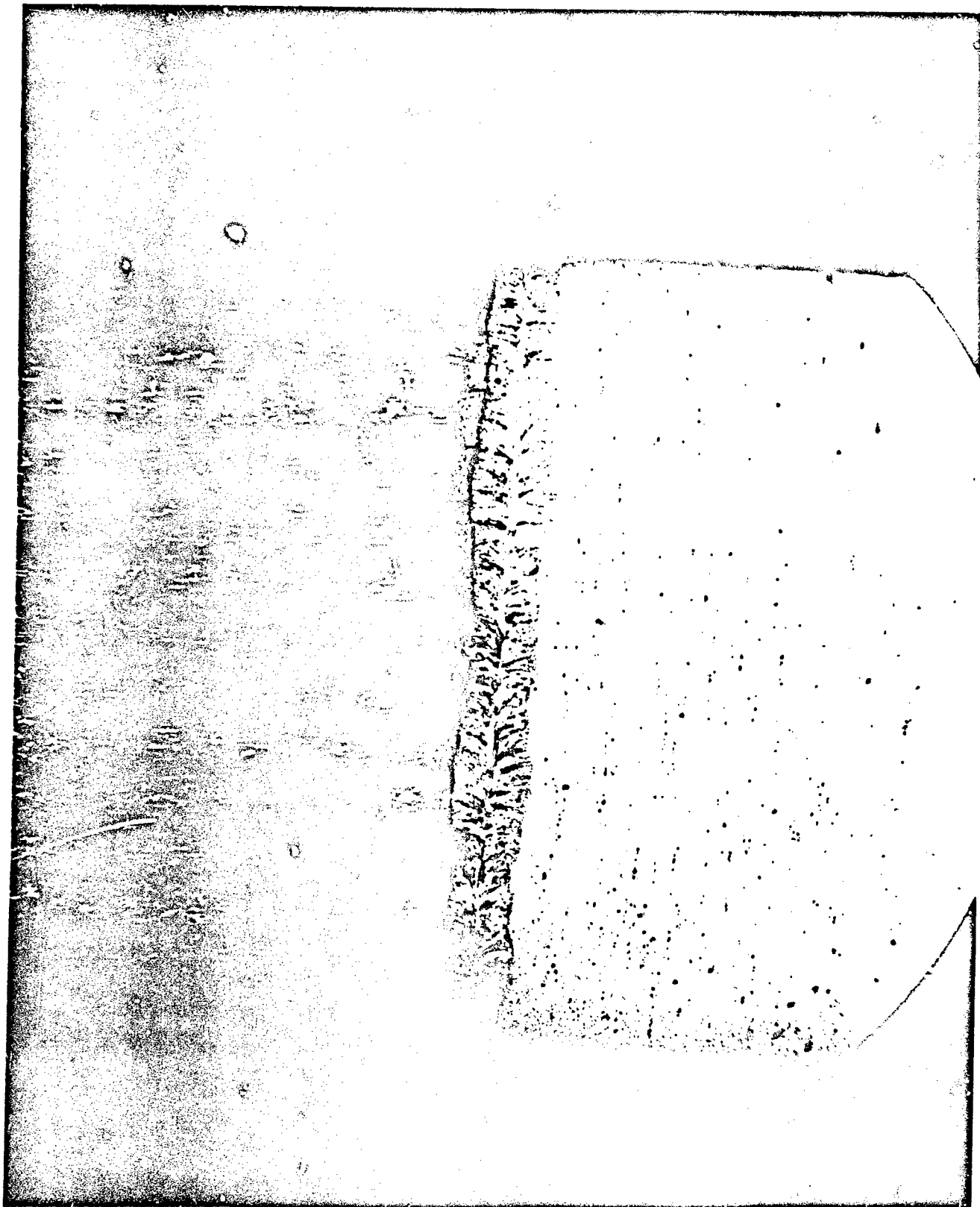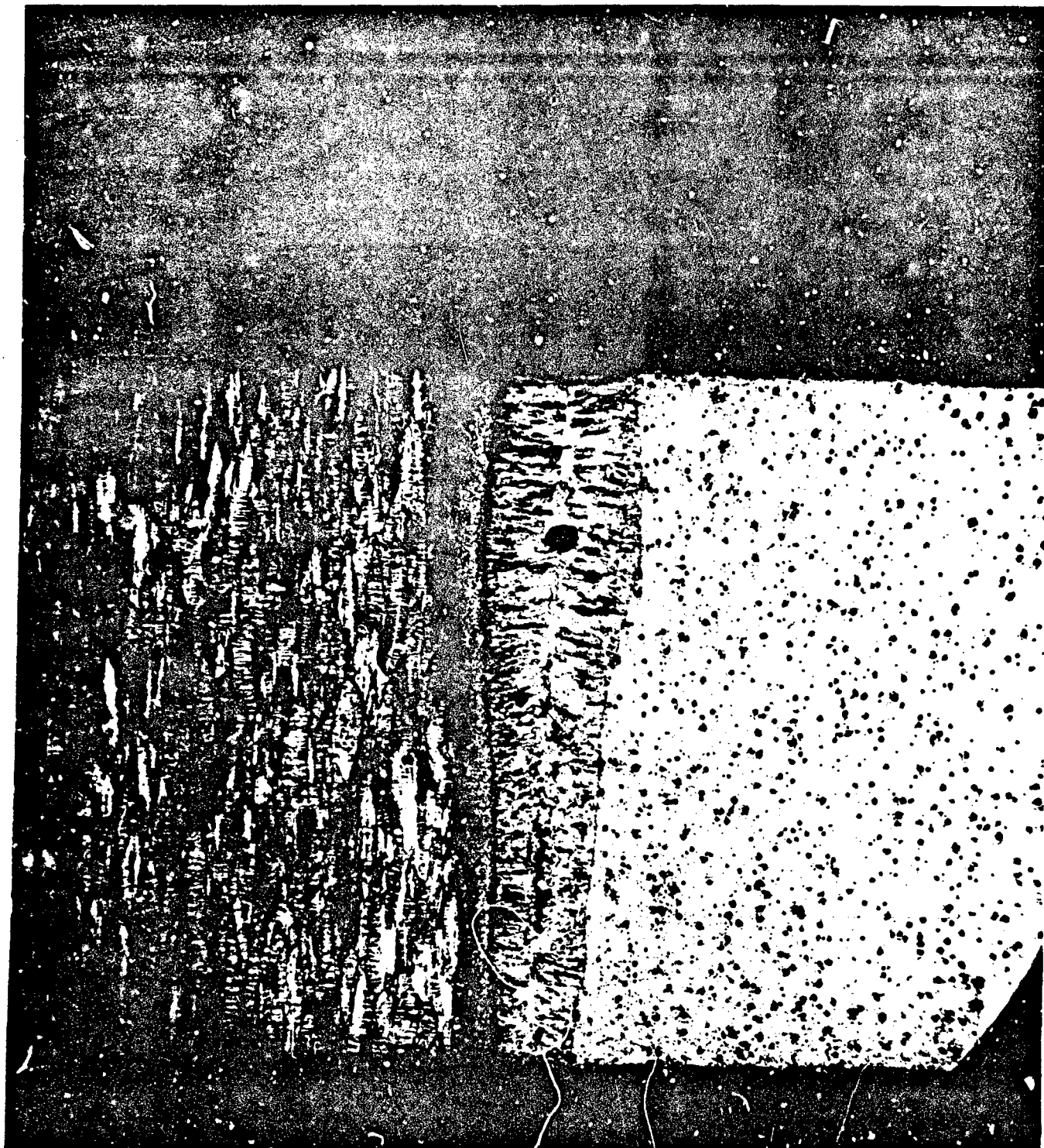zone in the center adjacent to the
fusion zone.

44

Figure 3.10

Weld sample #1. Mixed acids etch 20X.
Recrystallized zone in CTX-1 alloy
shows plainly next to the fusion zone.

43

Figure 3.11

Weld sample #1. Mixed acids etch, 20X.
CTX-1 on left has a typical cold worked
structure except for the recrystallized
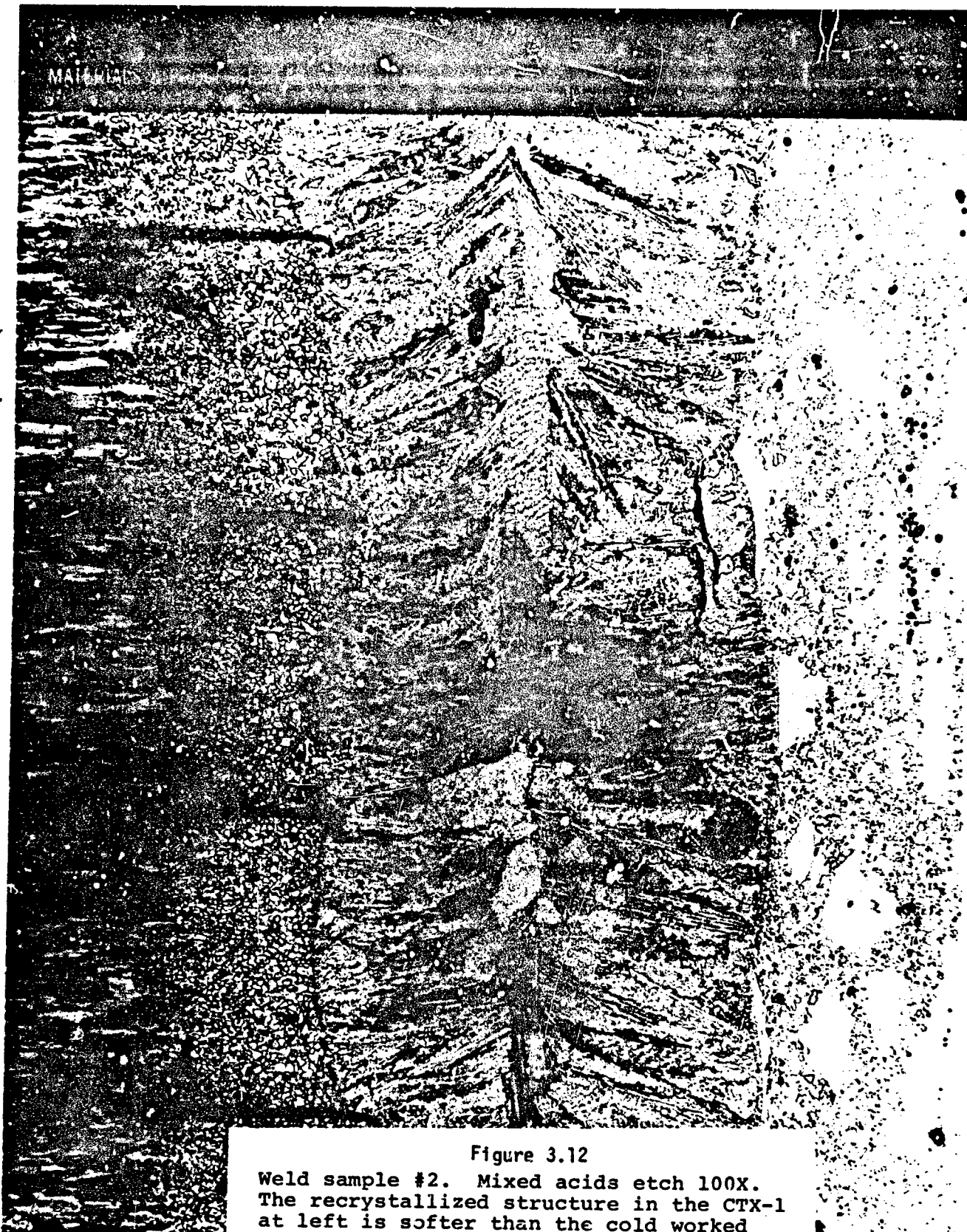zone in the center adjacent to the
fusion zone.

44

Figure 3.12
Weld sample #2. Mixed acids etch 100X.
The recrystallized structure in the CTX-1
at left is softer than the cold worked
and aged CTX-1 and about the same hardness
as the fusion zone. Inconel 718 mixed
grain structure is typical of aged
material.   45

the weld zones are about .03 in., one can say that the weld zone
elongated plastically about 10%. This confirmed the fact that the
welds and the heat affected zone had appreciable ductility. Of
course, there was little reduction of area at the fracture.

The eight test bars after fracture are shown in Figure 3.13.
As evident, the laminations mostly failed in the recrystallized zone
shown in the etched metallographic sections. The failures were 45°
shear fractures indicating considerable deformation prior to frac-
ture. Some of the fractured surfaces showed the odd "oyster shell"
areas as shown in Figure 3.14. Although the exact nature of these
areas is not known, there is no obvious correlation between the
incidence of these areas on the fractured surface and the measured
strength of the individual samples.

For the eight tensile specimens tested, the following average
results were obtained:

Ultimate tensile strength - 187,575 psi
Yield strength (0.2%)   - 167,300 psi

Although the test results were good, it was questionable if these
figures could be used for design purposes since the samples were not
circular in cross-section. Moreover, each test consisted of pulling
the 15 or so laminations generating stresses at the joint of an ex-
tremely complex nature. Thus, only a general level of circumferential
strength could be inferred for the containment ring. It was also
understood that the stress distribution in an actual ring could be
somewhat different.

3.2   PARTIAL SHRINK RING

The next stage in the component development phase was to
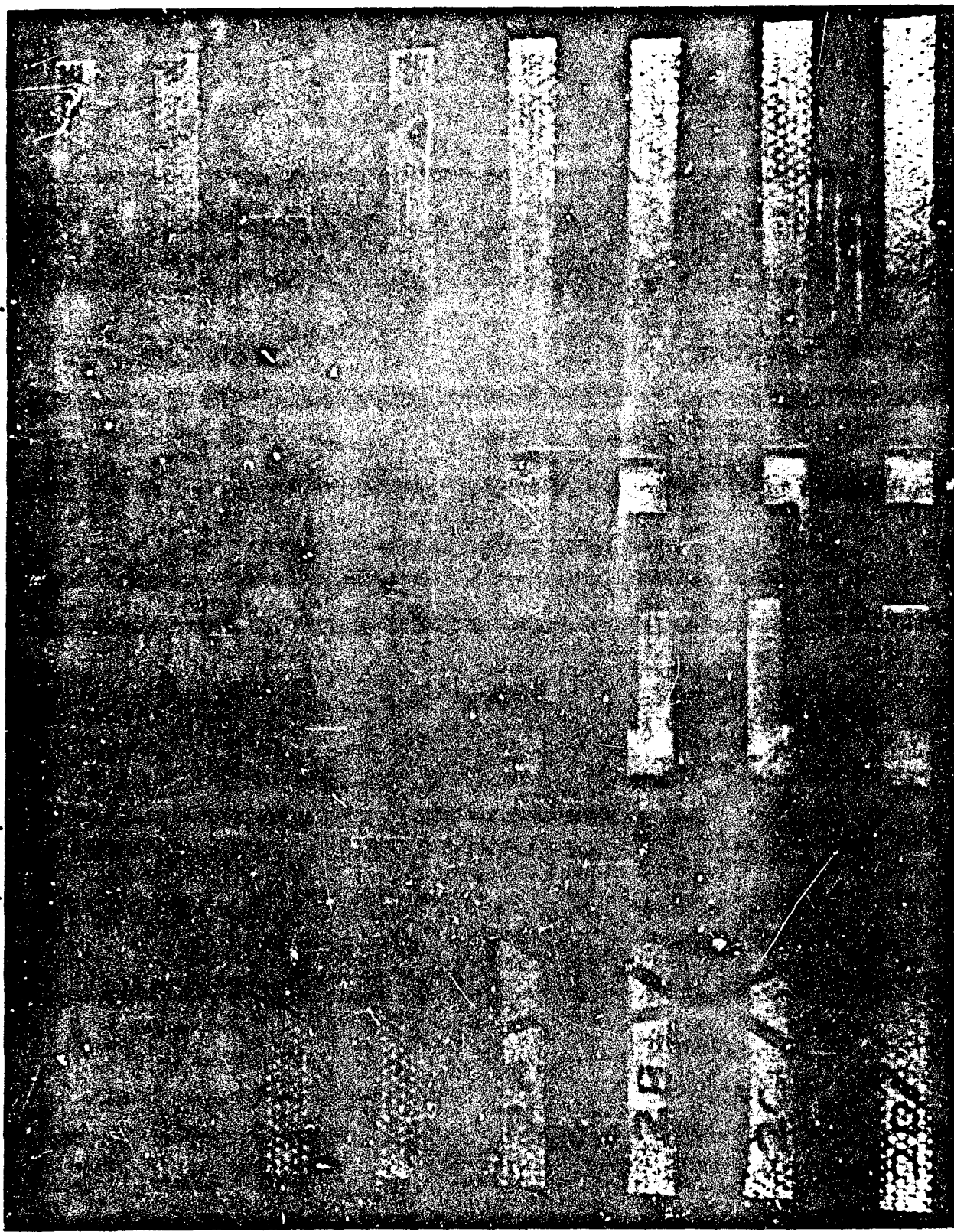fabricate a partial shrink ring and develop a process to drill the

46

Figure 3.13 Fractures of tensile samples cut from weld samples 1 & 2. Most of the fractures occurred in the recrystallized areas of the CTX-1 laminations, while the remainder occurred in the fusion zone near the 718 material.
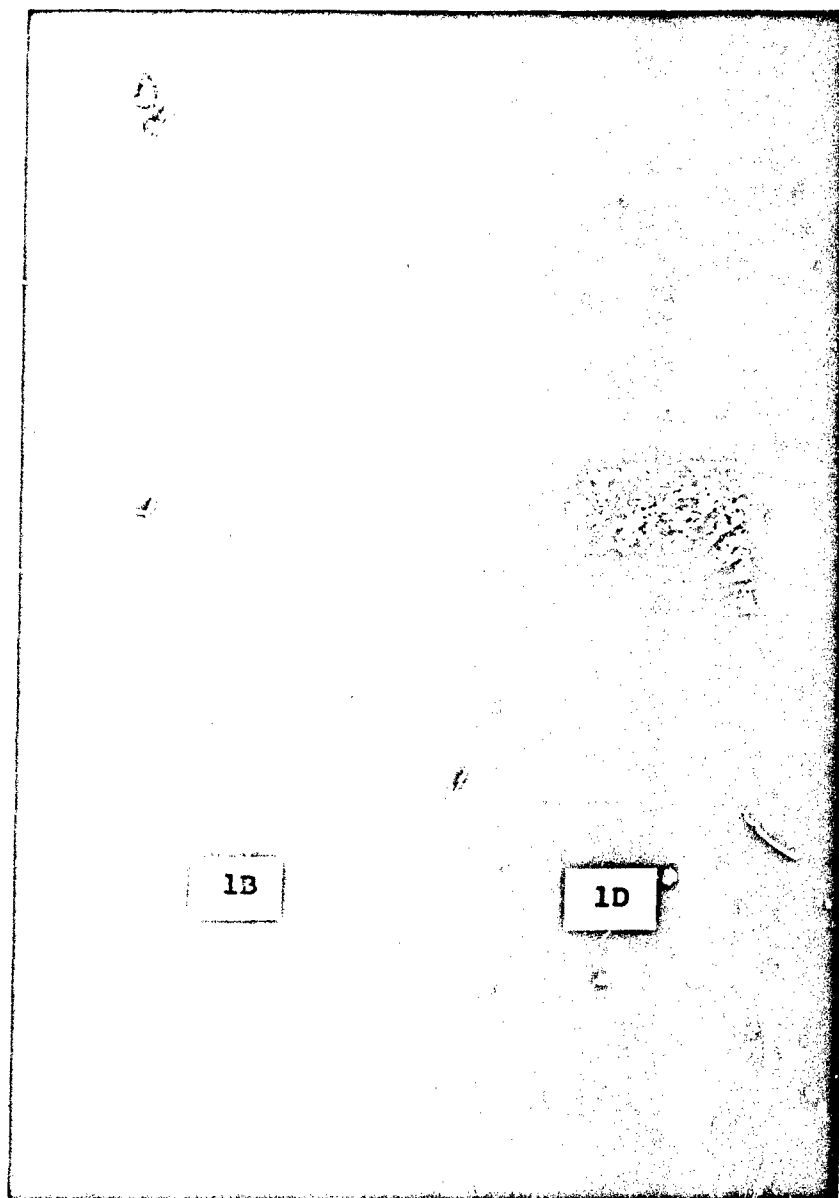
Figure 3. 14

Fractures of samples 1B, left, and
1D, right, showing "oyster shell"
defects in fracture surface.

48

required amortisseur holes in the laminated segments. For this pur-
pose a trapezoidal die was made to stamp CTX-1 laminations. The
same die was later used in the fabrication of the actual ring. The
laminations were stacked, held in place, and TIG welded at the top
and bottom to form a manageable segment as shown in Figure 3.15. Two
such segments were placed in conjunction with three solid bars of
Inconel and electron beam welded to form a partial ring. This ring is
shown in Figure 3.16 after welding. The ring was then cut at various
axial locations and checked for weld deficiencies but none were detected.

The amortisseur holes were to be drilled about an inch deep.
Since the diameter was to be .06" no ordinary drilling bit could
be used. Wire electrical discharge machining appeared to be the most
appropriate process. Using deionized water as the cutting solution,
several holes of various diameters were bored successfully in one of
the sections cut from the partial shrink ring, as shown in Figure
3.17. This section was examined in house to determine the digression
of the hole over the 1 in. axial length and found to be minimal. It
was also suggested that further examination be done to evaluate the
extent of a possible recast layer surrounding the electrical discharge
machined holes.

For this purpose, the cross-section of the laminated segment
was metallographically prepared and examined under light microscope
in the unetched and the etched state. No recast layer was observed
at this point, but it was noted that any recast layer could have been
masked due to a "dimpling" effect at the edges of the holes from the
EDM process. Photographs A through D of Figure 3.18 show poor re-
solution at the edges of the holes. Photograph E shows a representa-
tive field cf the general structure.

The part was then sectioned longitudinally in a plane where
both a small and a large hole could be examined. The specimen was
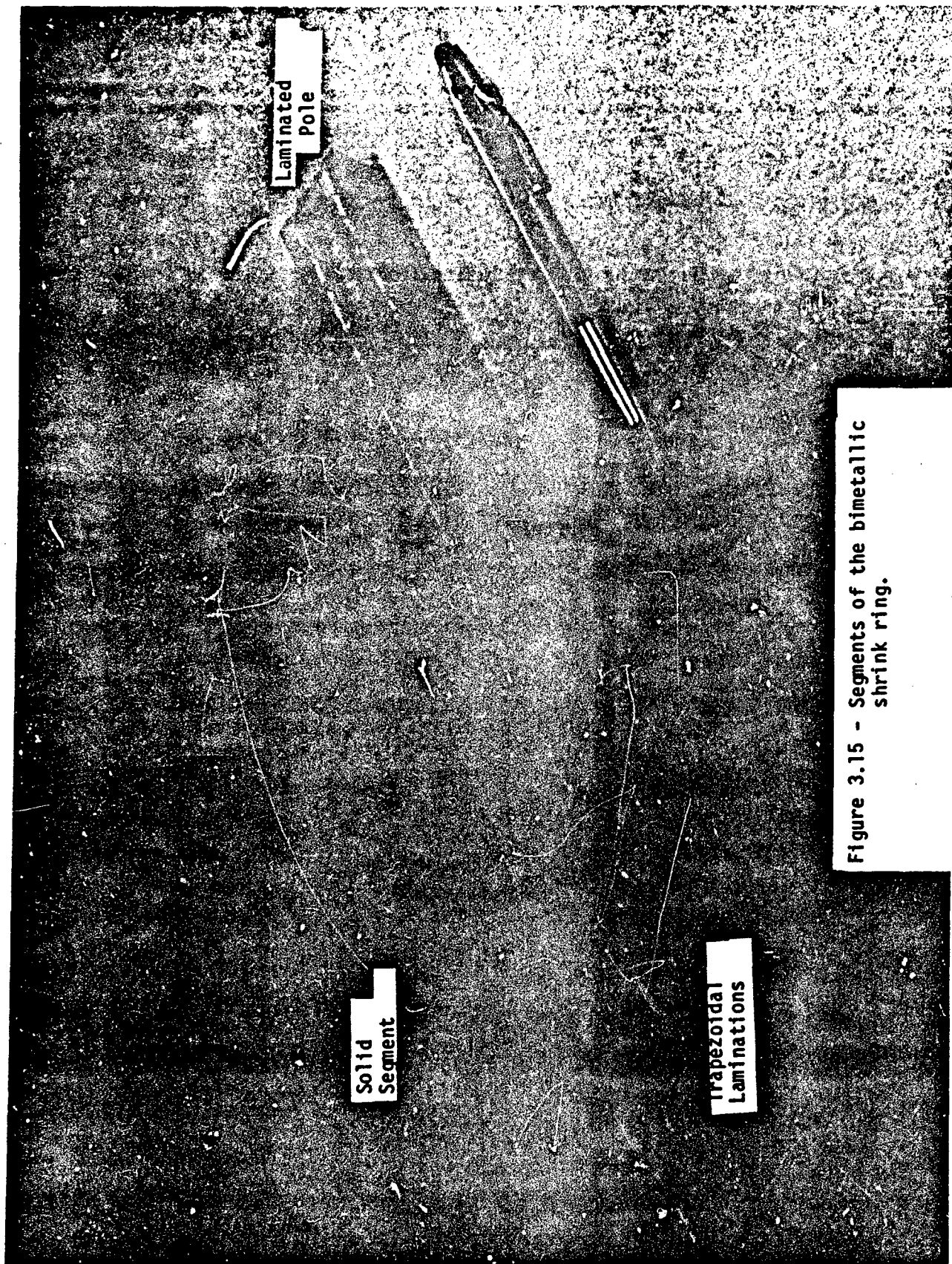ultrasonically cleaned and prepared for evaluation. A recast layer

49

Laminated Pole

Solid Segment

Trapezoidal Laminations

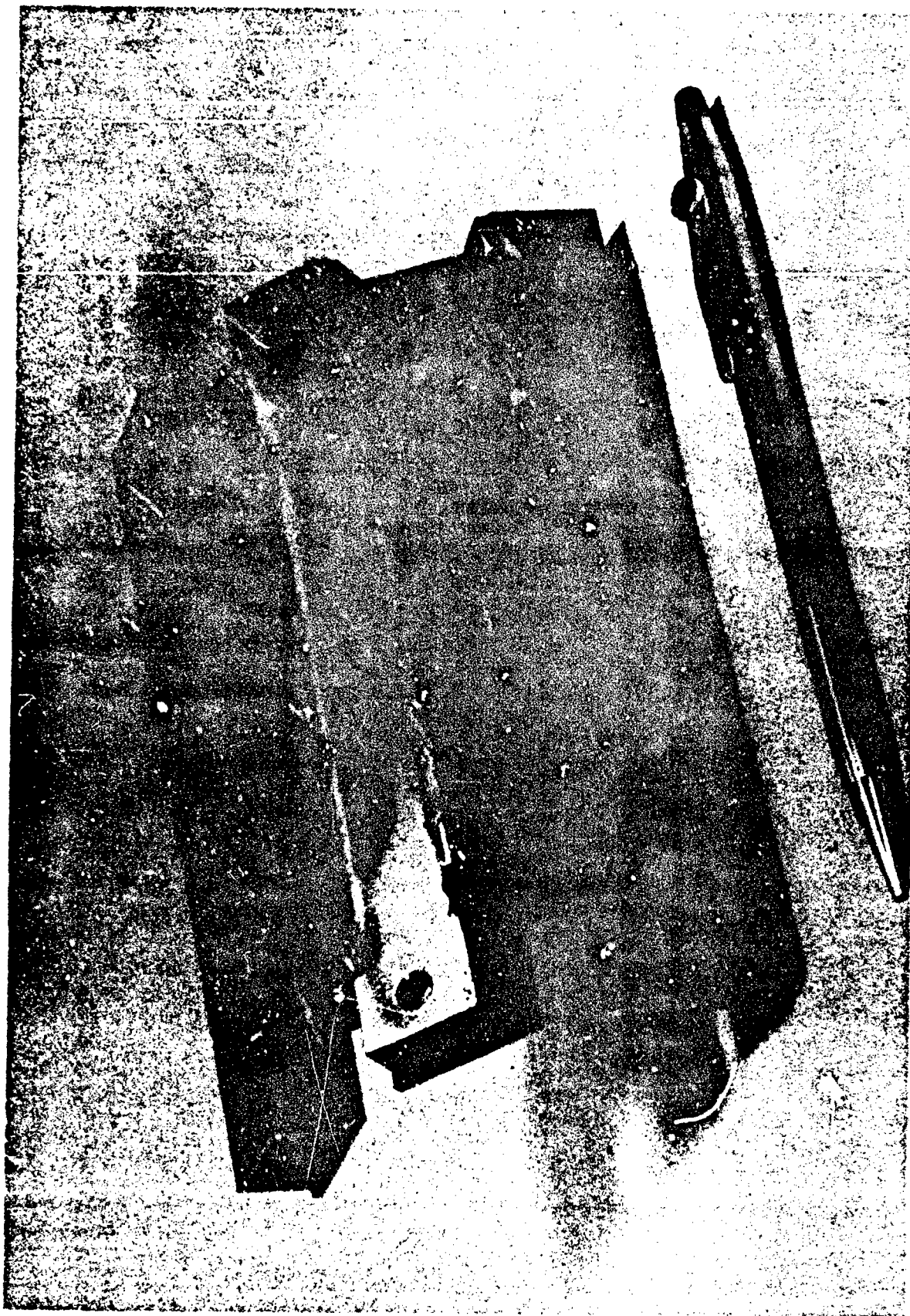Figure 3.15 - Segments of the bimetallic shrink ring.

50

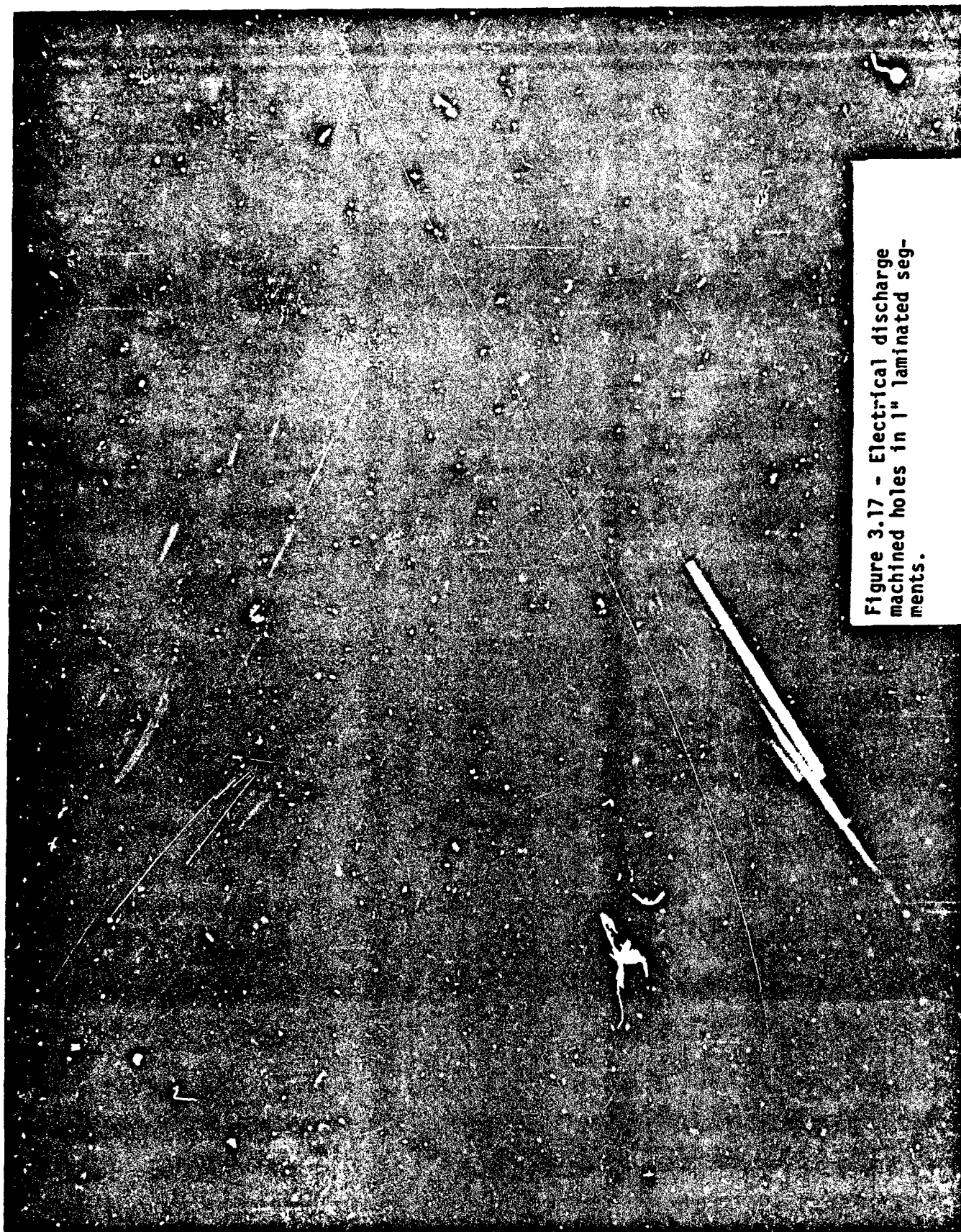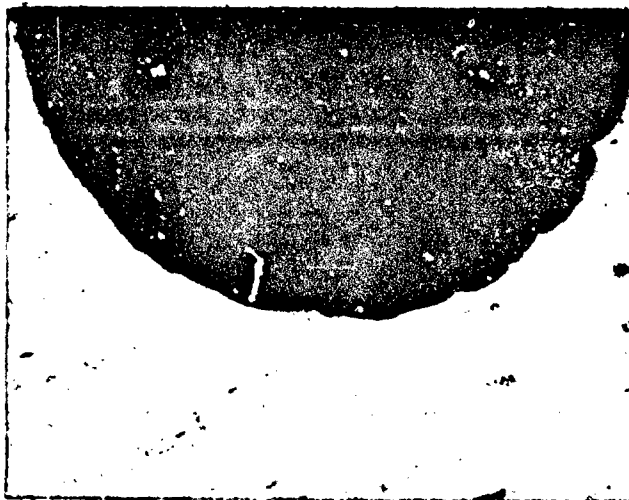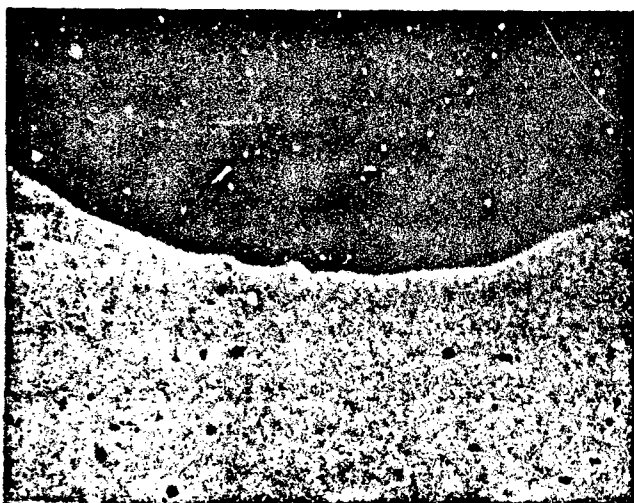Figure 3.16 - Partial shrink ring made from two laminated magnetic segments and three solid non-magnetic segments.

51

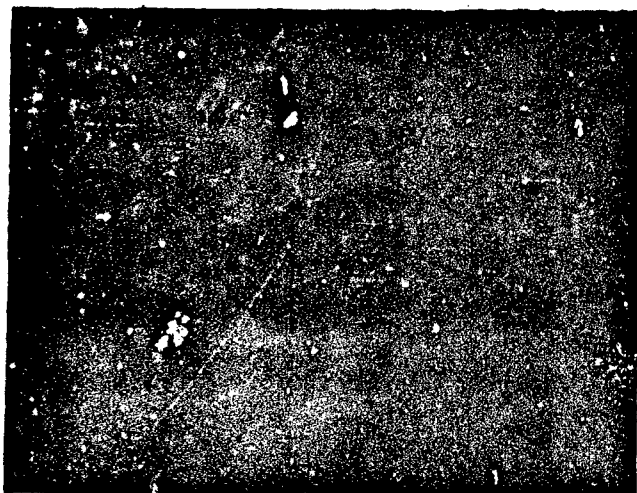Figure 3.17 - Electrical discharge machined holes in 1" laminated segments.
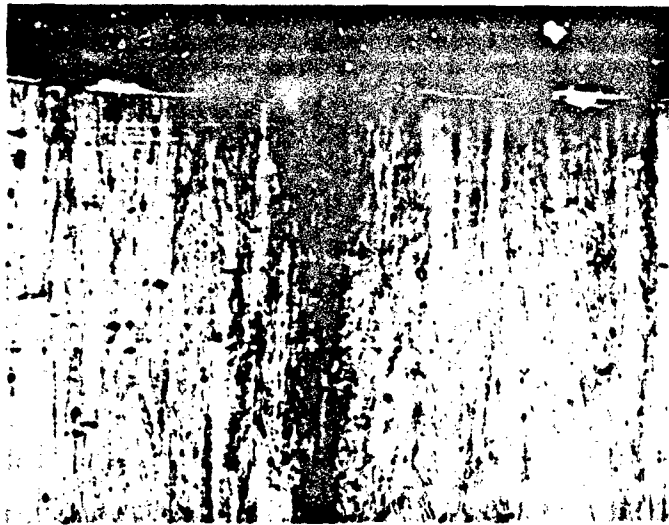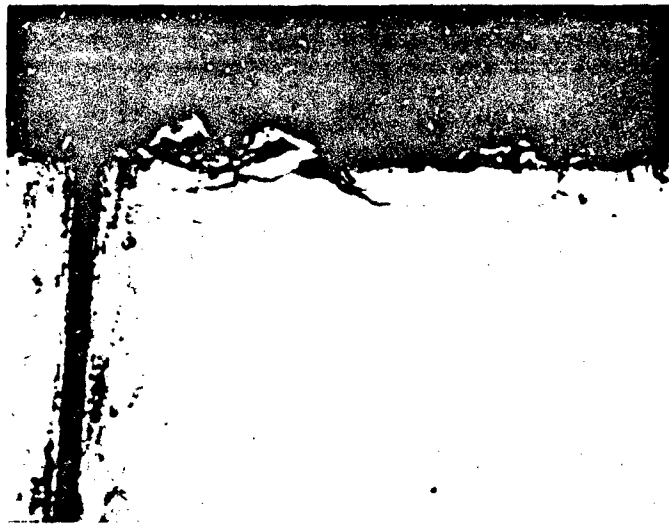
A. small hole - unetched
B.   "   "   - etched
C. large hole - unetched
D.   "   "   - etched
E. representative structure

Mag: 100X   Etchant: Glyceregia

Figure 3.18   Laminated Part - Pyromet CTX-1 Alloy, Representative Photomicrographs of Cross Section.
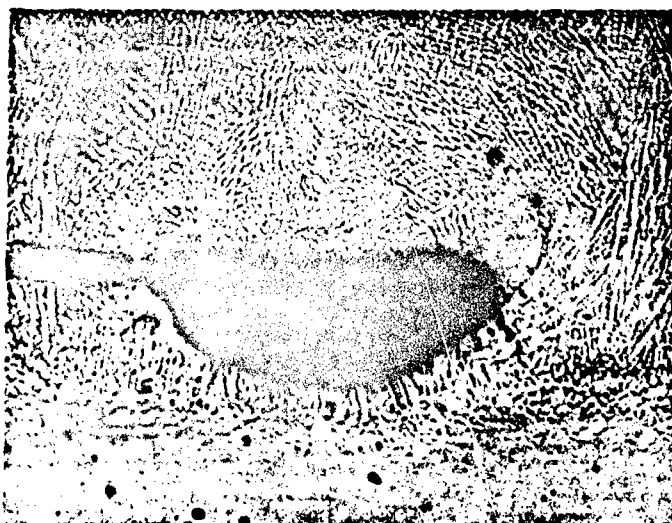
A. small hole

B. small hole - crack area

C. large hole

Mag: 200X   Etchant: Glyceregia

Figure 3.19   Laminated Part - Pyromet CTX-1 Alloy
Longitudinal Views of Damper Holes

A. Cross sectional view

B. Longitudinal view

Mag: 100X   **Etchant: Glyceregia**

Figure 3.20   Laminated Part - Pyromet CTX-1 Alloy
                 Photomicrographs of Weld Areas.
                 Note weld porosity in Cross Section View (A) and
                 also grain recrystallization in heat affected zone
                 shown in Longitudinal View (B).

and also a layer of debris from the machining process was evident, as shown in photos A and C of Figure 3.19. The large hole and, to some extent, the small hole had an irregular concave condition between the layers at the edge of the hole. The severest condition in the large hole was measured to be under 0.003" on the radius. The small hole had an occasional crack about .001" deep. This is shown in photograph B of Figure 3.19. Thus, it was concluded that the recast layer condition could be eliminated by reaming out 0.006" of material after electrical discharge machining the holes.

The welds joining the laminations were also examined on surface transverse and longitudinal planes. Minor porosities were detected on the transverse plane (View A) but the weld appeared sound on the longitudinal plane as shown in Figure 3.20. The recrystallized grain structure on the heat affected zone is very evident in these photographs.

3.3   FABRICATION OF SHRINK RING

The CTX-1 laminations were stamped with the same die as used for the partial ring fabrication. These laminations were stacked and held in place in the fixture, shown as G4 in Figure 3.21, during the TIG welding process. This welding was only to facilitate the handling of the laminated segments. To insure that the segments would fit tightly in the later assembly, the sides of the welded stacks were machined. The non-magnetic segments, shown as P1 in the figure, were made from Inconel-718 stock.

Ten laminated and ten solid segments were assembled, as shown as G2, in a fixture that held these pieces in the correct relationship. The segments were then fused together by electron beam welding. The resulting tube, shown in Figure 3.22 was then machined at the inner and outer diameter to the dimensions shown in G3 of Figure 3.21. This
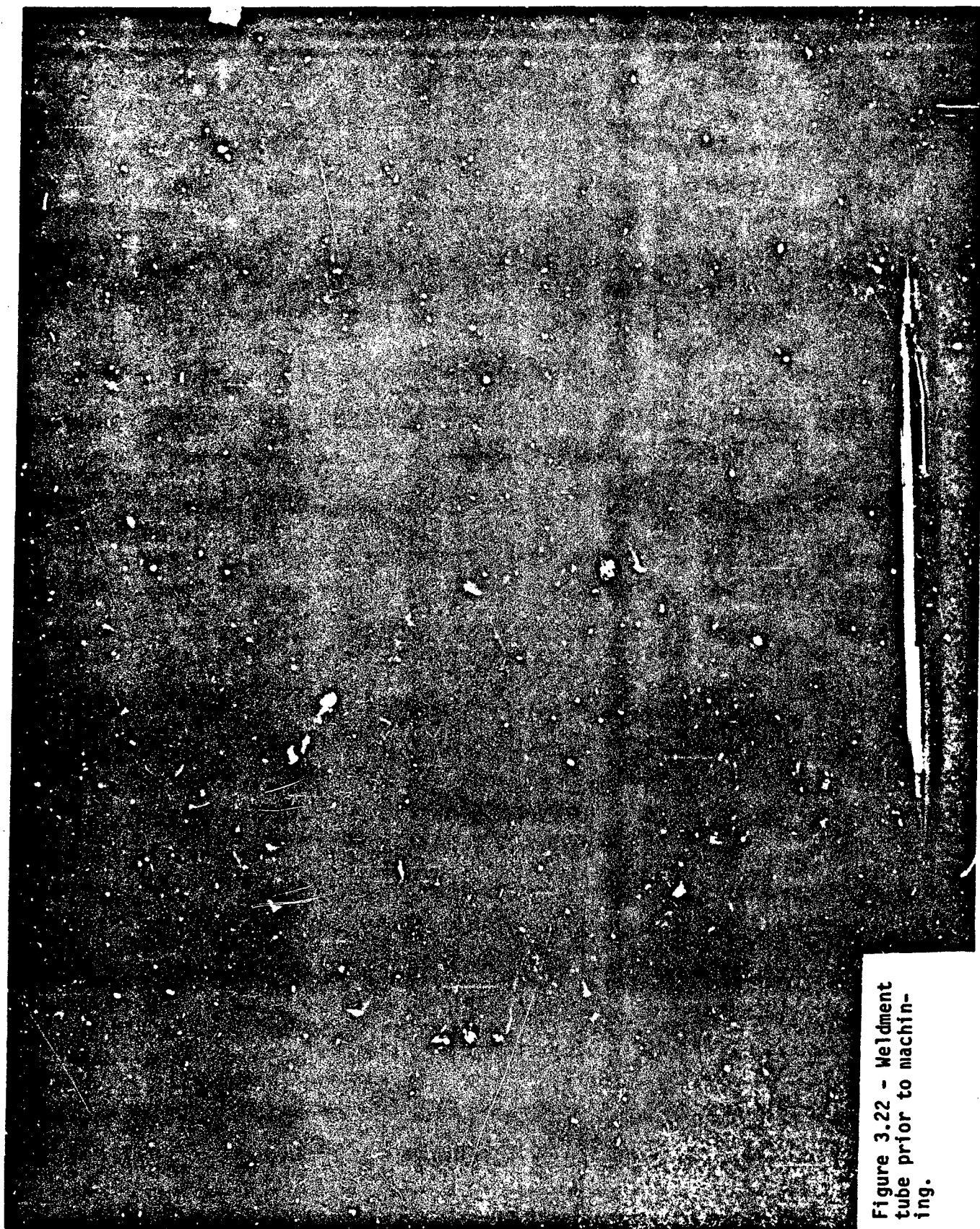
Figure 3.21 - Shrink ring fabrication

57

Figure 3.22 - Weldment tube prior to machining.

Figure 3.23 - Shrink rings obtained from slicing of the weldment tube.

59

tube was then sliced to produce five shrink rings. Using electrical discharge machining, amortisseur holes were drilled in the magnetic segments of these five rings. Figure 3.23 shows one such ring after the machining of the amortisseur holes. The holes were reamed about 0.006" on the diameter to insure that the brittle recast layer was eliminated.

3.4 PROOF TESTING OF THE SHRINK RINGS

As evident from the construction of the shrink ring, the critical component is the welded joints. Thus, before assembling the ring onto the poles, the integrity of these welds were determined. Although, an expandable arbor test was suggested, it was deemed impractical. General Electric's Material and Processes Laboratory was contracted and a split mandrel tensile test was devised. The M&P lab was also commissioned to design and fabricate the proof test fixture and do the actual testing of the shrink rings.

The shrink rings were tested by applying hoop stresses by means of a split mandrel. The two halves of the mandrel were pulled perpendicular to the plane of the split as shown in Figures 3.24 and 3.25. Before the start of the test the mandrel and the hole fixture were inspected and found to be within the tolerances shown on the sketches. In order to insure that the loading was uniform across the axial dimension of the ring eight strain gages were cemented as shown in Figure 3.26. These strain gages were also used to determine the reduction of hoop stresses at locations away from the split of the mandrel due to friction. Two strain gages were connected in series and their output was connected to the X axis of an XY recorder. the output from the load cell was connected to the Y axis. With the rings positioned such that the gages were at 90 degrees to the plane of the split, a load of approximately 45,000 lbs. was applied twice. The ring was then moved through an angle equal to that subtended by one segment and the loading repeated. This process was continued until the gages
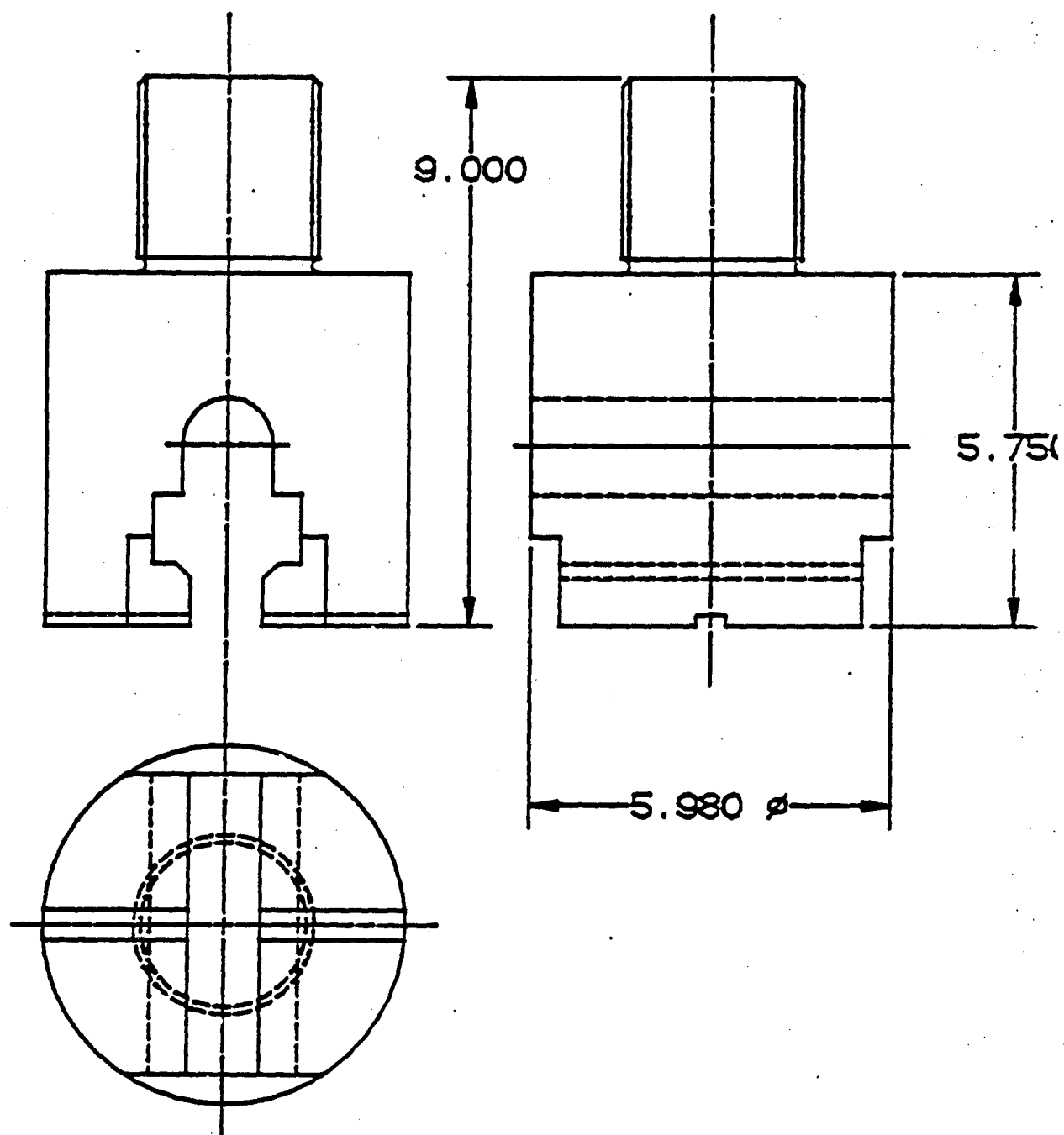
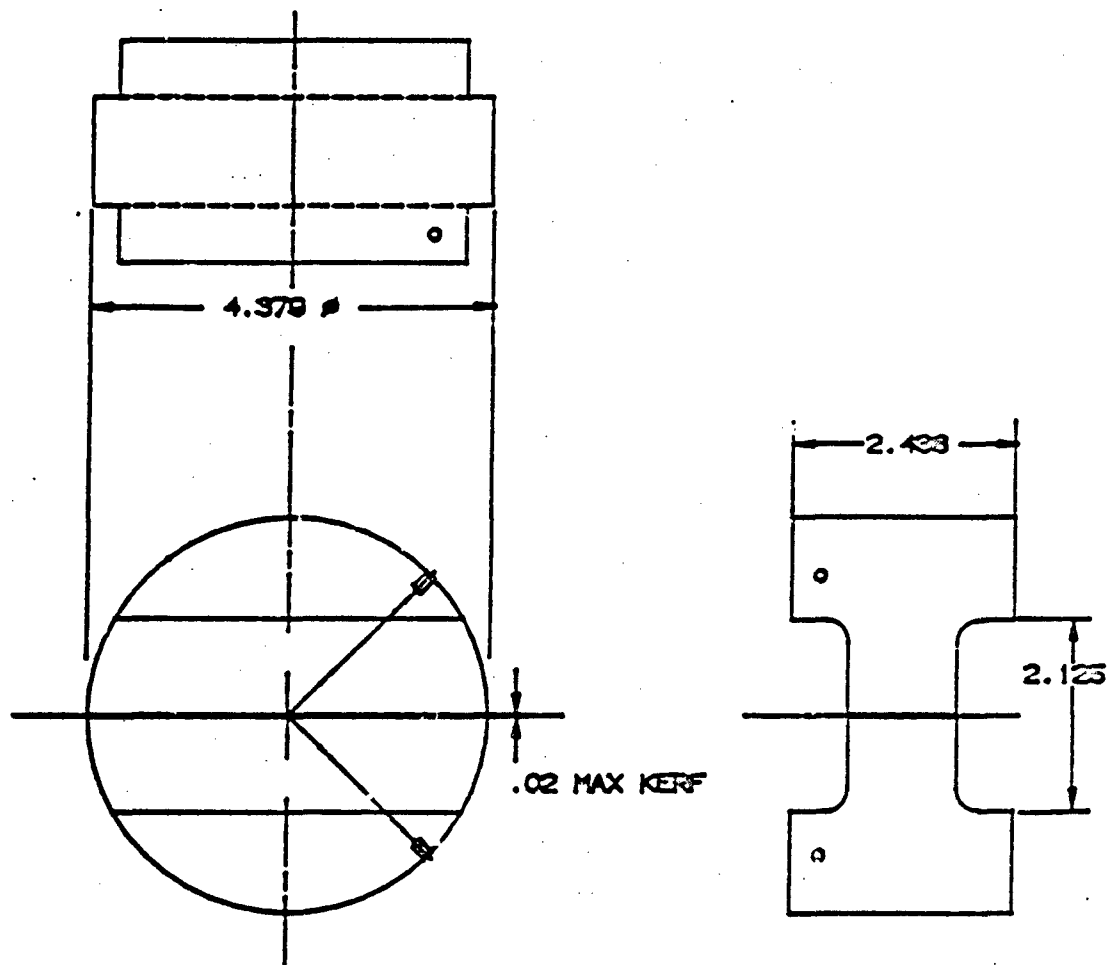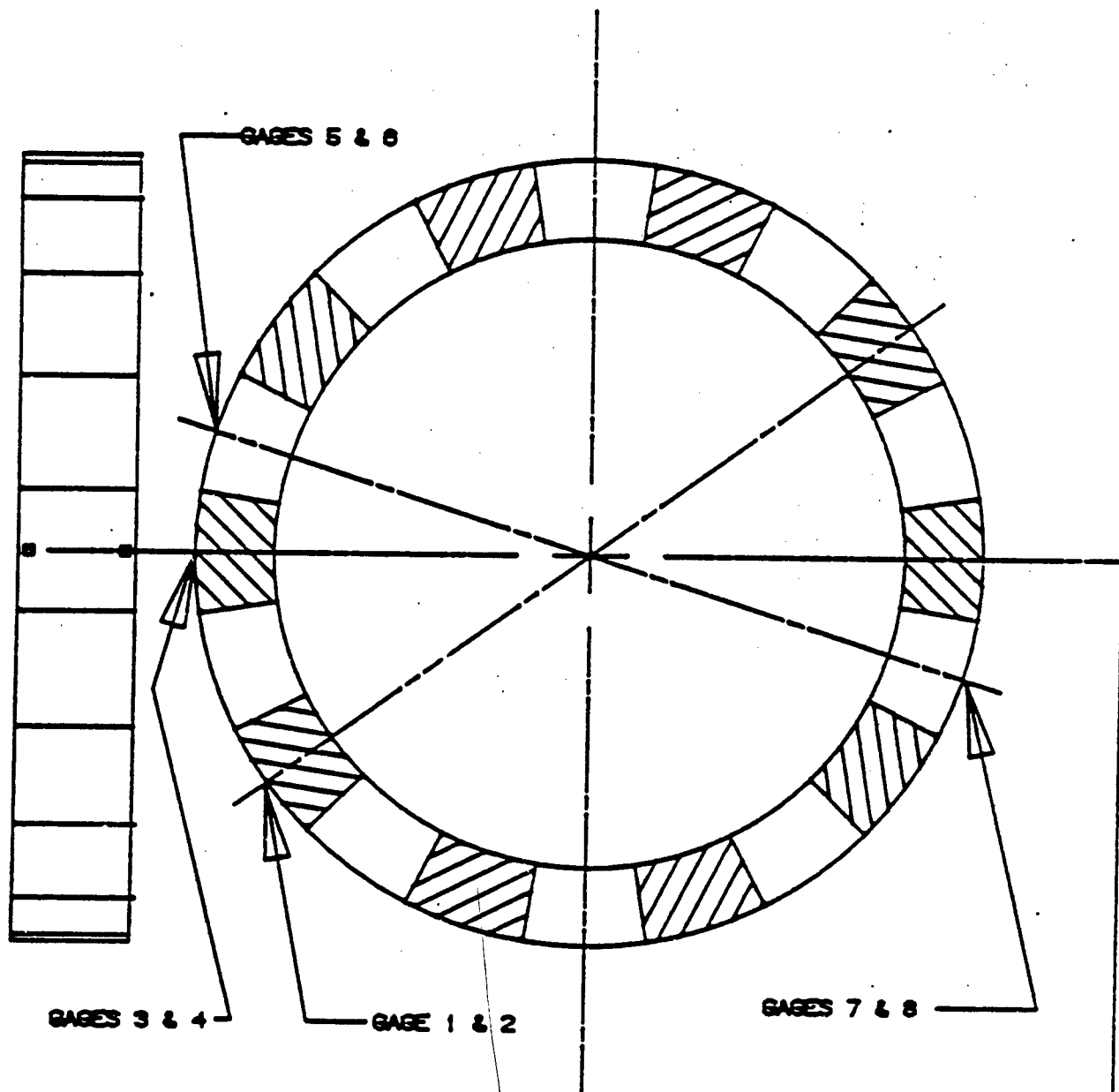Figure 3.24 - Clevis for the proof test fixture

Figure 3.25 - Split mandrel for shrink ring testing

62

GAGES 5 & 6

GAGES 3 & 4

GAGE 1 & 2

GAGES 7 & 8

ALL GAGES LOCATED .140
FROM FRONT AND REAR EDGES
AND CENTRALLY LOCATED ON
EACH SEGMENT

Figure 3.26 - Location of the strain gages

63

were in the plane of the split. The stress-strain records indicated
a large amount of bending when the gages were in the plane of the split.
Since the welds would be located one-half segment away from the split
during proof testing, the gages were moved to this location and the
load applied. The records indicated that the bending was signifi-
cantly lower in this position. Moreover, the gages farthest from
the split indicated that the effect of friction is reducing hoop
stress was less than 10%.

To determine the yield strength, one of the shrink rings was
taken to destruction. The ring was lubricated with Molykote and
positioned such that the center of the laminated segment coincided with
the split in the mandrel. A diametral extensometer was used and its
output was plotted versus stress by the XY plotter. The graph obtained
is shown in Figure 3-27 and it is evident that the ring started to
yield at 64,000 lbs. and failed at 97,000 lbs. The test setup is
shown in Figures 3.28 and 2.29 and the destroyed ring is shown in Figure
3.30. The following results were obtained:

    Proportional limit   136,000 psi
    Yield strength (0.2%)   187,000 psi
    Ultimate tensile strength   206,000 psi

In the next series of tests the remaining four rings were proof tested
at a level corresponding to 130,000 psi. The loading was applied
gradually and the ring was rotated between the loadings such that the
same segment was never at the split until all other segments had
been subjected to the pull.

All of the rings passed the proof testing and no change in
dimensions were noted. This confirmed the effectiveness of the weld
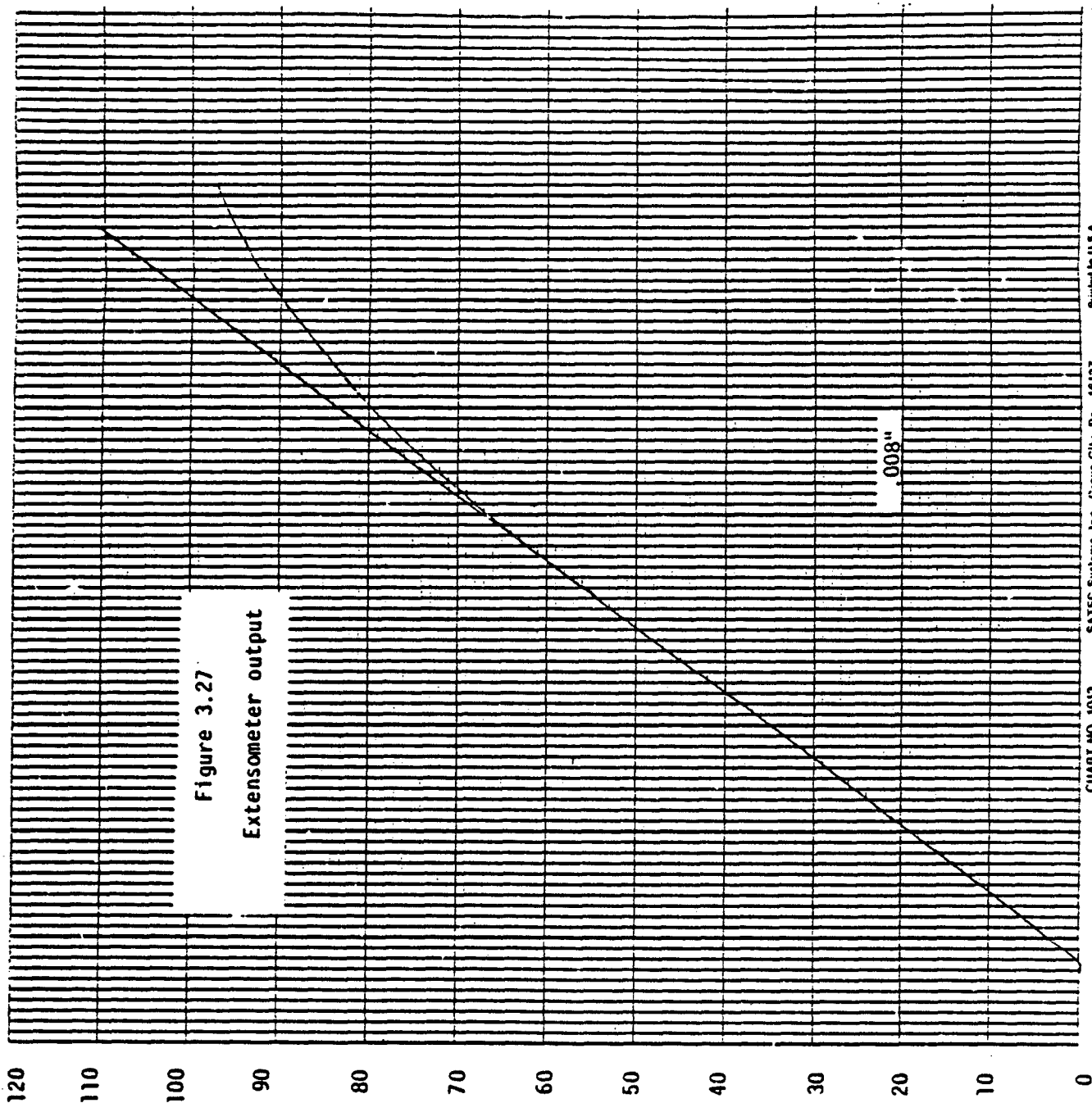joints and eliminated the possibility of rotor failures during actual
operation.

Figure 3.27
Extensometer output

Force (KIPS)

.008"

CHART NO. 1012   SATEC Systems, Inc., Grove City, Pa.   16127   Printed in U.S.A.

120 110 100 90 80 70 60 50 40 30 20 10 0
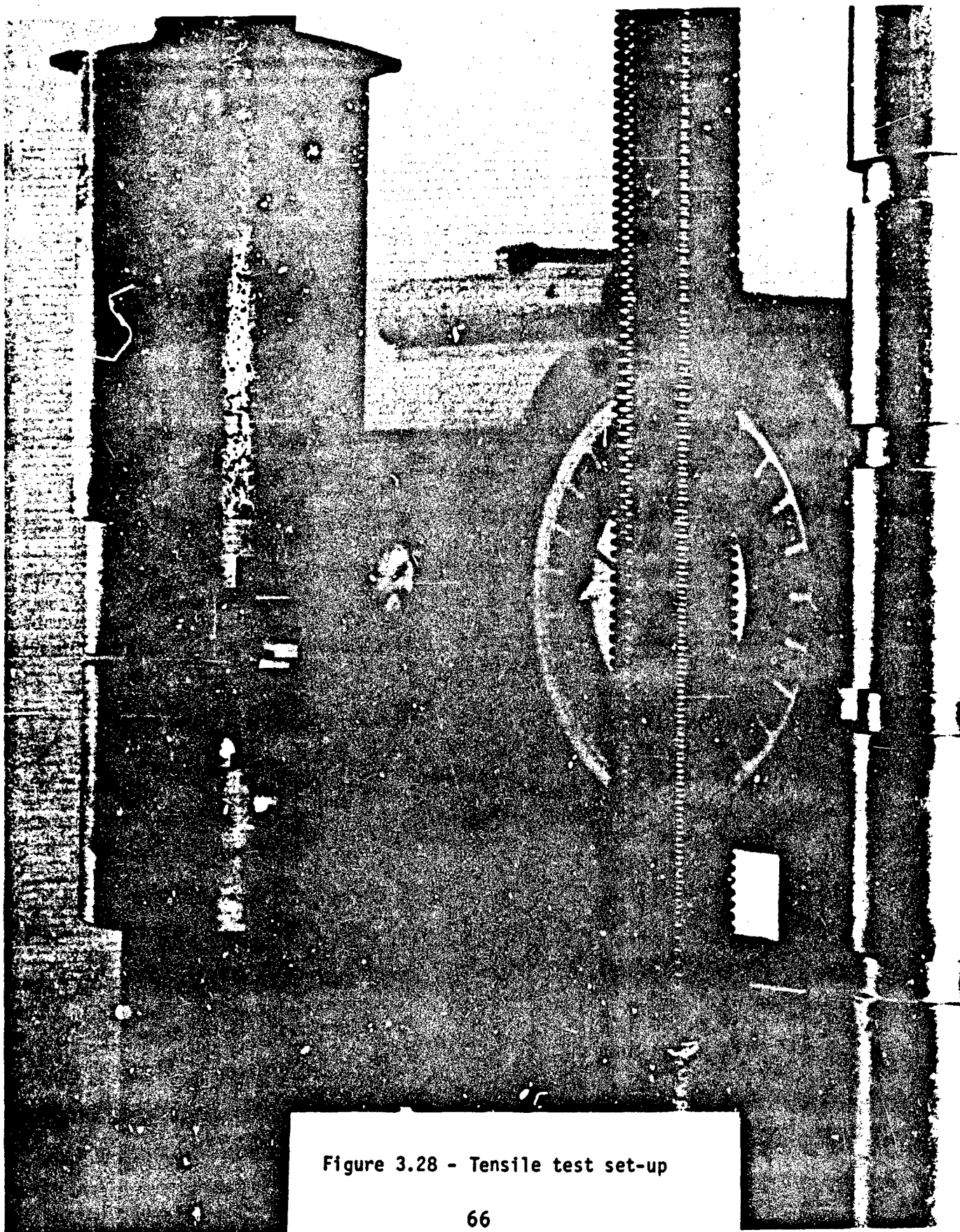
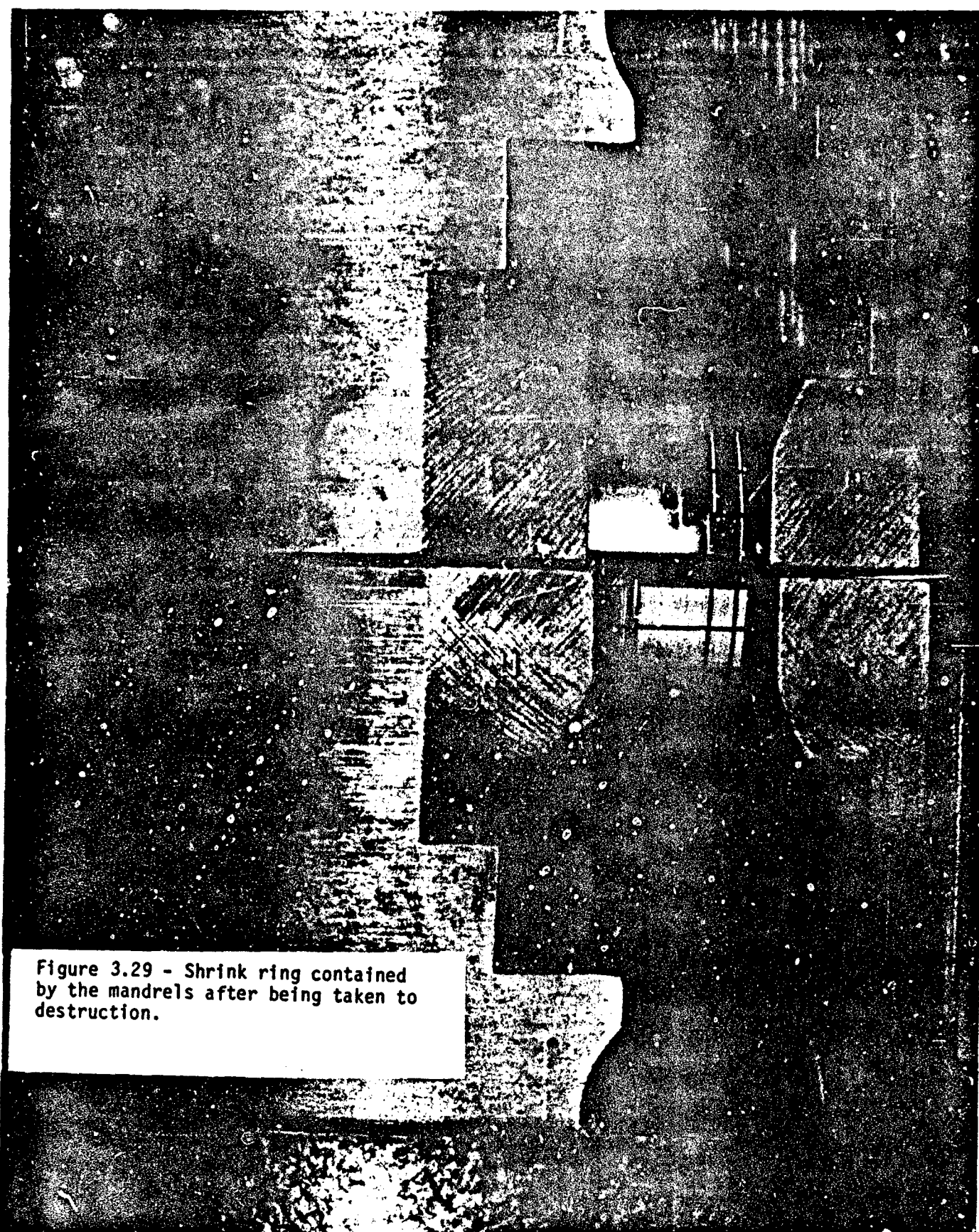65

Figure 3.28 - Tensile test set-up

66

Figure 3.29 - Shrink ring contained by the mandrels after being taken to destruction.
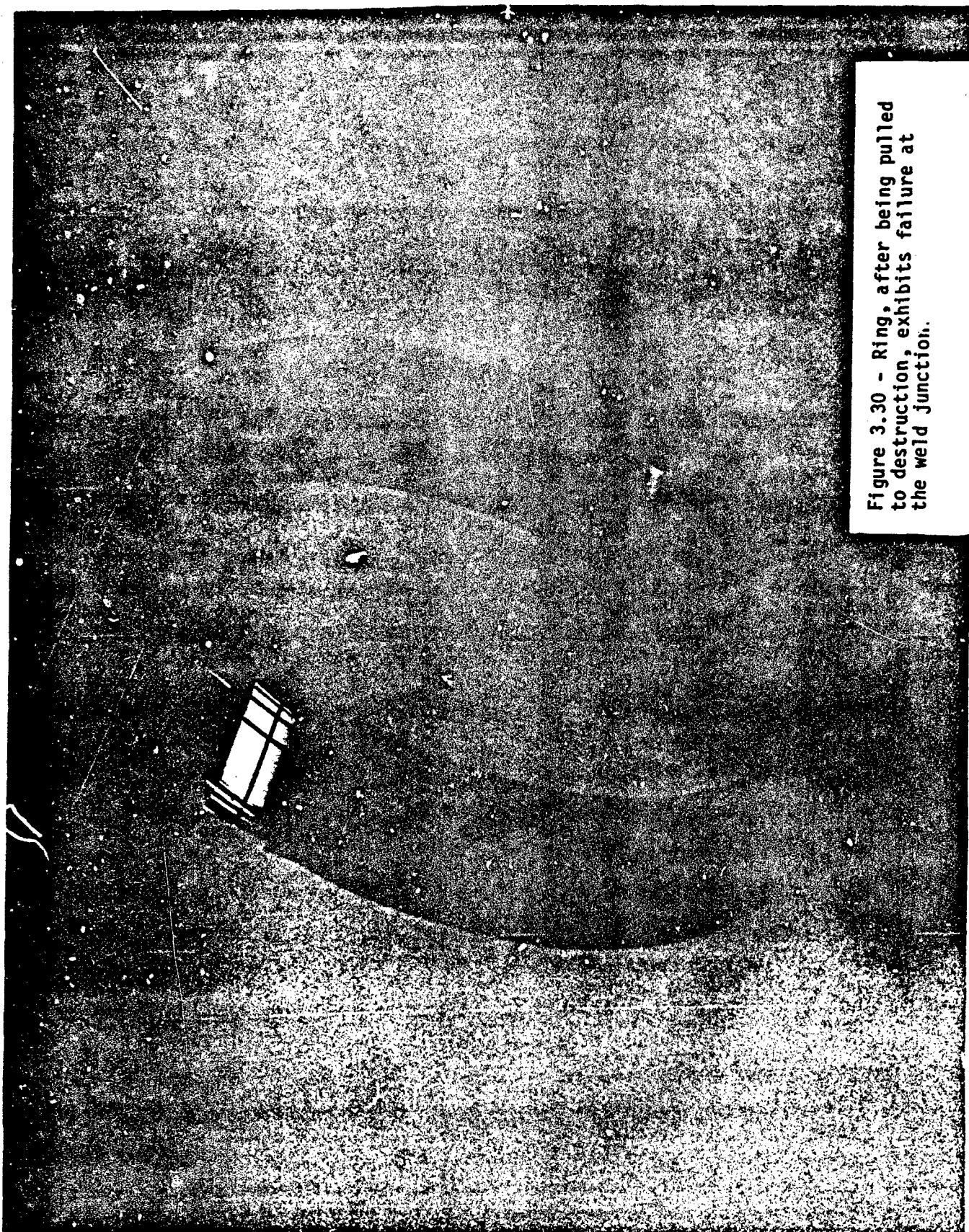
Figure 3.30 - Ring, after being pulled to destruction, exhibits failure at the weld junction.

68

SECTION IV
GENERATOR DESIGN

4.1   GENERATOR SPECIFICATIONS

The containment technology developed in this program was demonstrated in a breadboard generator of the type used in the variable speed constant frequency (VSCF) systems. As shown in the block diagram (Figure 2.1), the wild frequency output from the generator is converted to precise 400 Hz power by means of a cyclo-converter. The electromagnetic design of the permanent magnet generator required an analysis of the characteristics and limitations of the rotor, stator and the converter. The four significant limitations were:

i)   the minimum generator frequency acceptable for for required converter performance

ii)   the maximum rotor diameter possible without exceeding the strength of the containment ring

iii) the maximum commutating inductance for stable converter operation

iv)   the requirement of minimum electrical and mechanical losses

The specification for the 30/40 KVA system is given in Table 4.1. The generator must have a higher output than the required system rating to compensate for the power factor and the cycloconverter efficiency. Typically, because of the phase retarding approach used in the cycloconverter operation, the generator KVA is approximately 33 percent higher than the system output. Table 4.2 gives a summary of the generator/converter interface requirement for this 30/40 KVA, 115 V, 3 phase, 400 Hz system.

Since no converter design or fabrication was required, the generator was designed as a split system whereby the generator and the converter would be separate assemblies. An example of a split

69

SYSTEM RATING

CONTINUOUS	40 KVA, 115/200 VOLT, 400 HZ 3 PHASE-4WIRE, 0.75 PF PER MIL-E-23001
5 MINUTES	45 KVA, 0.75 TO 0.95 PF
5 SECONDS	60 KVA, 0.75 TO 0.95 PF
SPEED RANGE	15,300 RPM TO 26,250 RPM, CCW WHEN VIEWED FROM DRIVE END (1.7:1 SPEED RANGE)
ENVELOPE	SAME AS F-18 SYSTEM

Table 4.1.   System Specifications

70

SYSTEM		GENERATOR					
KVA	PF	V(L-N) MIN.	KVA	DISP. PF	FUND. AMPS	RMS AMPS	DUTY
0	--	155	25.1	0.1	27	30	CONTINUOUS
40	0.75	155	43.7	0.74	47	52	CONTINUOUS
	0.95	155	53.0	0.76	57	63	CONTINUOUS
45	0.75	150	47.7	0.74	53	58	5 MINUTES
	0.95	150	56.7	0.78	63	69	5 MINUTES
60	0.75	145	64.4	0.74	74	82	5 SECONDS
	0.95	145	72.2	0.83	83	91	5 SECONDS

Table 4.2

Generator/Converter Interface Requirements

71

design is the 60 KVA starter generator system shown in Figure 4.1. The generator layout, Figure 4.2, shows the stator, rotor and the disconnect housed inside a F18 stator frame. This was done so that the F18 test frame could be used for generator testing. An outline of a generator test frame is shown in Figure 4.3.

The flux path in the permanent magnet machine is shown in Figure 4.4 for circumferentially energized magnets. The north poles of the magnets face each other in the circumferential direction as do the south poles. The pole, a magnetic member positioned between the magnets, carries the flux radially to the magnetic segment of the shrink ring. The flux then travels across the air gap into the stator laminations. The non-magnetic segment of the shrink ring prevents leakage and forces the flux through the air gap.

The rotor disc is shown in Figure 4.5 where the shrink ring is bimetallic with laminated magnetic segments. In addition three amortisseur bars are incorporated in each magnetic segment. These features of the shrink ring lead to the minimization of rotor pole face losses and generator commutating inductance. The hub is made non-magnetic to prevent flux leaking to the shaft. Three such discs are mounted on the shaft with an interference fit to form the rotor.

COMMUTATING INDUCTANCE

The commutating inductance is defined as the inductance per phase that produces voltage loss during commutation of current from one phase to another. It is the most significant machine reactance when considering rectifier type loading of the generator. It governs the generator behavior to transient energy and directly affects converter performance. Higher reactance requires the converter to dissipate more transient energy and results in higher voltage regulation for the generator. It is desirable to maintain a low voltage regulation in the no load to double load operating range since it minimizes the voltage stress on the SCR's. A high commutating reactance
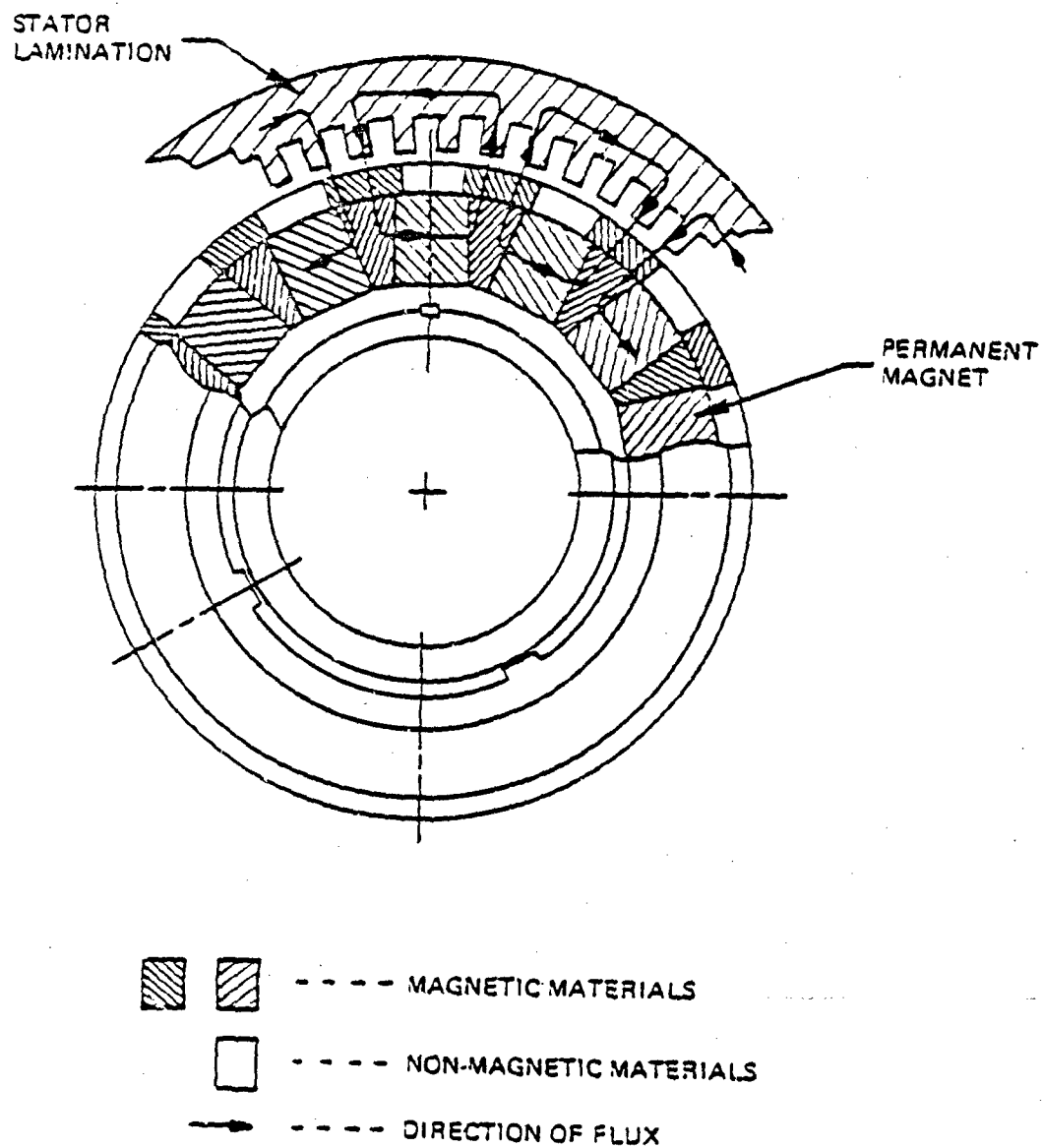
Figure 4.3. Outline of
Generator Test Frame

STATOR
LAMINATION

PERMANENT
MAGNET

MAGNETIC MATERIALS

NON-MAGNETIC MATERIALS

DIRECTION OF FLUX
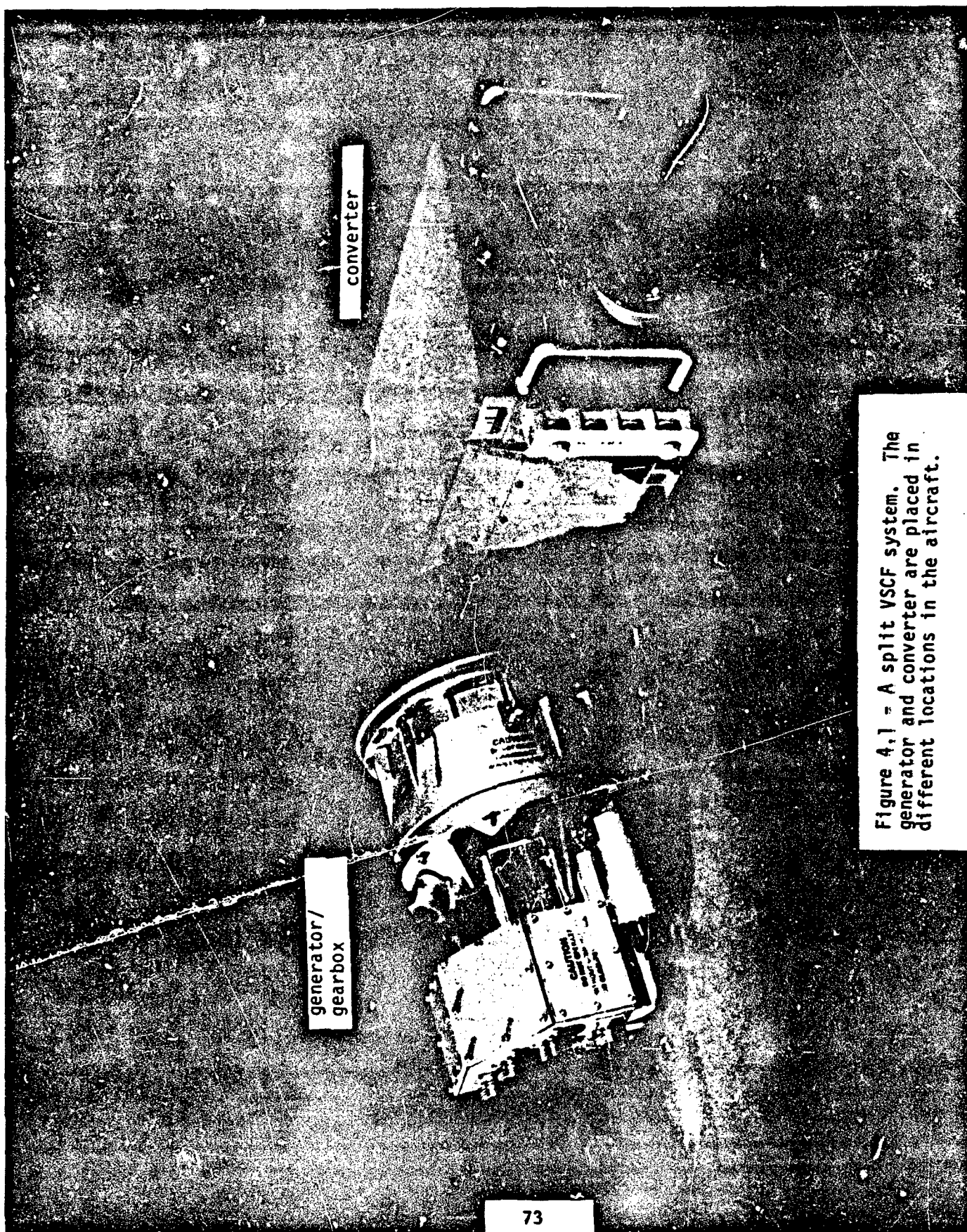
Figure 4.4 - Flux paths in a permanent
magnet generator

converter

generator/
gearbox

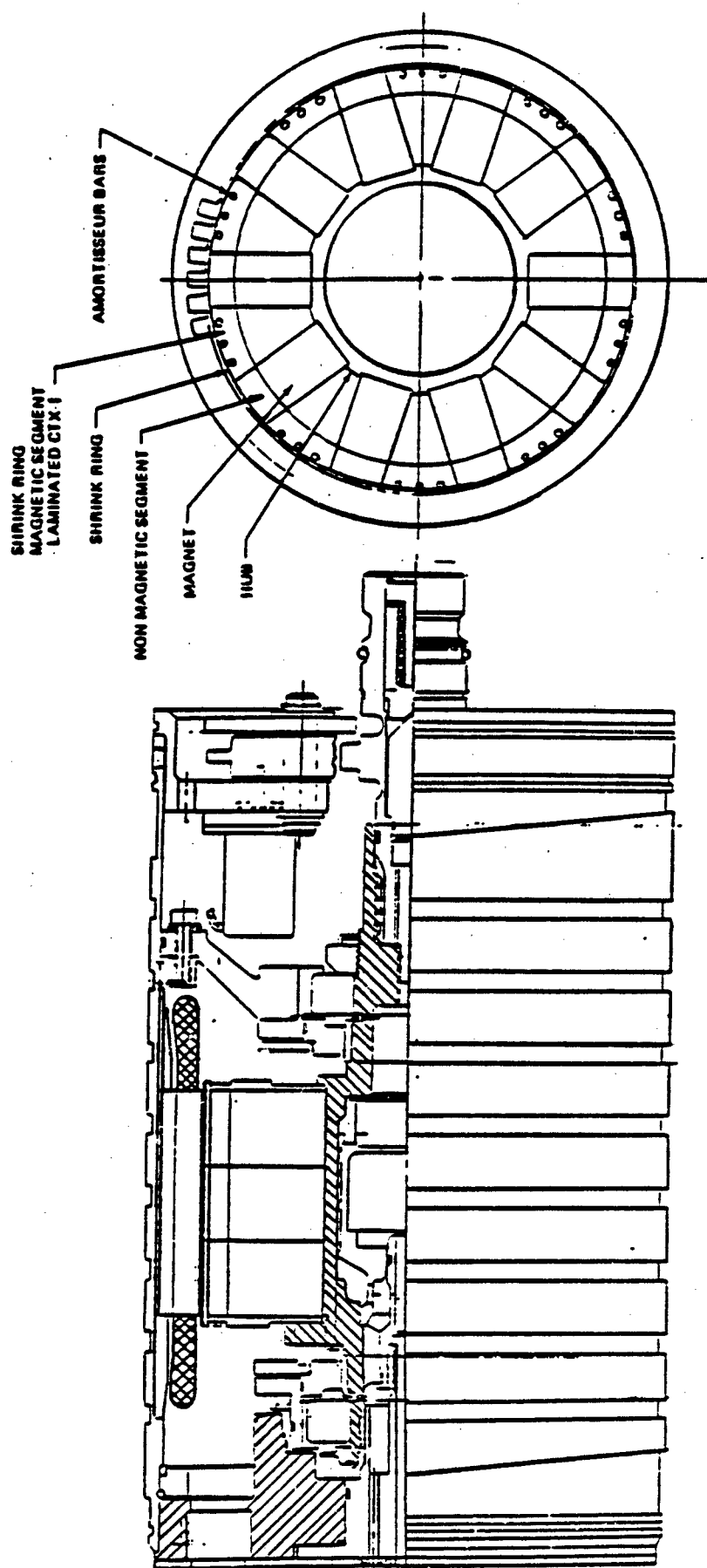Figure 4.1 - A split VSCF system. The generator and converter are placed in different locations in the aircraft.

AMORTISSEUR BARS

SHRINK RING
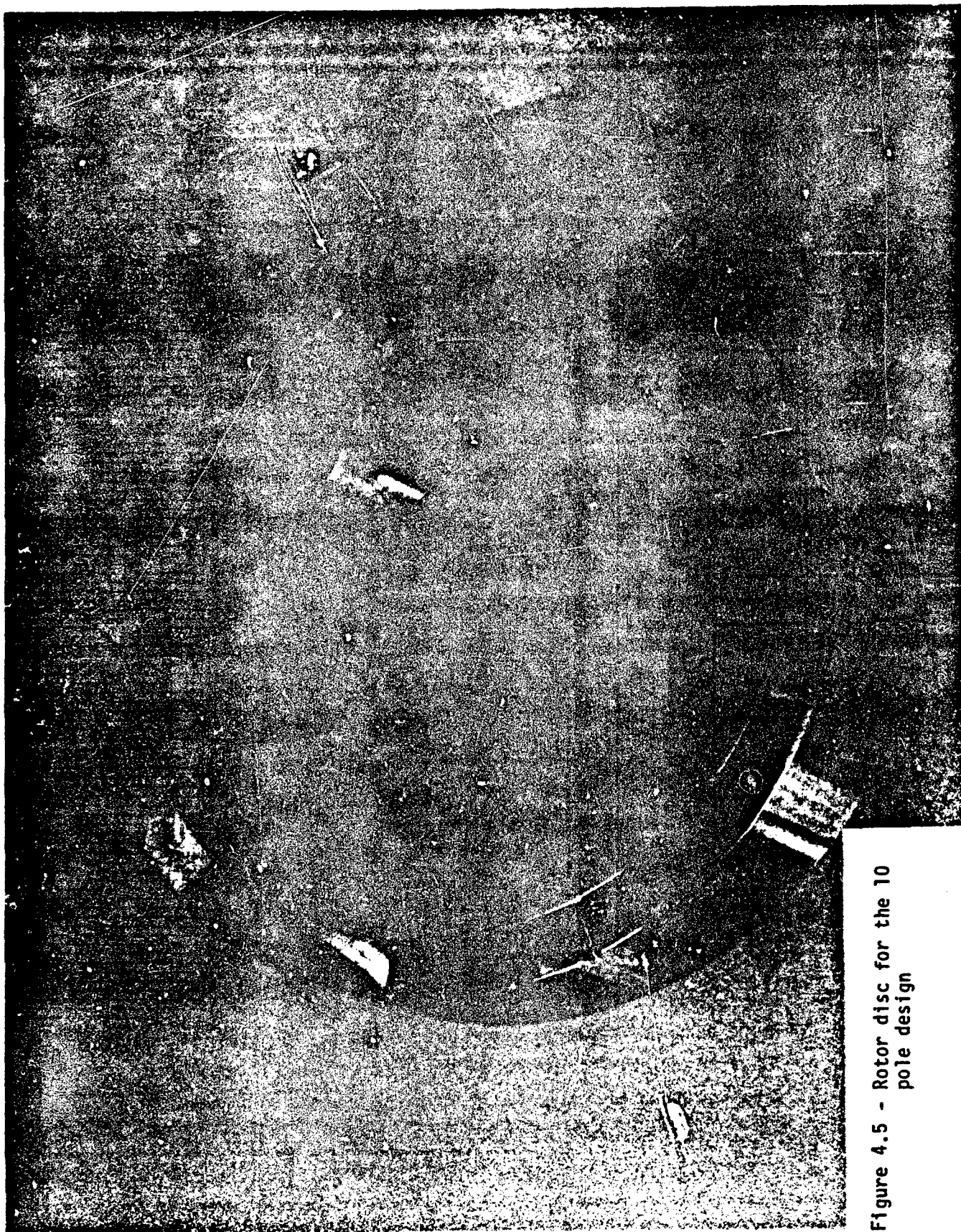MAGNETIC SEGMENT
LAMINATED CTX I

SHRINK RING

NON MAGNETIC SEGMENT

MAGNET

HUB

Figure 4.2 - Generator layout.

Figure 4.5 - Rotor disc for the 10 pole design

also introduces undesirable mutual effects between the converter output phases and, thus, imposes the need for additional control circuitry.

The commutating inductance for a given cycloconverter system is based on calculations and past experience. Since is is a function of the number of phases, base frequency and system rating, the value specified is one that offers the optimum balance between the generator weight and size and the converter intricacy. This value can be obtained from the negative sequence impedance calculation or approximately, from the subtransient reactance calculation. Figure 4. shows the equivalent circuits for the negative sequence impedance in the direct and quadrature axis. As shown, the total reactance is the equivalent of the stator leakage reactance, armature reaction reactance, field leakage reactance and the damper winding leakage reactance. If all resistances are neglected, an equivalent circuit for subtransient reactance in the direct and quadrature axes is obtained.

In figure 4.6 the following nomenclature is adopted.

R_A = stator resistance
R_F = field resistance
R_{KD} = damper winding resistance in direct axis
R_{KQ} = damper winding reactance in quadrature axis
X_L = stator leakage reactance
X_{AD} = armature reaction reactance in direct axis
X_{AQ} = armature reaction reactance in quadrature axis
X_F = field leakage reactance
X_{KD} = damper winding leakage reactance in direct axis
X_{KQ} = damper winding leakage reactance in quadrature axis
X_Z = negative sequence reactance
X_D = subtransient reactance in direct axis
X_Q = subtransient reactance in quadrature axis

78
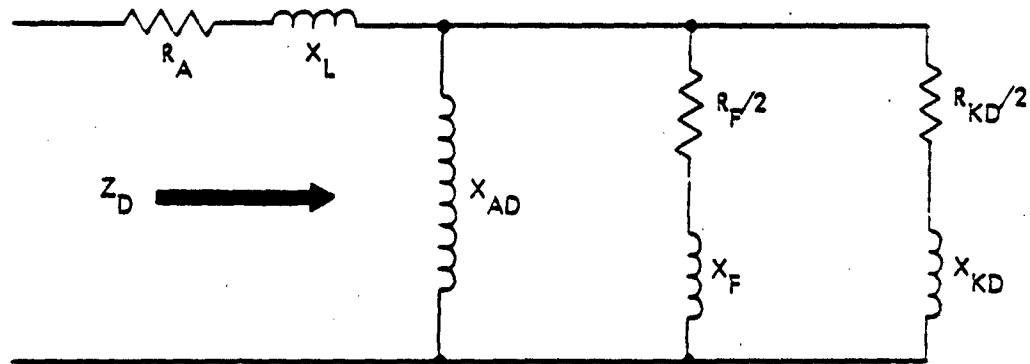
Direct Axis

Quadrature Axis
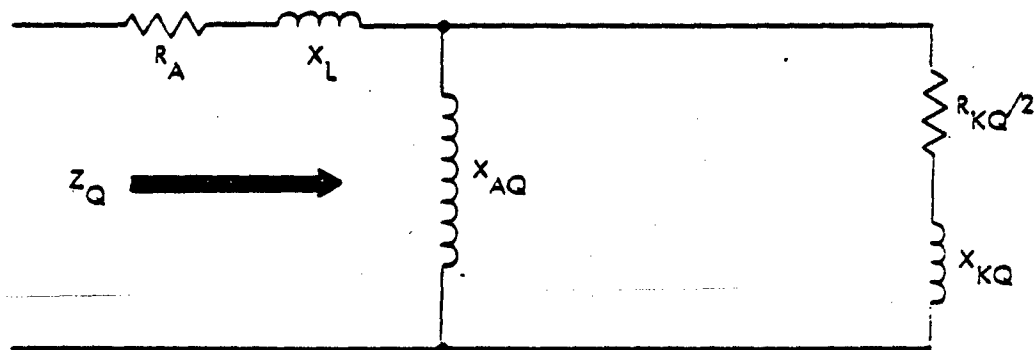
$$Z_2 = 1/2 \ (Z_D - Z_Q) = R_2 - j \ X_2$$
$$\text{OR} \quad X_2 \simeq 1/2 \ (X_D{}'' - X_Q{}'')$$

Figure 4.6 - Negative sequence impedance
equivalent circuits

Z_D = negative sequence impedance in direct axis

Z_Q = negative sequence impedance in quadrature axis

Z_Z = negative sequence impedance

X_C = commutating reactance

The approach taken in lowering commutating reactance is to reduce the individual leakage reactances as much as possible. The first step in this approach is to find common factors having significant influence on all the leakage reactances. The next step is to minimize these factors subject to the machine requirements. In general, all the leakage reactances are proportional to the square of the number of turns per phase and also to the height of iron, i.e.

leakage reactance $\propto$ (turns/phase)^2 (stack length)

It is evident from the above relationship that the least number of turns per phse should be employed in order to reduce the reactances effectively. However, the production of the same voltage with a reduction in the number of turns per phase requires an increase in flux, that is, an increase in stack length which leads to an increase in the leakage reactance. Thus, an optimum blaance must be established between the reactance and the generator size.

In the absence of damper windings, the commutating reactance is

$$X_C = \frac{1}{2} (X_D'' + X_Q'')$$

$$\text{where } X_D'' = X_L + \frac{1}{\frac{1}{X_{AD}} + \frac{1}{X_F}}$$

$$X_Q'' = X_L + X_{AQ}$$

Since the armature reaction reactance and the field leakage reactance are connected in parallel

$$\frac{1}{\frac{1}{X_{AD}} + \frac{1}{X_F}} \quad \text{MIN. } (X_{AD}, X_F)$$

Moreover, the armature reaction reactance is usually larger than the field leakage reactance and, consequently, the subtranseint reactance in the direct axis X_D" is usually smaller than that in the quadrature axis X_Q". Thus, in the first approximation, the commutating reactance can be calculated as

$$X_C \doteq X_L + X_{AQ}$$

The presence of the damper winding, however, adds a reactance parameter in the calculations and thus

$$X_D" = X_L + \cfrac{1}{\cfrac{1}{X_{AD}} + \cfrac{1}{X_F} + \cfrac{1}{X_{KD}}}$$

$$X_Q" = X_L + \cfrac{1}{\cfrac{1}{X_{AQ}} + \cfrac{1}{X_{KQ}}}$$

Since the damper winding leakage reactance is smaller than both the armature reaction ad field reactances, we have

$$\cfrac{1}{\cfrac{1}{X_{AD}} + \cfrac{1}{X_F} + \cfrac{1}{X_{KD}}} < X_{KD}$$

$$\cfrac{1}{\cfrac{1}{X_{AQ}} + \cfrac{1}{X_{KQ}}} < X_K$$

and it is obvious that the damper winding has a significant influence on the subtransient direct and quadrature axis reactances and, thus, on the commutating reactance. The damper winding leakage reactance depends on the number of damper bars and the cross-sectional area of the bars.

The stator leakage reactance depends on the number of poles, number of slots, slot geometry and the coil pitch. Since several combinations of poles and slots can produce a balanced winding, emphasis is placed on the slot geometry particularly the slot opening and depth since

$$X_L \propto \frac{(turns/phase)^2 \ (stack\ length)\ (slot\ depth)}{slot\ opening}$$

This implies that stator leakage reactance can be decreased if a larger slot opening and a smaller slot dept is used. However, a larger slot opening increases the rotor pole face losses. Thus, the slot geometry must be chosen with a view to achieve the best compromise between the reactance and the pole face losses.

After reviewing the factors that influence the commutating reactance, it becomes obvirus that a significantly lower reactance could be achieved by incorporating an effective amortisseur circuit in the shrink ring. After several trade-off studies were conducted to determine the appropriate slot geometry, it was determined that the introduction of three .057 in. amortisseur bars per pole would reduce the commutating inductance from 84.5 uH/phase to 47.7 uH/phase.

4.3   POLE FACE LOSSES

The pole face losses are generated due to eddy current and hysteresis. As the mgnetic flux density at the pole face is greater at the tooth than at the slot, the pole face experiences a pulsating flux density. This causes eddy currents to circulate in the pole face resulting in losses and consequently, heat generation.

To minimize pole face losses the slot opening, air gap and materials used are important factors and need to be considered in the generator design. While the pole face losses would be minimal

82

with closed stator slots and a larger air gap, the commutating
reactance would be exceedingly high. Moreover, this configuration
is not practical since the large air gap would reduce the output
and the close slots would not permit insertion of coils. However,
the pole face losses can be reduced by laminating the magnetic seg-
ment of the shrink ring. Several authors have analyzed these
losses and the following equations are used in this design

Eddy current loss

$$W_{EC} = 3.06 \; \frac{K_{PF} \cdot P \cdot A_{PF}}{R} \; \left(\frac{\phi \; GAP}{A_{PF}}\right)^{2.1} \; F_R^{1.7} \; t^{1.2}$$

Hysteresis loss

$$W_H = 0.00965 \; K_{PF} \; A_{PF} \; \left(\frac{\phi \; GAP}{A_{PF}}\right)^{1.4} \; F_R$$

where K_{PF} = pole face loss factor

P = number of poles

A_{PF} = area of pole face

R = resistivity of face material

ϕGAP = air gap flux per pole

F_R = pole face ripple frequency

t = lamination thickness

The total pole face loss is simply the sum of the eddy current loss
W_{EC} and the hysteresis loss W_H. Table 4.3 gives the pole face losses
with laminated segments and the conventional solid design. It is
evident that a reduction of approximately 40% is achieved.

SYSTEM KVA	15,300 RPM		26,250 RPM	
	LAM.	SOLID	LAM.	SOLID
40	0.57	1.0	0.58	1.0
45	0.59	1.0	0.58	1.0
60	0.60	1.0	0.60	1.0

Table 4.3. Pole Face Losses

4.4   SUMMARY OF ELECTROMAGNETIC DESIGN

The electromagnetic design based on several trade-off studies as mentioned earlier is summarized below:

Stator

number of phases	6
number of slots	60
lamination	
OD	6.05"
ID	5.09"
thickness	0.006"
slot	
opening	0.130"
depth	0.270"
turns per coil	2.5
number of wires	2.5
type of wire	No. 24 HML
height of iron	2.88"
max. commutating inductance	47.4 uH/phase

Rotor

outside diameter	5.00"
inside diameter	2.018"
air gap	0.045"
number of poles	10
per unit pole arc	0.6
shrink ring thickness	0.325"
hub thickness	0.15"
amortisseur circuit	
number of bars	3
bar diameter	0.0571"
end ring width	0.075"
end ring radial thickness	0.2"

Magnet

material	Sm-Co
energy product	21 MGOe min.
recoil permeability	1.03
reversible temp. coefficient	0.05 per °C
irreversible temp. coefficient	1% per 100°C
size:	
circumferential	0.628"
radial	1.016"
length	0.96"
total number of magnets	30

A space harmonic analysis based on this design is given in Table 4.4.

POSSIBLE HARMONICS* = 6K ± 1 FOR K = k, 2, 3, ...etc.

First slot harmonics = 11th, 13th
Second slot harmonics= 23rd, 25th

HARMONIC	K_p	K_D	K_{SKEW}	$K_p K_d K_{SKEW}$	% HARMONIC
1	0.9659	0.9698	0.9886	0.9261	100
5	0.2588	0.4131	0.7379	0.0789	1.7
7	0.2588	0.4131	0.5271	0.0564	0.87
11	0.9659	0.9698	0.0899	0.0842	0.83
13	0.9659	0.9698	0.0760	0.0712	0.59
17	0.2588	0.4131	0.2170	0.0232	0.15
19	0.2588	0.4131	0.1942	0.0208	0.12
23	0.9659	0.9698	0.0430	0.0403	0.19
25	0.9659	0.9698	0.0395	0.0370	0.16

* Assume sinusoidal air gap flux density waveform.

Table 4.4.   Harmonics Analysis

Assuming that the air gap flux density waveform is a sinusoid, the possible harmonics for a six phase machine are given by

$$n = 6K \pm 1 \quad (K = 1,2,3,\ldots)$$

The first slot harmonics are the 11th and 13th and the second slot harmonics are the 23rd and 25th.

4.5 FLUX PLOTTING USING FEA

A finite element analysis was used to determine the flux distribution within the machine. This analysis based on energy principles takes into account all the non-linearities of the magnetic circuit. The flux distribution in the two dimensional model is governed by the following non-linear differential equation.

$$\frac{\partial}{\partial x}\left(\frac{1}{\mu}\frac{\partial A}{\partial x}\right) - \frac{\partial}{\partial y}\left(\frac{1}{\mu}\frac{\partial A}{\partial y}\right) = -J$$

where μ, the permeability of the material, is a function of the unknown vector potential A and J is the current density. The energy functional F is the difference between the stored energy and the input energy and can be expressed as

$$F = \int_{v}\left(\int_{0}^{B} H\,dB - \int_{0}^{A} J\,dA\right)\,dV$$

where B is the induction and H is the coercive force. The finite element method is a variational technique and obtains solution to the field problem by minimizing the energy functional that is

$$\frac{\partial F}{\partial A} = \int_{v}\frac{\partial}{\partial A}\left(\int_{0}^{B} H\,dB - J\right)\,dV = 0$$

The essential assumptions made here are

i)   effects due to end leakage are negligible

ii) eddy currents produced by time varying field can be neglected

86
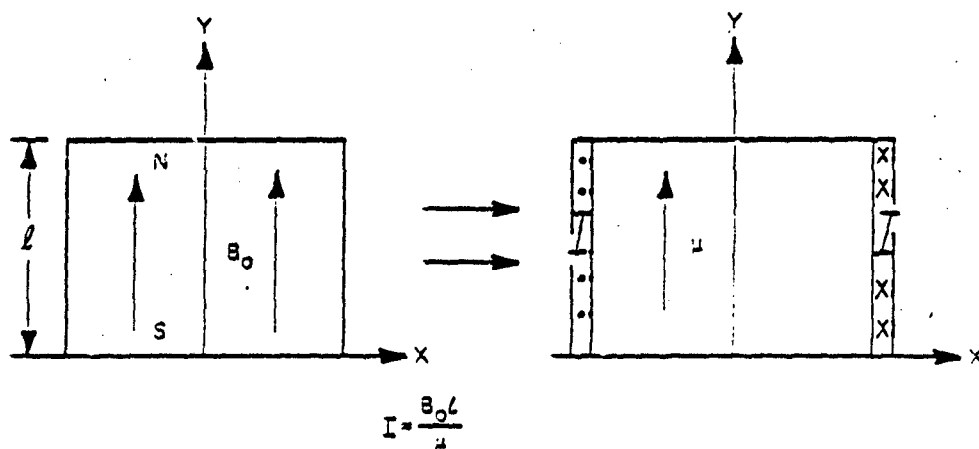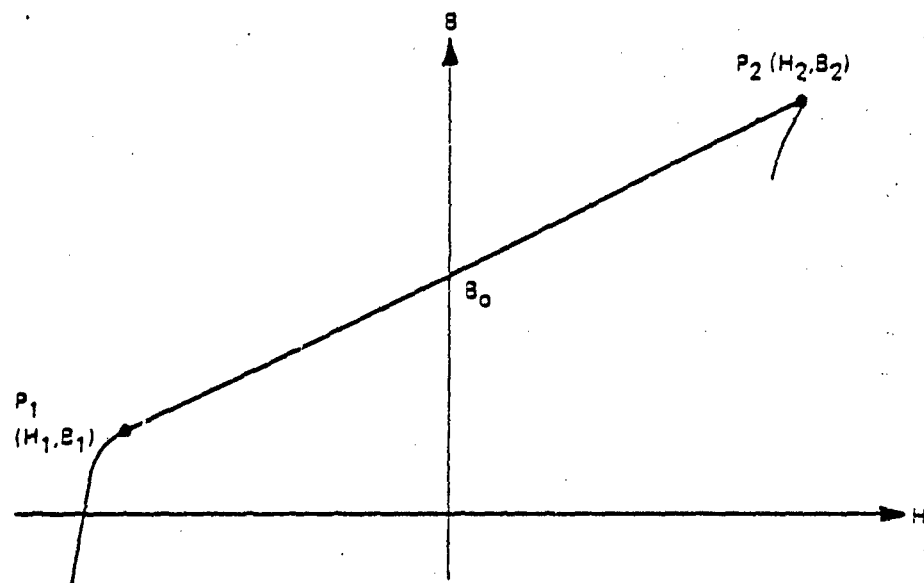
Figure 4.7 - B-H curve for a permanent magnet and the development of an equivalent model.

iii) hysteresis effects are neglected so that the magnetization curve is single valued

iv) flux leakages from the stator outer circumference can be neglected

The B-H curve for a typical permanent magnet material is shown in Figure 4.7. For the operating point lying between P_1 and P_2 we have

$$\bar{H} = (\bar{B} - \bar{B}_o)/\mu$$

where B_o is the residual induction. Amperes' law becomes

$$\nabla \times \bar{B}/\mu = J + \nabla \times \bar{B}_o/\mu$$

Thus a rectangular shaped magnet may be replaced by a material of permeability having a current density

$$J_{PM} = \nabla \times \bar{B}_o/\mu$$

Since B_o is uniform throughout the magnet, J_{PM} exists on the magnet surface and the related current is

$$I = B_o L/\mu$$

Figures 4.8 and 4.9 show the no load and load flux plots of this permanent magnet machine. The finite element grid used had 197 nodes and 346 elements. The no load flux plot is symmetric about the pole axis as expected. The load flux plot, however, is asymmetric and it is to be noted that these flux plots represent the distribution at a particular instant of time.

ELECTROMAGNETIC WEIGHTS

The electromagnetic weights are summarized as follows:

Stator:
  Core   4.23 lbs
  Copper   1.94 lbs
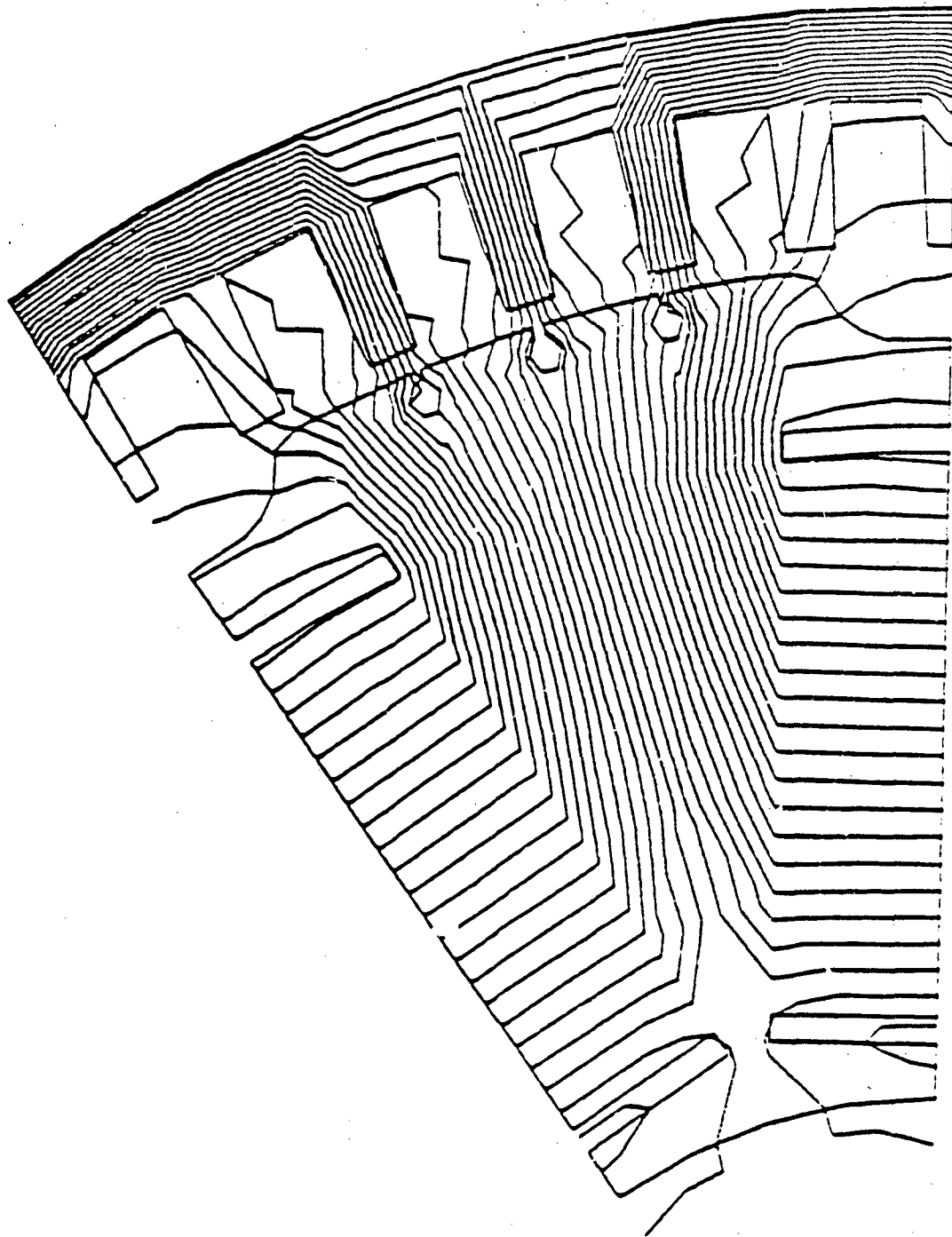
Figure 4.8 - No load flux plot.

MODEL, LOADPNG.

SUBCASE 1
INTER A VIEW COMMAND.
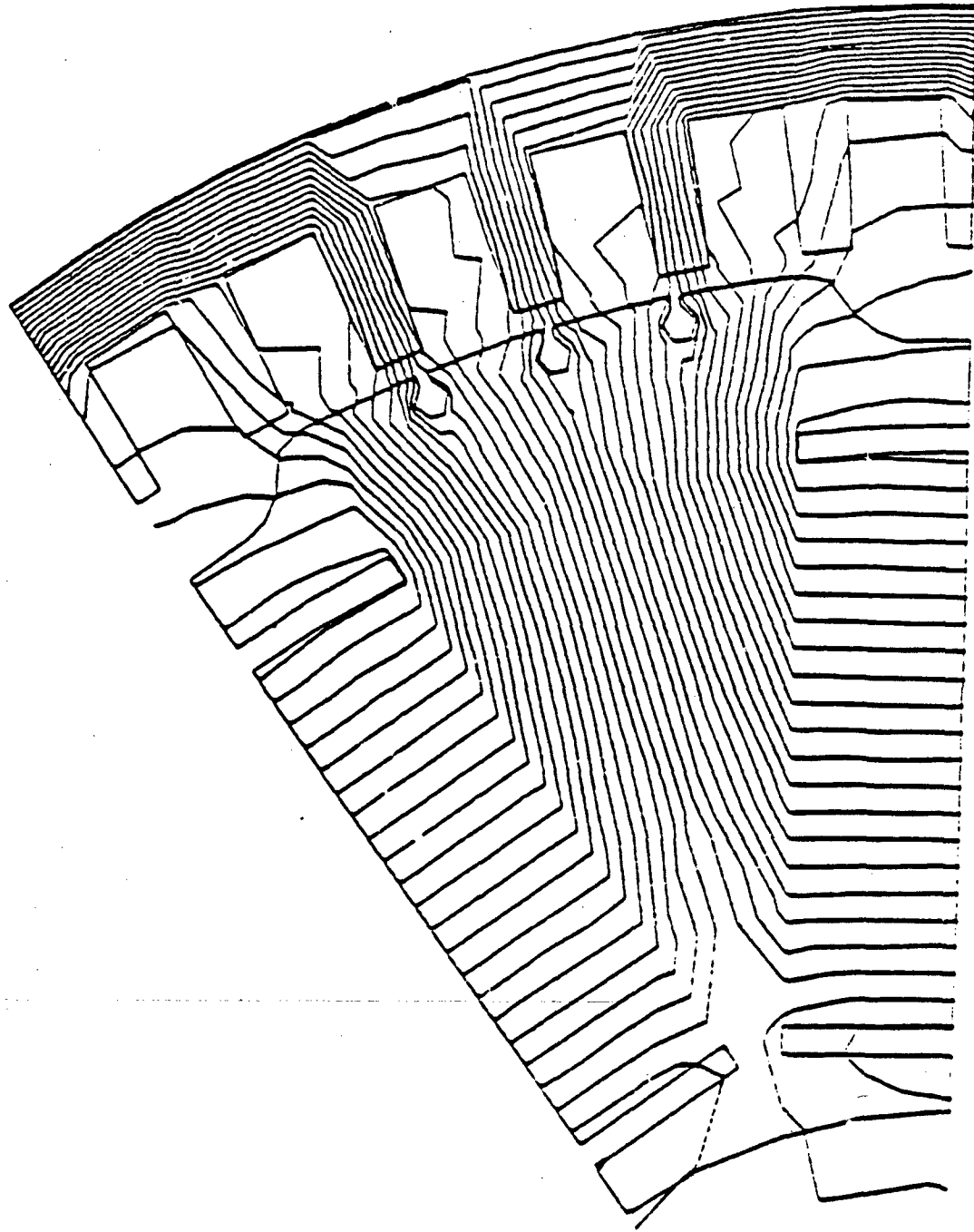
Figure 4.9 - Flux plot at 1 PU load

Rotor:

Magnet	5.44 lbs
Pole	3.47 lbs
Shrink Ring	3.77 lbs
Hub	0.83 lbs
Damper Winding	0.22 lbs

Total electromagnetic weight   19.90 lbs

SUMMARY OF ELECTROMAGNETIC LOSSES

The electromagnetic losses calculated at 250°C are tabulated for minimum and maximum speed conditions.

SYSTEM KVA @ 0.95 PF	LOSSES AT 15,300 RPM, 250°C		
	COPPER KW	CORE KW	POLE FACE KW
40	2.13	0.74	0.26
45	2.56	0.73	0.26
60	4.45	0.68	0.24

SYSTEM KVA @ 0.95 PF	LOSSES AT 26,250 RPM, 250°C		
	COPPER KW	CORE KW	POLE FACE KW
40	2.13	1.67	0.61
45	2.56	1.64	0.6
60	4.45	1.48	0.55

The copper loss at the actual operating temperature can be determined by calculating the resistance of the winding and then multiplying by the square of the armature current. The core and pole face losses are primarily influenced by speed and not significantly by temperature.

4.6   ROTOR STRESS ANALYSIS

In order to insure that the shrink ring stresses were within the permissible limit, a finite element analysis was performed. This was particularly important in view of the amortisseur holes that lead to stress concentration. Owing to the symmetry of the rotor, only a half pole pitch was modelled. The two dimensional grid is
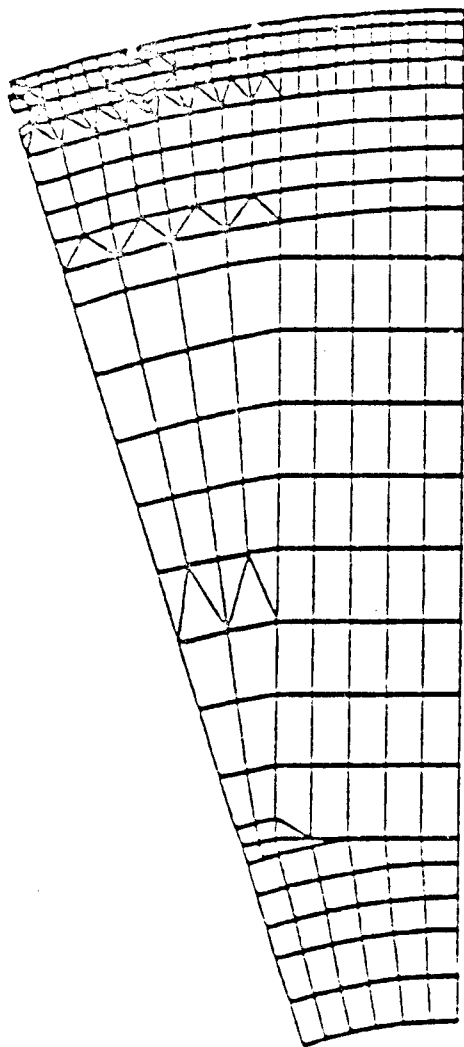
Figure 4.10 — Grid Generated for the Rotor Segment
Using 2D Isoparametric Solid Elements

TYPE OF ELEMENT — STIF42
NO. OF ELEMENTS — 191
NO. OF NODES — 355

1 — SHAFT & HUB
2 — MAGNETS
3 — POLE
4 — NON-MAGNETIC SECTION
5 — MAGNETIC SECTION

CONTAINMENT RING
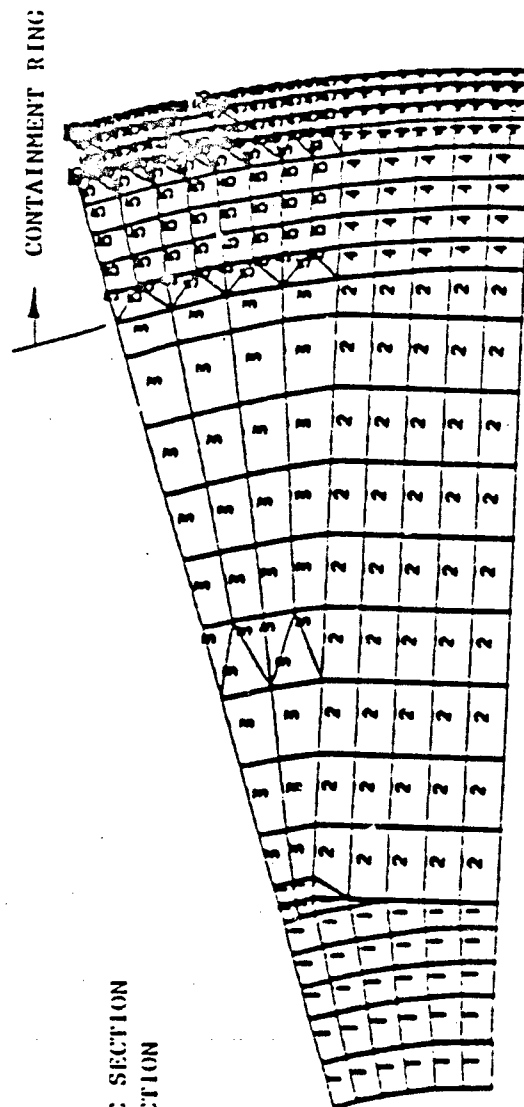
Figure 4.11 — Grid Specifying Material Types Used

SIGE STRESS
118,000 PSI

MAX. SIGE
123,403 PSI
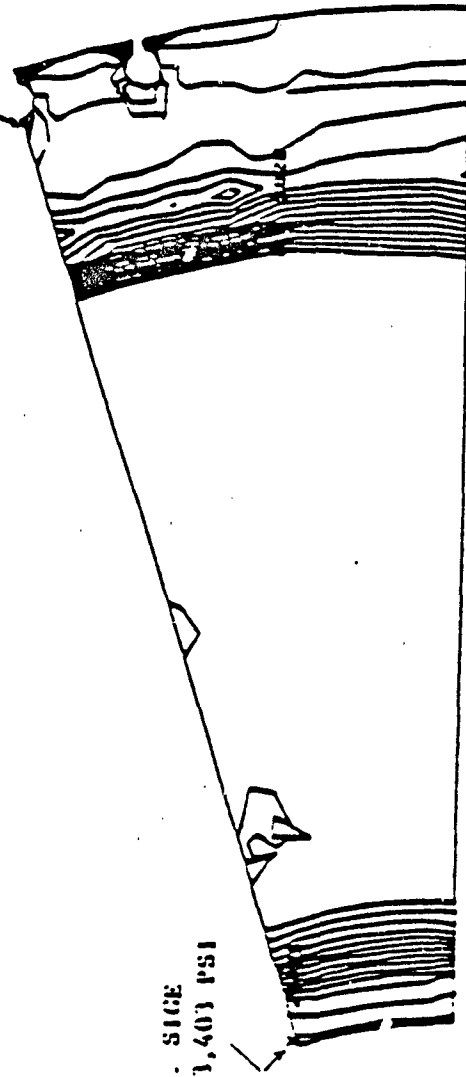
Figure 4. 12 - Stress Contour Plot at 0 RPM

93

DASHED LINES INDICATE INITIAL CONDITION
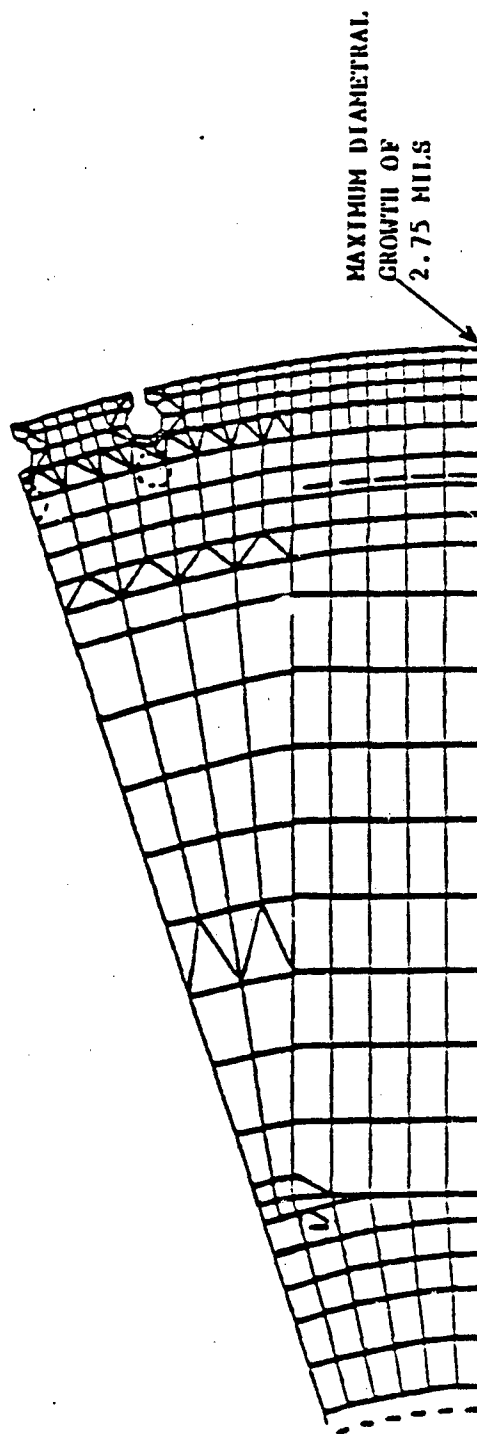
MAXIMUM DIAMETRAL
GROWTH OF
2.75 MILS

4.13 - Displacement Plot at Overspeed (28,875 RPM)

MAX. SIGE – 133,501 PSI
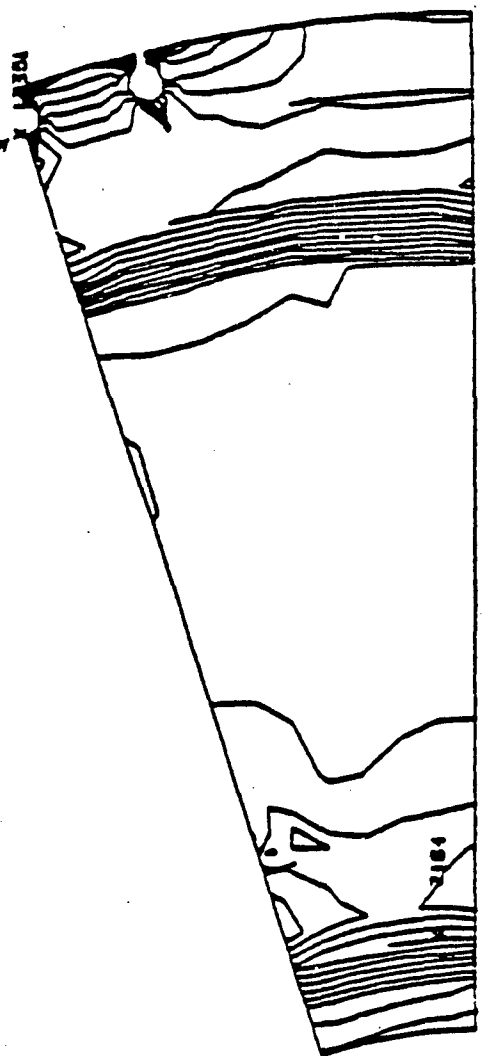
Figure 4.14 - Significant Stress Contour Plot at Overspeed

MAX.S.I.– 144,404 PSI
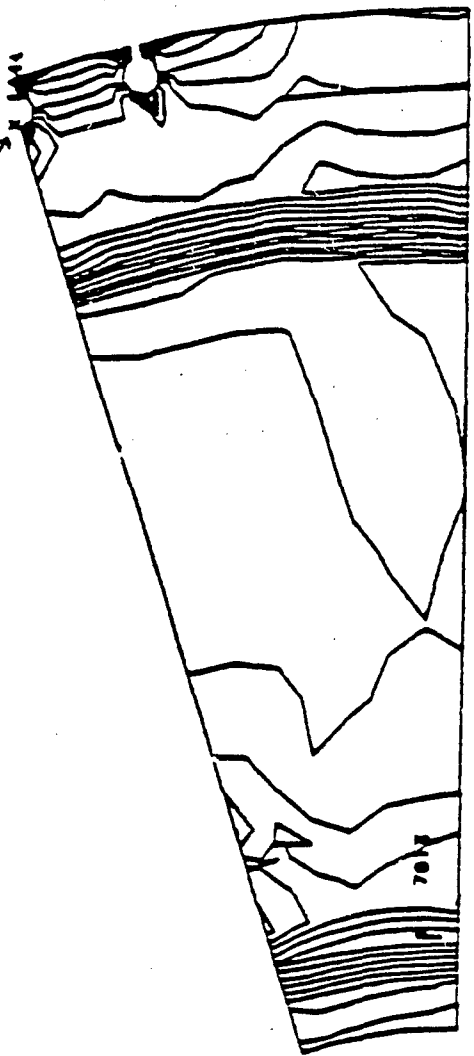
Figure 4.15 - Stress Intensity Contour Plot at Overspeed

95

shown in Figure 4.10 and is comprised of 191 elements formed with
355 nodes. Since ANSYS has the capability of realizing dis-
continuitie. in the structure, it was possible to include the re-
lief at the bottom of the magnet and the amortisseur holes. Six
different material properties were specified as shown in Figure 4.
and 4 noded isoparametric elements were used.

Figure 4.12 shows the stress contours in the rotor at stand-
still. The stresses are induced mainly due to the interference
between the shrink ring and the hub pole magnet assembly. The maxi-
mum significant stress occurs around the amortisseur hole and is
defined as

$$\sigma_{sig} = \frac{1}{\sqrt{2}} \sqrt{(\sigma - \sigma_2)^2 - (\sigma - \sigma_3)^2 - \sigma - \sigma_3}$$

where σ, σ and σ_3 are the principal stresses. Figure 4.13 is the
displacement plot of the rotor at overspeed, that is 28,875 rpm. Due
to the direct loading of the magnets on the containment ring, the
highest growth is in the non-magnetic segment. The dashed lines in
this post processor plot represents the original configuration. The
displacements are exaggerated with the maximum movement scaled to
approximately ½" on a 10" x 10" plot.

Figure 4.14 is a significant stress plot at overspeed where
the stress concentration around the amortisseur hole is evident.
Figure 4.15 is a stress intensity plot and portrays a similar distri-
bution. Stress intensity, which is the maximum difference between
principal stresses, is used for comparison with the yield strength
according to the shear stress theory of failure.

The results of this analysis confirmed that the stresses were
within the permissible limit. Moreover, the areas of the highest
stress levels were removed from the fusion zones.

4.7 BEARING ANALYSIS

The two bearings used in the machine were the MM9107 type hav-
ing an ABEC-7 precision. The dimensions of this bearing are as
follows:

bore	1.378"
OD	2.4409"
width	0.5512"

Using an operating temperature of about 95°C and MIL-L-7808 oil for
lubrication, the bearing life was calculated using a
program developed by General Electric's Aircraft Engine Group.
For a thrust load of 50 lbs. and the appropriate radial load based
on mechanical and magnetic unbalances, the following life was cal-
culated:

Speed	Bearing Life
15,300 rpm	2.54×10^5 hrs.
26,250 rpm	1.23×10^5 hrs.

As evident, this bearing has a substantial life for this application.

4.8 SHAFT CRITICAL SPEED

A computer program developed in-house for determining critical
speed for two bearing rotors with and without overhangs was used.
This program, based on the transfer matrix approach, takes into
account the magnitude and location of the applied loads, the bearing
stiffnesses and varying shaft geometry. Figure 4.16 is a drawing of
the shaft and Figure 4.17 shows the position of the rotors discs as
mounted. The shaft was divided into 20 sections with the bearings
located at the midst of the 2nd and the 16th section. The static
bearing reactions were calculated as follows:

left bearing	8.67 lbs.
right bearing	9.50 lbs.

97

Figure 4.16 - Shaft

Figure 4.17 – Rotor construction.

The critical speed was determined for various bearing stiffness and are tabulated below:

BEARING STIFFNESS LBS/IN	FIRST CRITICAL SPEED RPM
250,000	30,454
333,000	34,937
400,000	38,093
555,500	44,336

The experiences with prior generators have demonstrated that the bearing stiffness is in the vicinity of 600,000 lbs/in. The lower stiffness runs were made to estimate the possible reduction in critical speed because of bearing support flexibility.

Since the overspeed for this generator is 28,875 rpm, it was apparent that no critical speed problem would be encountered in the operating speed range. This was later confirmed through extensive rotor spin test.

4.9 GENERATOR OIL FLOW

Oil is used primarily for heat removal, but also for the lubrication of bearings and splines. The oil system, which is a series-parallel circuit through the stator and rotor assemblies, is compatible with either MIL-L-23699 or MIL-L-7808 synthetic oils. The total oil is introduced to the generator through a port in the test frame and directed into the stator circuit. At exit from the stator, part of the oil enters the rotor circuit and the remaining is bypassed by means of an orifice. The complete oil schematic is shown in Figure 4.18.

The stator oil circuit is comprised of the stator frame which creates the oil interface between the stator frame and the generator test frame. The stator frame, shown in Figure 4.19, is an aluminum tube with axial passages for the oil flow. The manifolds at each end
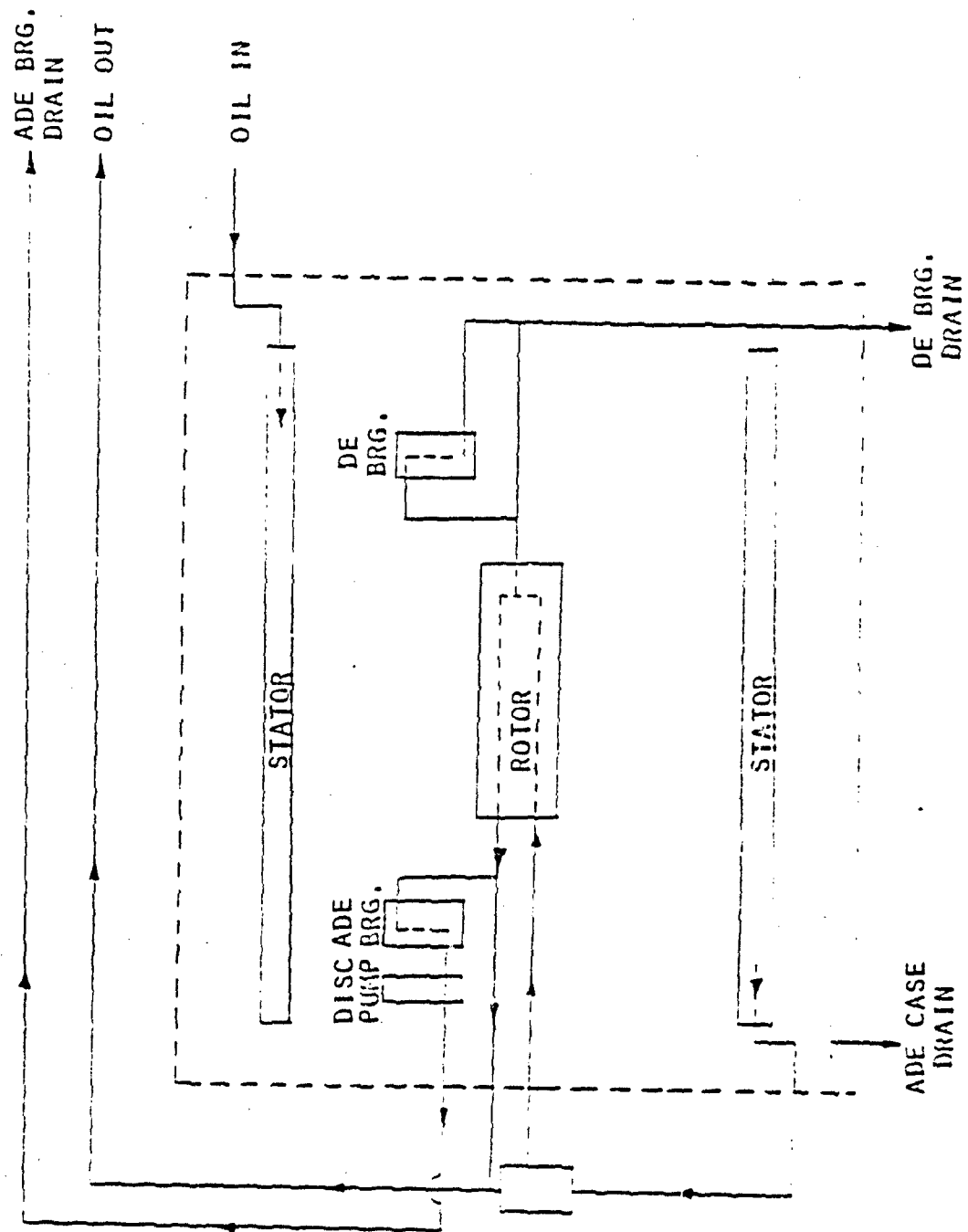
Figure 4.18 - Generator oil flow schematic.

INLET MANIFOLD

6.50 -.02

10.38 NOM.

9 SECTIONS

112 SLOTS OFFSET BETWEEN SECTIONS
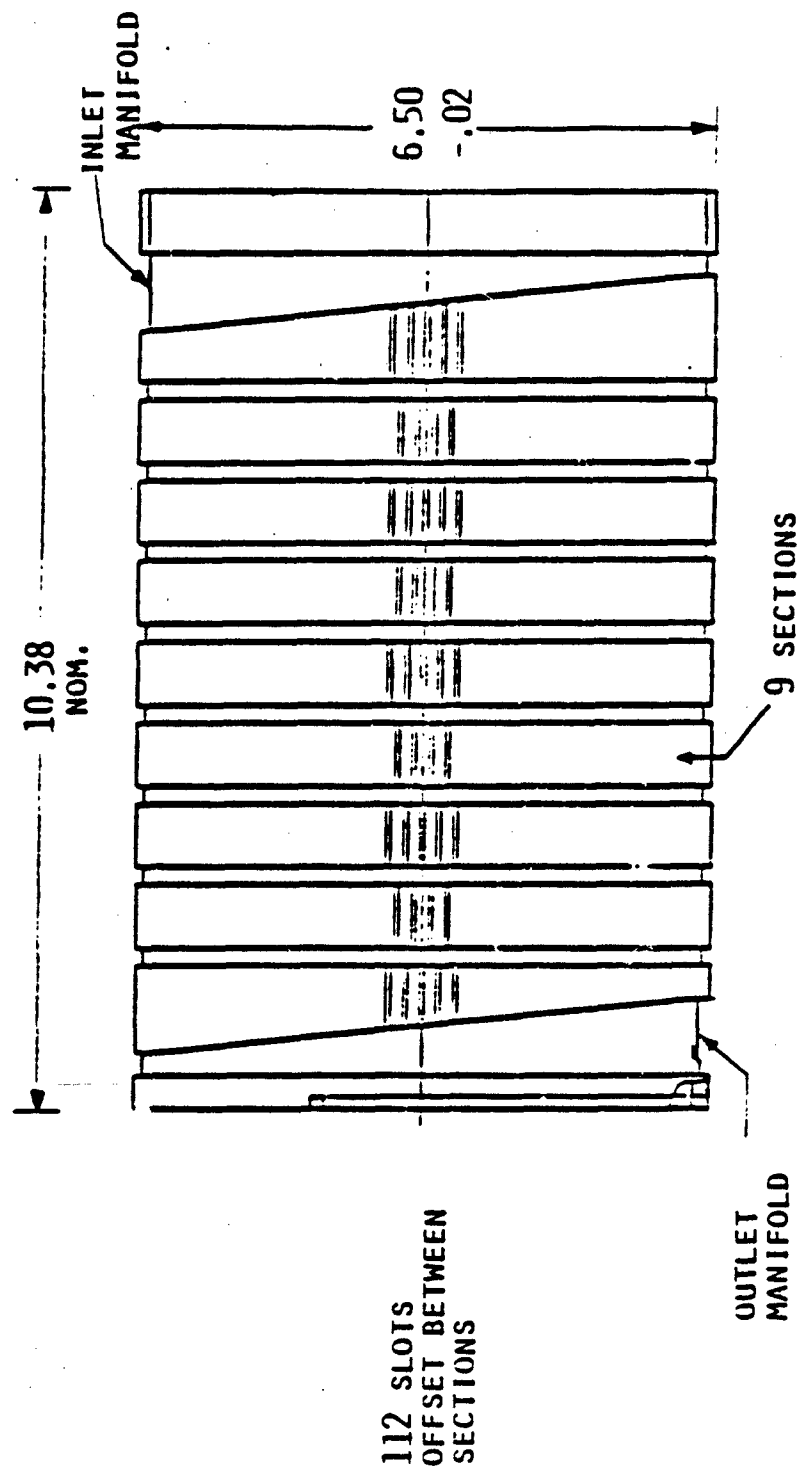
OUTLET MANIFOLD

Figure 4.19 - Stator frame showing the staggered oil grooves

are tapered for proper distribution of oil at inlet and outlet.
O-ring seals provided at the outboard end of the manifolds prevent
oil leakage. Oil, supplied at the top of the inlet manifold, flows
axially along the 112 slots which are offset between sections to
reach the outlet manifold at the anti-drive end. The staggering
of the slots generates turbulence in the oil thus enhancing the
convective coefficient and improving heat transfer. By locating
the manifolds 180° apart from one another, the oil paths are essentia-
lly the same length and thus an even oil distribution is attained.

A part of the oil exiting from the stator is bypassed by the
control valve and returned to the oil supply. The remaining oil is
directed into the rotor through a stationary transfer tube accurately
positioned inside a close clearance diameter inside the shaft. A
transfer seal at this point prevents any oil leakage. The oil flows
through the center of the shaft and is directed into the rotor passages
by the centrifugal force. At entry to the rotor passages, some oil
is used to lubricate the internal generator spline and the drive-end
bearing. The remaining oil flows outward removing heat and is dis-
charged through an outer channel into the transfer tube. A second
transfer seal at exit from the rotor limits the oil leakage into the
anti-drive end bearing cavity.

At each end of the shaft, orifices are provided to remove oil
from the shaft for bearing lubrication and seal cooling. The oil
after injection in the bearing cavities is collected at the bottom and
returned to the supply be means of drains provided at either end. The
anti-drive end bearing utilizes a disc pump to scavenge the oil back
to the supply.

The internal spline is lubricated continuously by oil taken
directly from the center of the shaft. This oil is collected in the
interface cavity between the generator and the drive and scavenged

103

from the bottom. In addition, case drains are provided at either end to remove any oil that may have leaked past the seals.

The cooling oil used in this design was MIL-L-7808 oil with a maximum inlet temperature of 80°C and the following flow rates:

SPEED RPM	STATOR FLOW GPM	ROTOR FLOW GPM
15,300	1.5	5.0
26,250	2.5	8.5

The stator oil passages were designed as being almost rectangular with dimensions of 0.125" by 0.06". The 112 slots were staggered after each section of approximately 0.72" significant length. The rotor passage was an annulus of about .025" radial gap. Occassional bumps were provided in this annulus for creating turbulence.

This oil circuit design was selected based on a trade off study between the heat transfer capability and the system pressure drop.

4.10 THERMAL ANALYSIS

A finite difference nodal approach was used to determine the temperature distribution in the machine at various speed and load conditions. Owing to the symmetry of the rotor, only a half pole pitch was modelled. The location of the nodes is given in Figure 4.20 and the corresponding thermal network is shown in Figure 4.21.

The computer program developed in-house takes into account the various thermal links, heat generators rates, boundary conditions and oil temperature and calculates the temperature at the node locations. Although the heat generation rates are inputted, the copper loss is adjusted every iteration based on the resistance of the windings. Thus, when convergence is attained, there is an exact correlation between the winding temperature and the copper losses. The other losses in the generator do not vary as significantly with

104
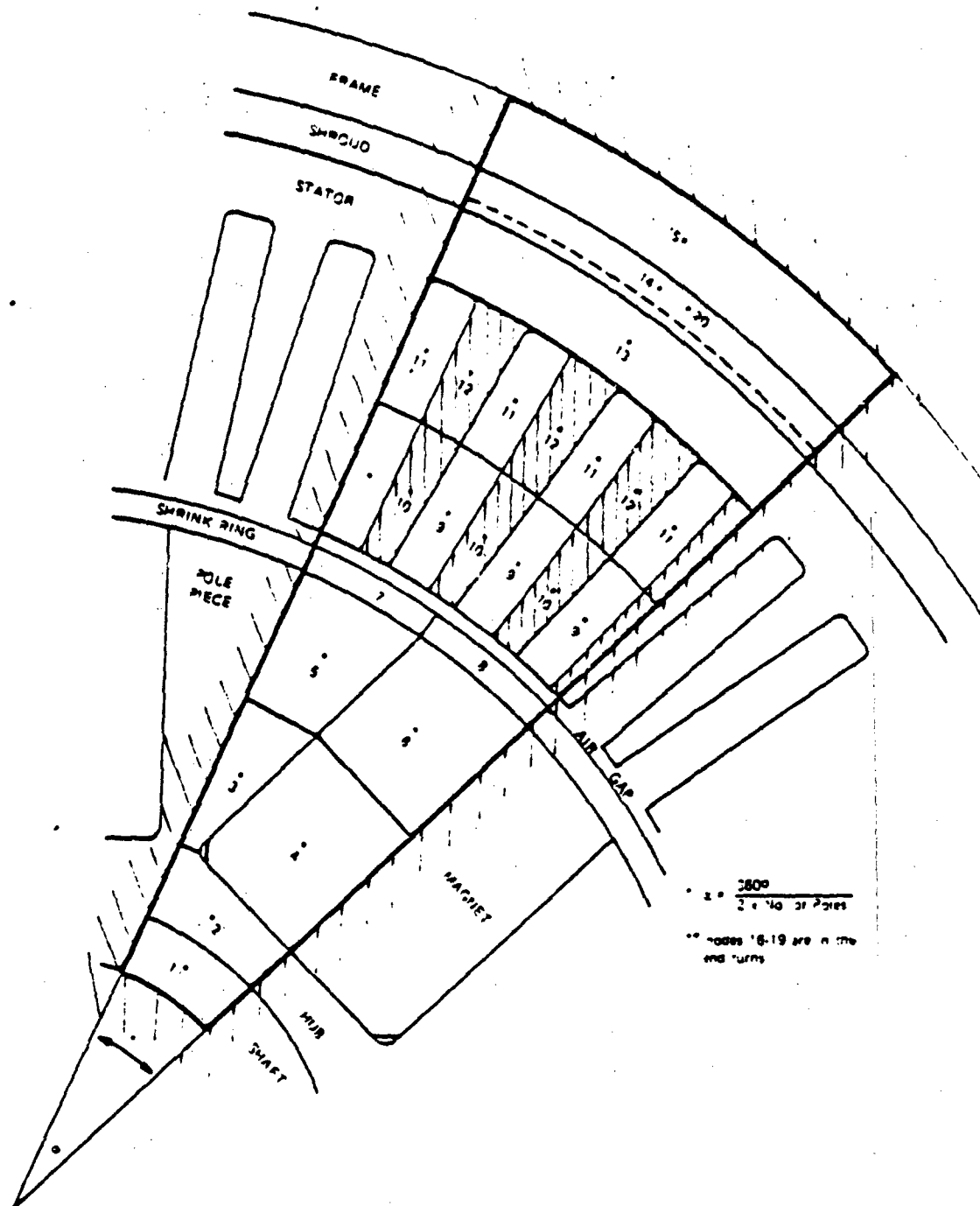
Figure 4.20 - Mathematical model of the permanent
magnet generator for thermal analysis.
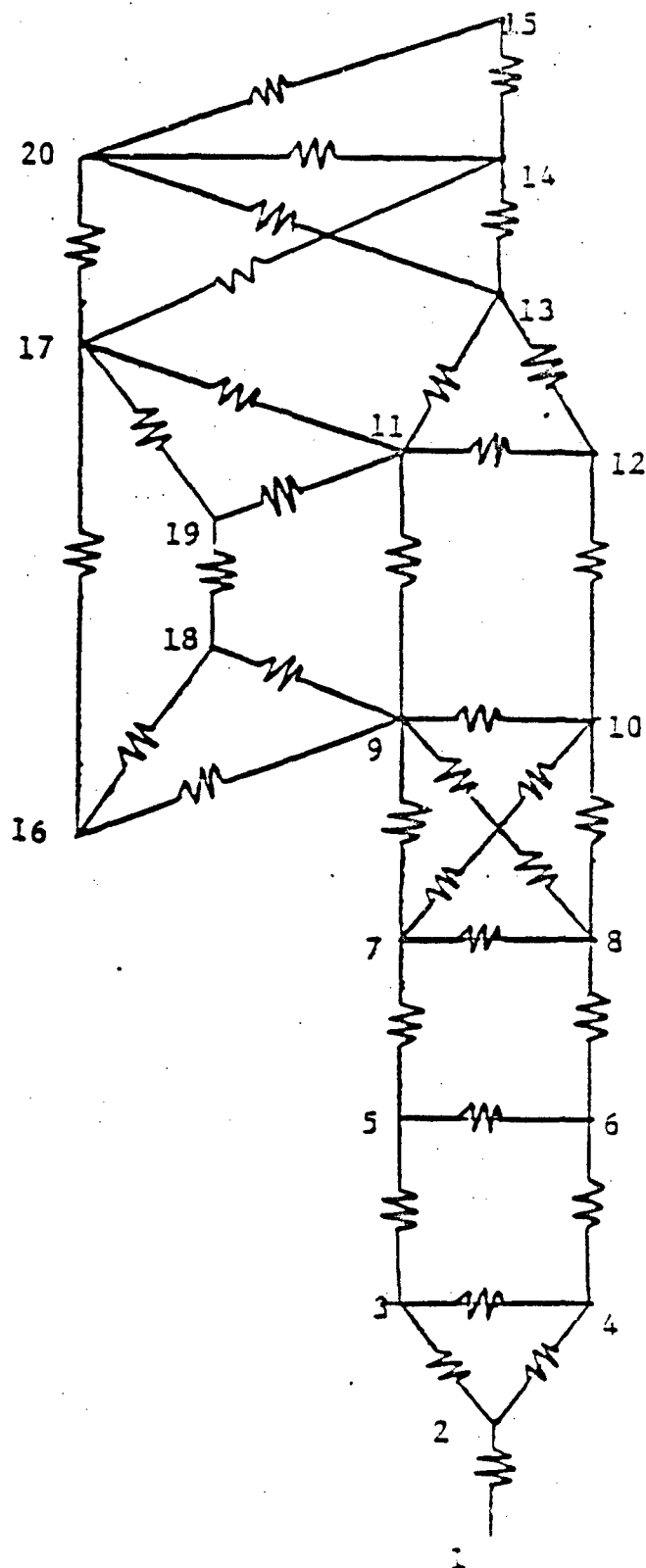
1. SHAFT
2. HUB
3. LOWER POLE PIECE
4. LOWER MAGNET
5. UPPER POLE PIECE
6. UPPER MAGNET
7. CTX SHRINK RING PORTION
8. INCONEL SHRINK RING PORTION
9. TOP SLOT
10. TOP TOOTH
11. BOTTOM SLOT
12. BOTTOM TOOTH
13. YOKE
14. SHROUD
15. FRAME
16. TOP END TURN
17. BOTTOM END TURN
18. MIDDLE END TURN
19. MIDDLE END TURN
20. OIL

Figure 4.21 - Thermal grid and node descriptions

changes in the operating temperature of the machine.

Some of the steady state results at various system loads and speeds are summarized in Table 4.5. For the overloads a transient program was used which was based on the explicit approach. A time step of 0.1 sec. was found to be suitable for rapdi convergence and stability of the solution. The time variation of temperature for the 1.5 PU condition is plotted in Figure 4.22. Because of the small time constant, almost steady condition is reached at the end of the 5 minutes overload duration.

As evident from the results, the temperatures are below the allowable limit of 250°C for the magnet and 275°C for the stator hot spot. Thus the life of the insulation materials at these lower temperature levels, which determines the life of the generator, would exceed the requirements of aircraft machines.

DATA PT.	SPEED RPM	GEN. KVA	PF	GEN. AMP/∅	ROTOR TEMP.	STATOR TEMP. °C				TOTAL LOSSES
						SLOT	TOOTH	YOKE	END-TURN	
1	15,300	45.6	0.76	40	122.4	121.9	106	91.7	123.7	2.79
2	15,300	52.2	0.74	47	129.9	135.2	112.2	94.2	138.4	3.14
3	15,300	61.1	0.76	57	133.5	152.8	117.7	95.6	159.3	3.52
4	26,250	87.4	0.74	47	155.4	171.9	135.3	104.7	182.4	5.20
5	26,250	102.6	0.76	57	162.7	181.4	146.2	109.2	191.7	5.62

Table 4.5. Steady State Temperture with 80°C Oil Inlet Temperature
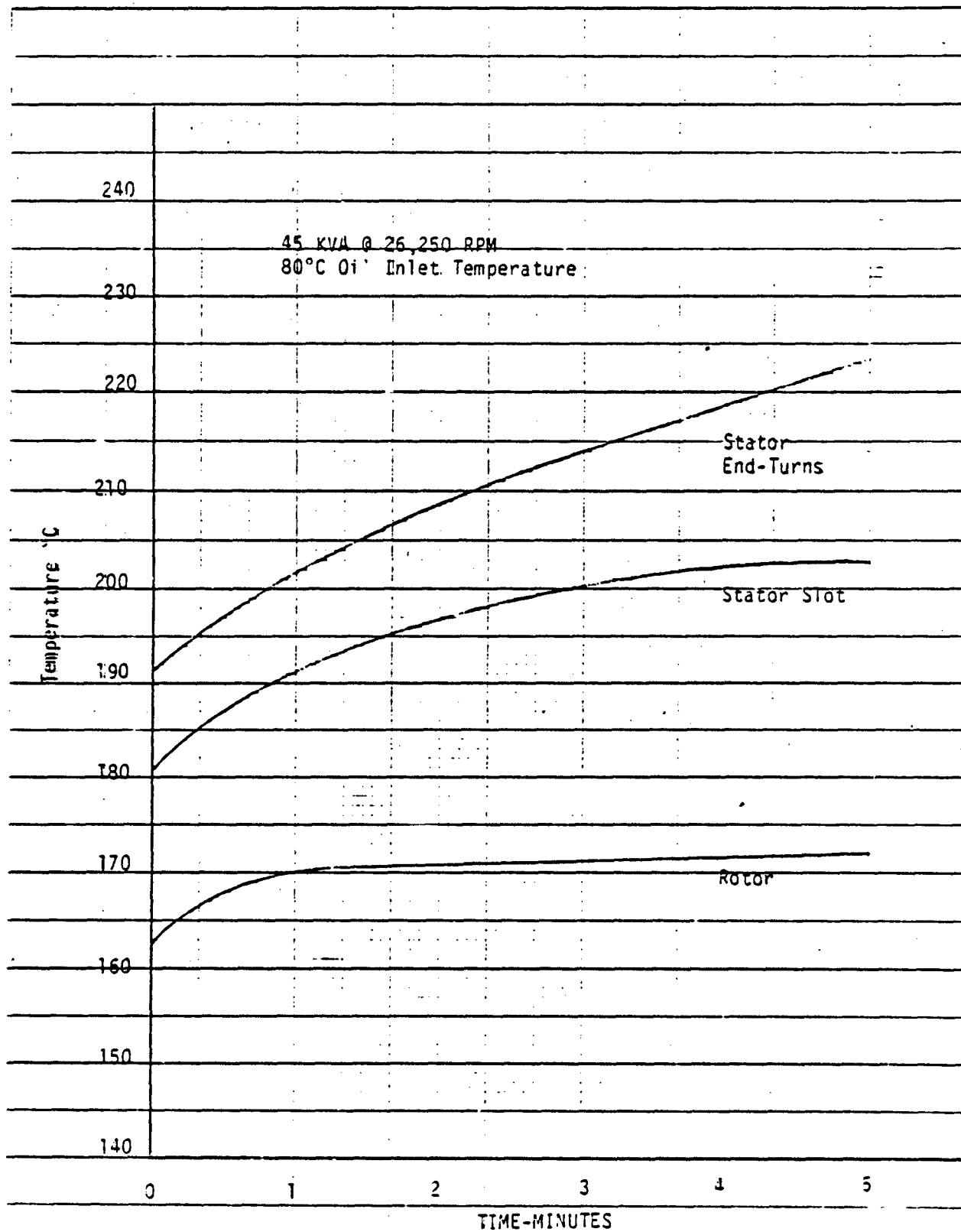
Figure 4.22 - Temp. profile for 1.5 PU
transient condition.

109

SECTION V
GENERATOR FABRICATION AND TESTING

5.1 INTRODUCTION

The fabrication of the generator was accomplished in two consecutive phases of the program. During phase II, only the rotor components were manufactured and assembled inside a specially designed test fixture An extensive 50 hour test was then conducted to verify the mechanical integrity of the containment structure. Upon successful completion of this test, phase III of the program was initiated during which the stator was fabricated and the generator assembly was accomplished. The generator was then evaluated under various speed and load conditions and its performance compared with predictions. The remainder of this section is devoted to the details of the rotor and stator construction, test procedures and test results.

5.2 ROTOR FABRICATION

A cross-sectional view of the rotor is shown in Figure 5.1. The material and construction of each component of the rotor is described below:

o Shaft - The generator shaft shown in detail in Figure 5.2 is made from Inconel-750, a non-magnetic and heat treatable material that has a yield strength in excess of 175,000 psi. The shaft is comprised of two pieces, fitted one inside the other, welded together. The inner tube is hollow and provides a channel for the flow of oil. The oil flows axially along this tube and is thrown into the annulus between the inner and outer tube due to rotation. The oil flows outward in this annulus cooling the rotor and exits via the transfer tube. At the drive end there are nozzles for the purpose of providing oil for bearing and spline lubrication.

PERMANENT MAGNET
MAGNETIZATION DIRECTION

NON-MAGNETIC
MEMBER

BIMETALLIC
SHRINK
RING

PERMANENT
MAGNET

MAGNETIC
MEMBER

HUB
(NON-MAGNETIC)

MAGNETIC
MEMBER
(POLE PIECE)

SHAFT

Figure 5.1 - Cross-sectional view of the permanent magnet rotor

Figure 5.2 - Shaft

112

o Hub - The hub is made from Inconel-750 to minimize flux leakage.
   It provides the base for attachment of the spoke configured
   poles as shown in Figure 5.3. The poles are tapered to provide
   a rectangular slot for the magnets.

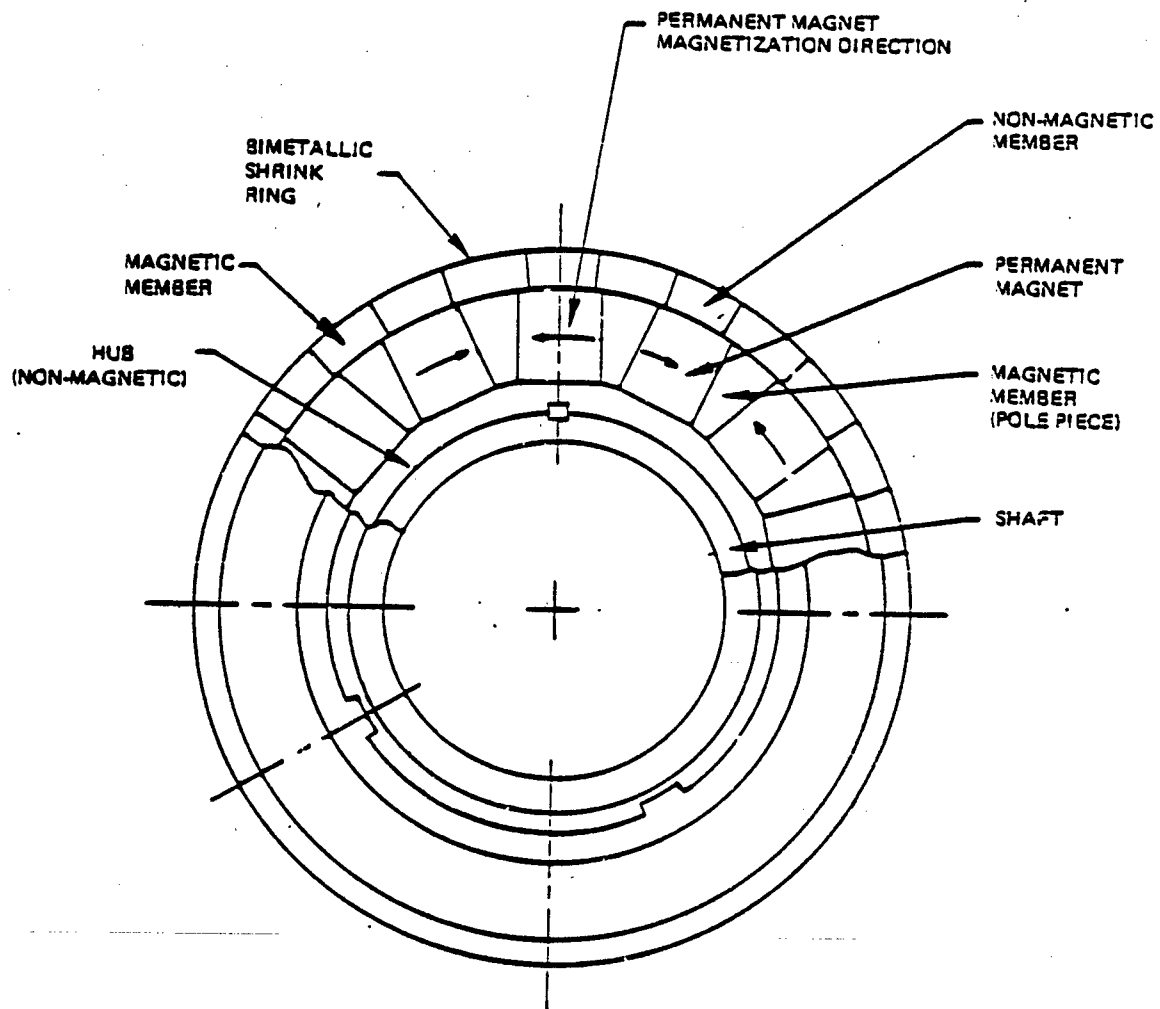o Magnets - The magnets are produced from fine particle rare-
   earth samarium cobalt alloy which is sintered, heat treated and
   circumferentially aligned to provide an energy product of not
   less than 21 X 10^6 gauss oersted measured at room temperature.
   The magnets are assembled in the hub-pole assembly in the fully
   magnetized state.

o Shrink ring - The shrink ring is bimetallic with alternate seg-
   ments of Inconel-750 and Carpenter Steel CTX-1. The ring is
   heat treated to attain the required electromagnetic and mechani-
   cal properties. This ring is assembled over the pole-magnet
   assembly with an interference fit to provide the preload and
   minimize stress cycling.

o Rotor assembly - Three discs are assembled on the shaft with an
   interference fit with care taken to insure alingment of the
   amortisseur holes. The amortisseur bars are brazed at either end
   to a copper ring for short circuiting. The copper ring, in turn,
   is contained inside the Inconel ring that serves as a side cover
   for the magnets. The containment of the upper ring is important
   because copper has the tendency to creep at high temperatures.
   The complete rotor is shown in Figure 5.4.

o Seals - Two spring loaded circumferential carbon seals are used
   at either end to prevent leakage of the bearing oil. The seal
   bore diameter operates on a chrome plated surface of 1.56"
   diameter having a 8 micro inch finish. The seal is supported at
   the outside by the bearing bracket. As the shaft rotates, the
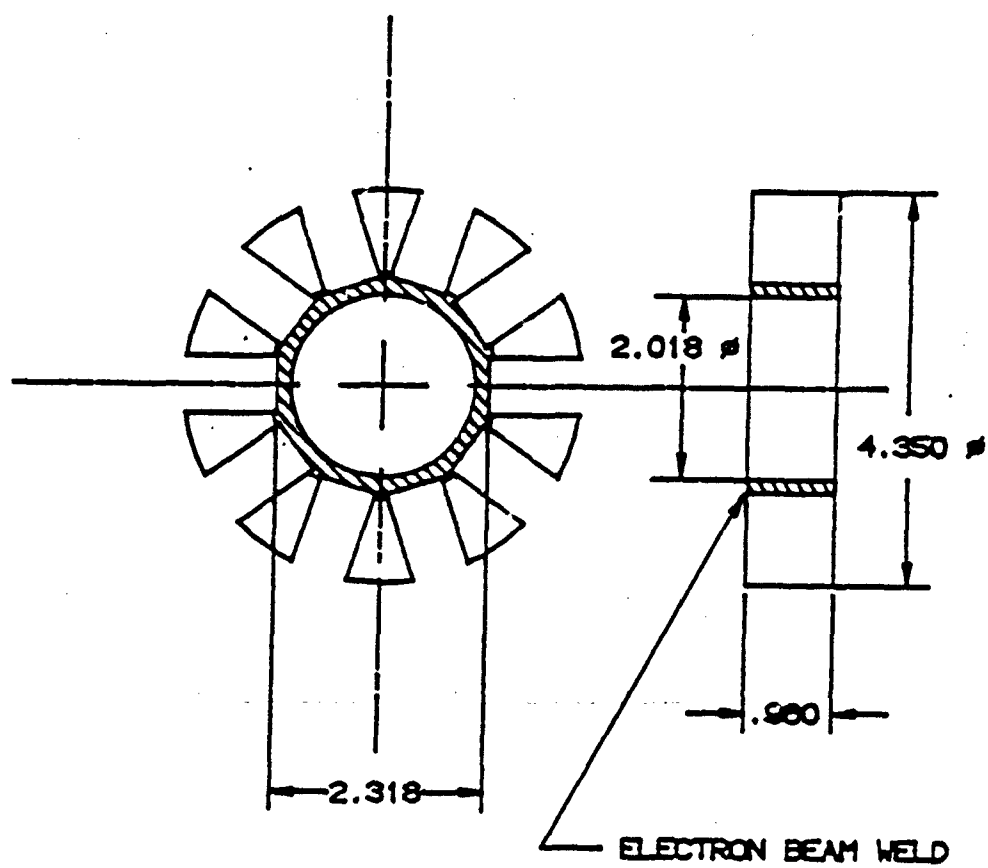   carbon face rides on a thin layer of oil and thus provides the
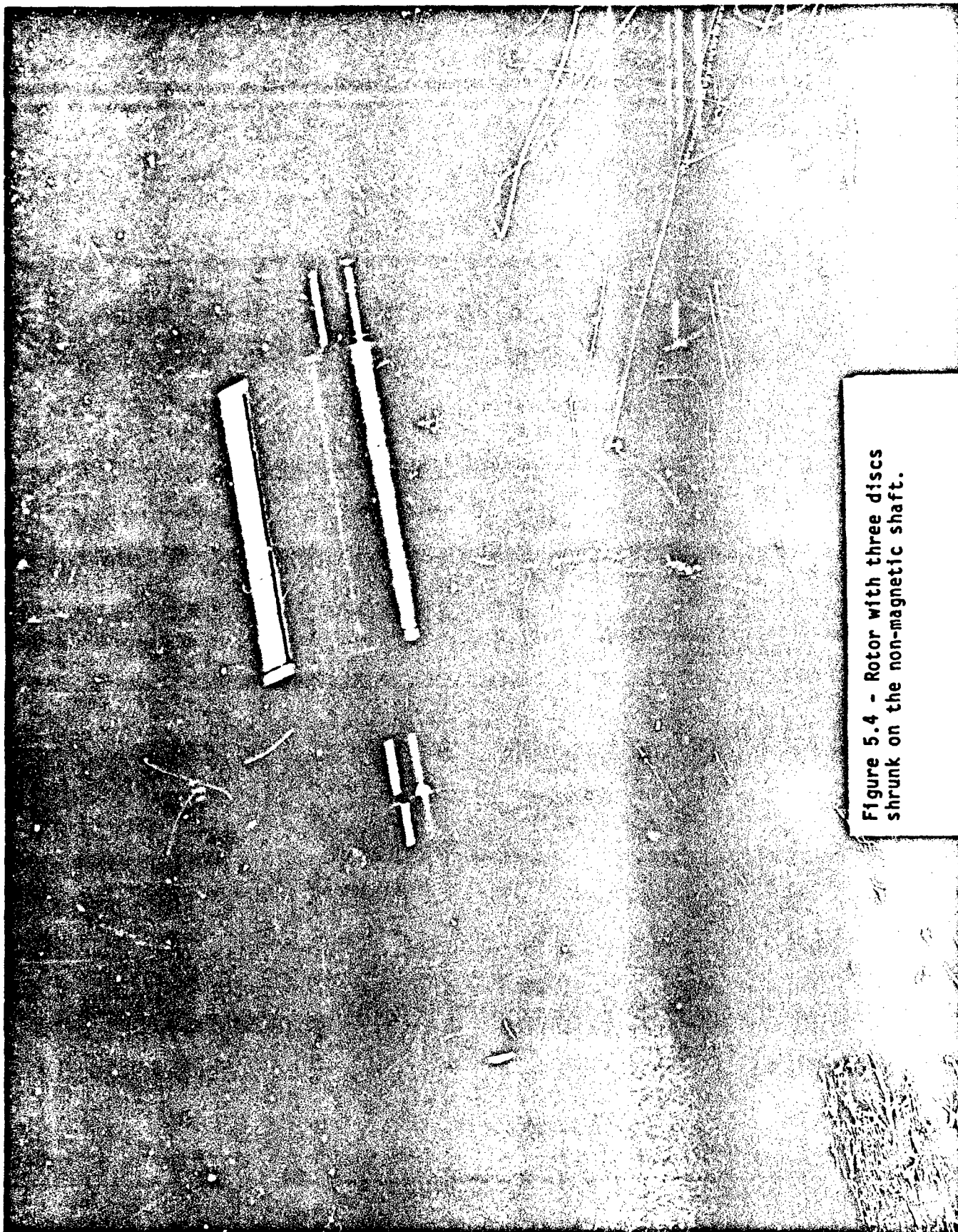   necessary sealing.

Figure 5.3 - Hub and pole.

Figure 5.4 - Rotor with three discs shrunk on the non-magnetic shaft.

o Bearings - Two MM9107 bearings having an ABEC-7 precision are used.
   The races and balls are made from AISI M-50 steel for enhanced
   B10 life. These bearings are assembled on the rotor with a
   slight interference and operated with an axial preload of 50 lbs
   supplied by means of wavy springs. The outer race of the bearings
   is housed in a steel sleeve which fits in the aluminum housing.
   Cooling and lubrication is provided by jetting oil from a nozzle
   located in the shaft.

o End bells - The end bells which serve as housing for the rotor .
   bearings are machined from aluminum bar stock. They are designed
   to have a high stiffness, at minimum weight, in order to insure a
   smooth rotor operation. With o-ring seals placed between the end
   bells and the stator frame, a dry rotor cavity is maintained. The
   anti-drive end bell has an opening for exit of the stator leads.

5.3 ROTOR TESTING

At the conclusion of the rotor fabrication, a test was conducted
to evaluate the dynamic performance of the rotor over its entire speed
range. For the purposes of this test, the rotor was assembled inside
a spin test fixture as shown in Figure 5.5. The fixture was simply
a stator frame, complete with oil grooves at the outside, having a
partially machined and hence a smaller inside diameter. This test
assembly was then fitted inside a test frame which had the mounting pad
and the required oil inlet and outlet parts.

Two thermocouples were placed in the rotor cavity to record
the operating air gap temperature. The test frame was mounted on a
125 hp drive stand and the oil lines were installed. Provisions were
made to monitor rotor and stator oil flow independently as well as
oil temperatures and pressures. Furthermore, an accelerometer was
mounted at the anti-drive end to record vibration levels. The labor-
atory set up is shown in Figure 5.6.
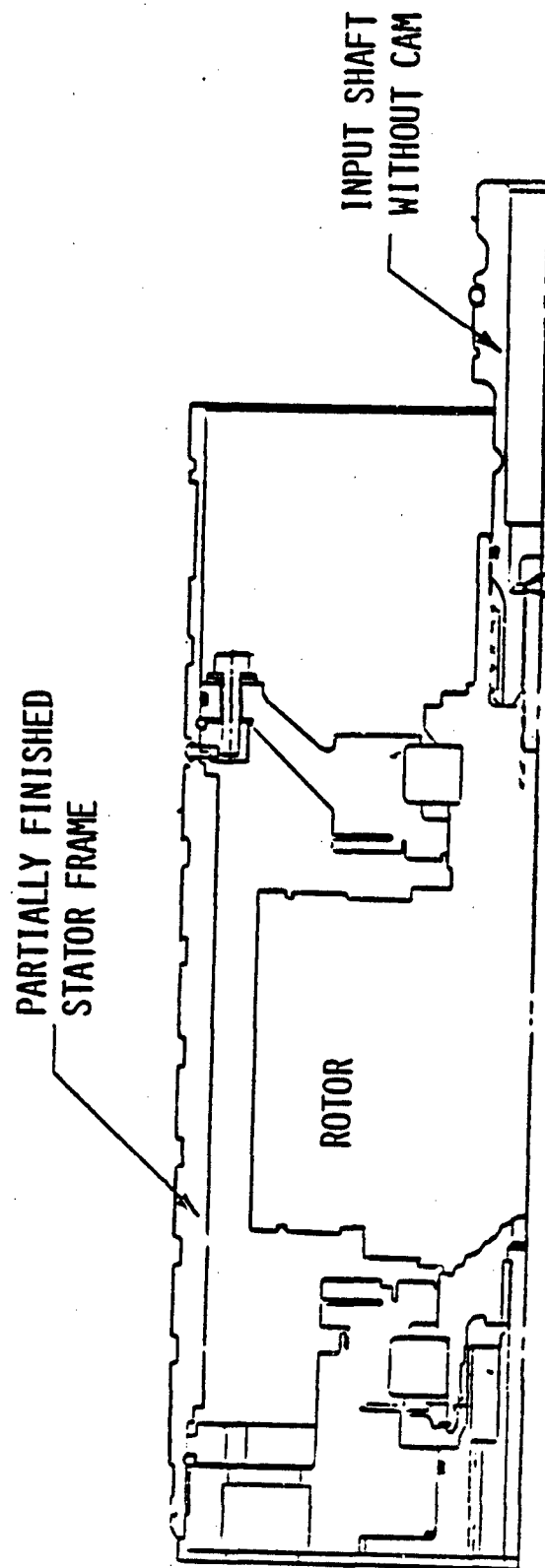
116

INPUT SHAFT WITHOUT CAM

PARTIALLY FINISHED STATOR FRAME

ROTOR

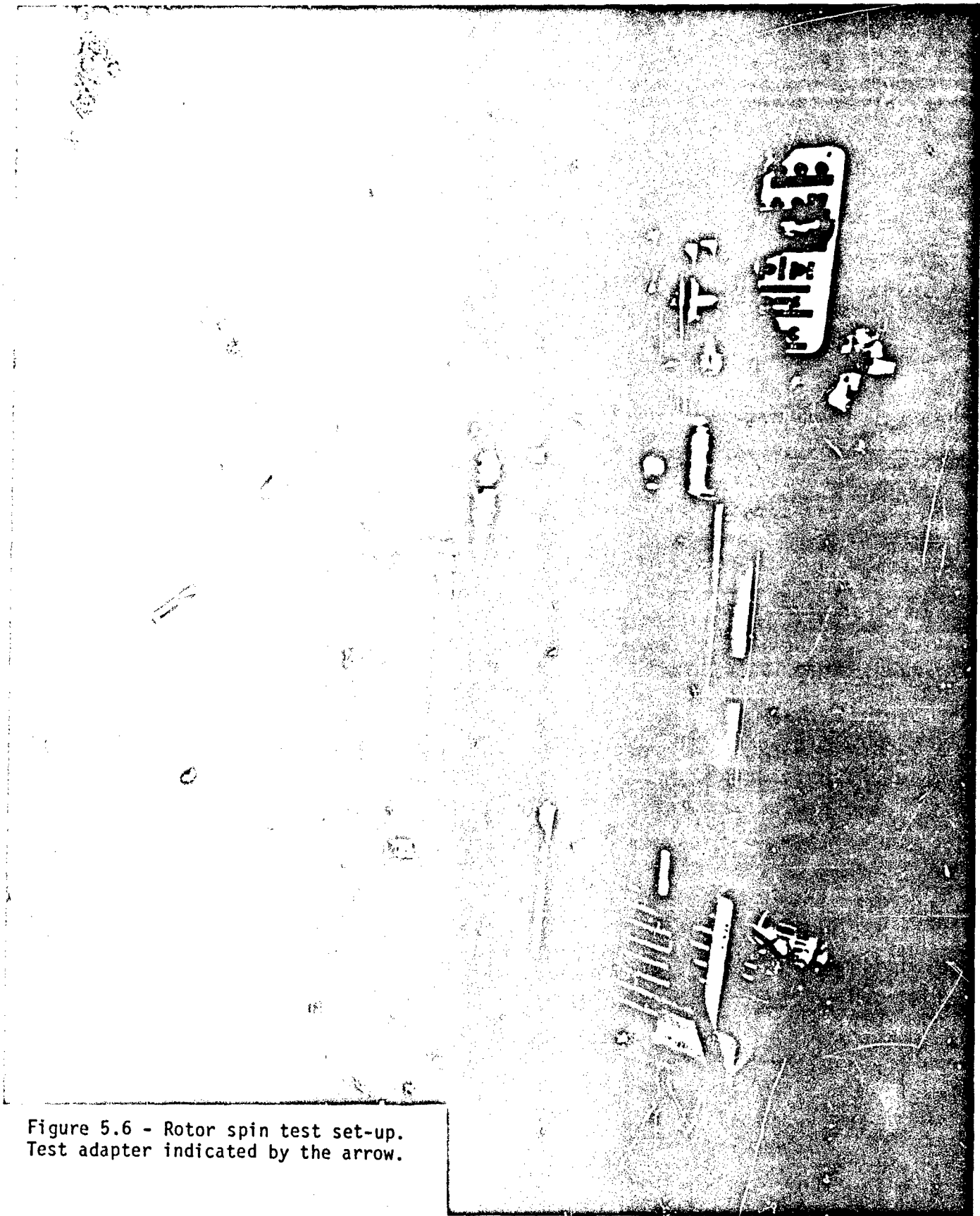Figure 5.5 - Spin test assembly. Rotor is housed in a partially machine stator frame.

117

Figure 5.6 - Rotor spin test set-up.
Test adapter indicated by the arrow.

The drive stand was accelerated at a very slow rate and the accelerometer output was monitored to detect any resonance. No resonances occurred and the rotor speed was increased to and maintained at 26,250 rpm. The air gap temperature was varied between 85°C and 150°C for the first few hours to detect any changes in rotor stability. Variations in the air temperature were made by adjusting the oil flow rates and the inlet temperatures. The air gap temperature was then maintained at 175°C, the maximum temperature expected during generator operation, and the rotor was operated for 50 hours at maximum speed. During this time, no change in rotor condition was detected and the anti-drive end vibration level was approximately 3 G's. After 50 hours of operation, the rotor speed was increased to 28,875 rpm and maintained for 5 minutes. The rotor was very stable at this overspeed condition and the vibration level was approximately 4.5 G's. At the end of five minutes, the rotor speed was reduced to 26,250 rpm and the vibration level dropped to the previous value of 3 G's. This condition was maintained for 2 hours to detect any changes but none occurred. The spin test data is presented in Appendix A.

In summary, a total of 64 hours of testing was accomplished at maximum speed and varying temperature. At the conclusion of the test, the rotor was disassembled and checked for changes in dimensions and balance. No changes were found confirming the integrity of the containment structure.

5.4 STATOR FABRICATION AND GENERATOR ASSEMBLY

Since all the rotor components and the end bells had been fabricated in the previous phase, only the wound stator was required to complete the generator assembly.

The stator core was fabricated from 0.006" laminations of vanadium-cobalt iron, an alloy commonly known as permendur. This alloy, with proper processing, permitted operation at substantially

higher flux density with lower magnetizing current than conventional
magnetic steels thereby reducing the electromagnetic weight. The
0.006" thickness was selected to minimize eddy current losses at
high operation frequencies.

Figure 5.7 shows the construction of the laminations. Approx-
imately 460 laminations were stacked to produce the 2.88 in. stack
length which corresponded to a 0.98 stacking factor. These lami-
nations were bonded together and held in the stacking fixture while
their outside diameter was ground to the specified dimension. After
machining, these laminations were dropped inside the core sleeve.

The slot configuration is shown in Figure 5.8. The conductors
are number 24 round copper wires coated with heavy polyimide insulation.
The HML coating is used to enhance the phase-to-phase and phase-to-
ground capability. The coil turns are wound in strands to reduce the
skin effect. The strands are transposed in the end turns such that
top positioned conductors leaving the slot are transposed such that
they become bottom positioned before entering the next slot. This
transposition has the effect of cancelling the strand to strand vol-
tages generated in the slot and, thus, reducing the deep bar losses.

The slot liner used was a 0.008" thick Nomex composite selected
because of its good thermal properties. A 0.008" phase separator was
also used for enhanced phase-to-phase insulation reliability. The top
stick was made from laminated polyimide and had a 0.026" thickness.
The completed stator winding was impregnated with General Electric
novolac compound applied by a vacuum pressure process. This compound
when vacuum applied insured a maximum slot fill and improved heat
transfer from the windings to the core and hence to the cooling oil.
Two views of the wound core are shown in Figures 5.9 and 5.10.
Finally, the wound core was fitted inside the stator frame.

120

5.713⌀ AT CL
5.707⌀ OF SLOTS

.015
.005

5.091⌀
5.089⌀

(.310)

.005 R
MAX

60 SLOTS EQ SP

.12
.08
1 NOTCH

FLAT BOTTOM

6.103⌀
6.097⌀
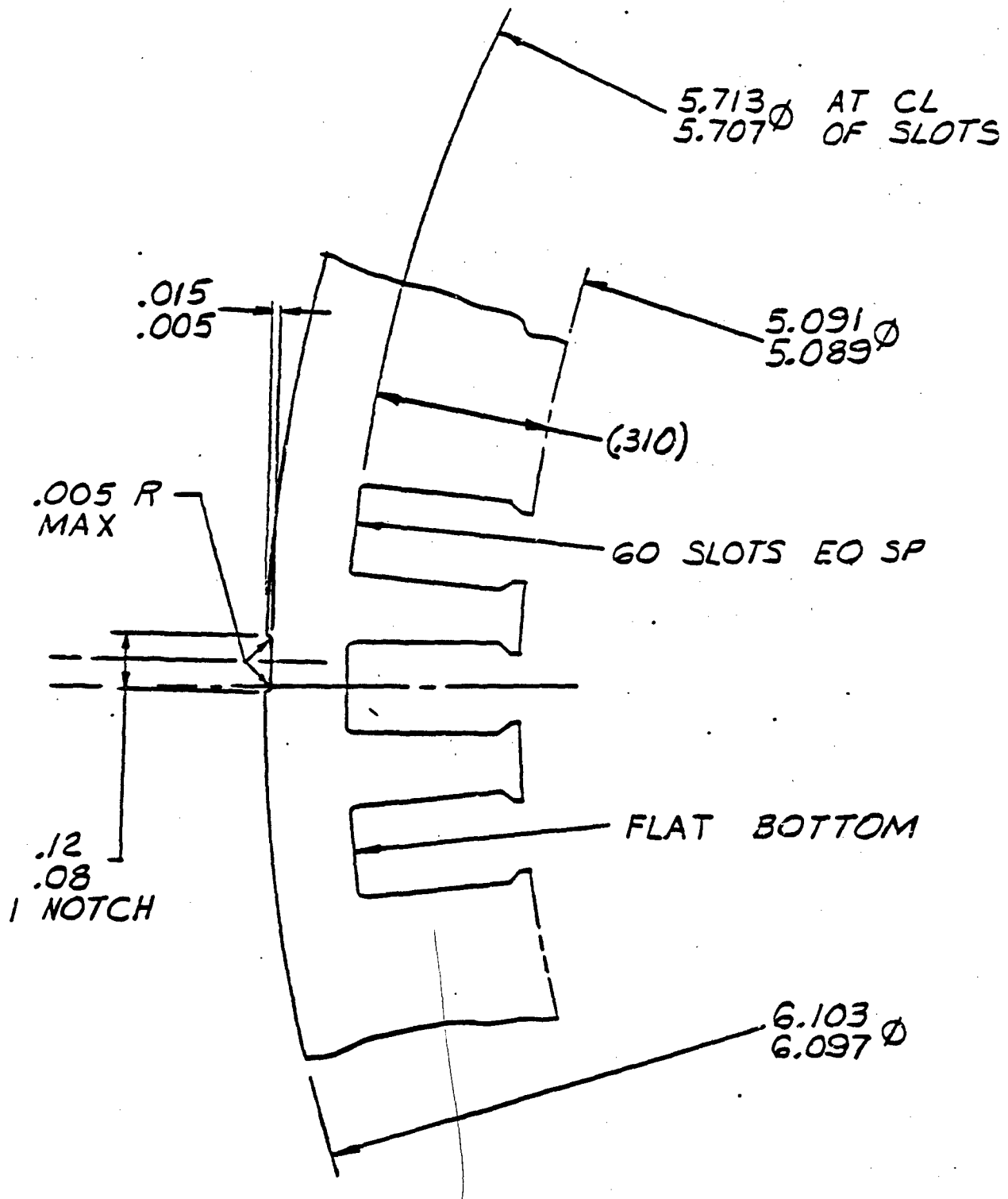
Figure 5.7 - Construction of the stator laminations

121

TOP STICK
MAT'L: POLYIMIDE, LAMINATED
0.026" THICK

SLOT LINER
MAT'L: NOMEX COMPOSITE
0.008" THICK

ROUND WIRE
MAT'L: COPPER
0.0201" DIA.

PHASE SEPARATOR
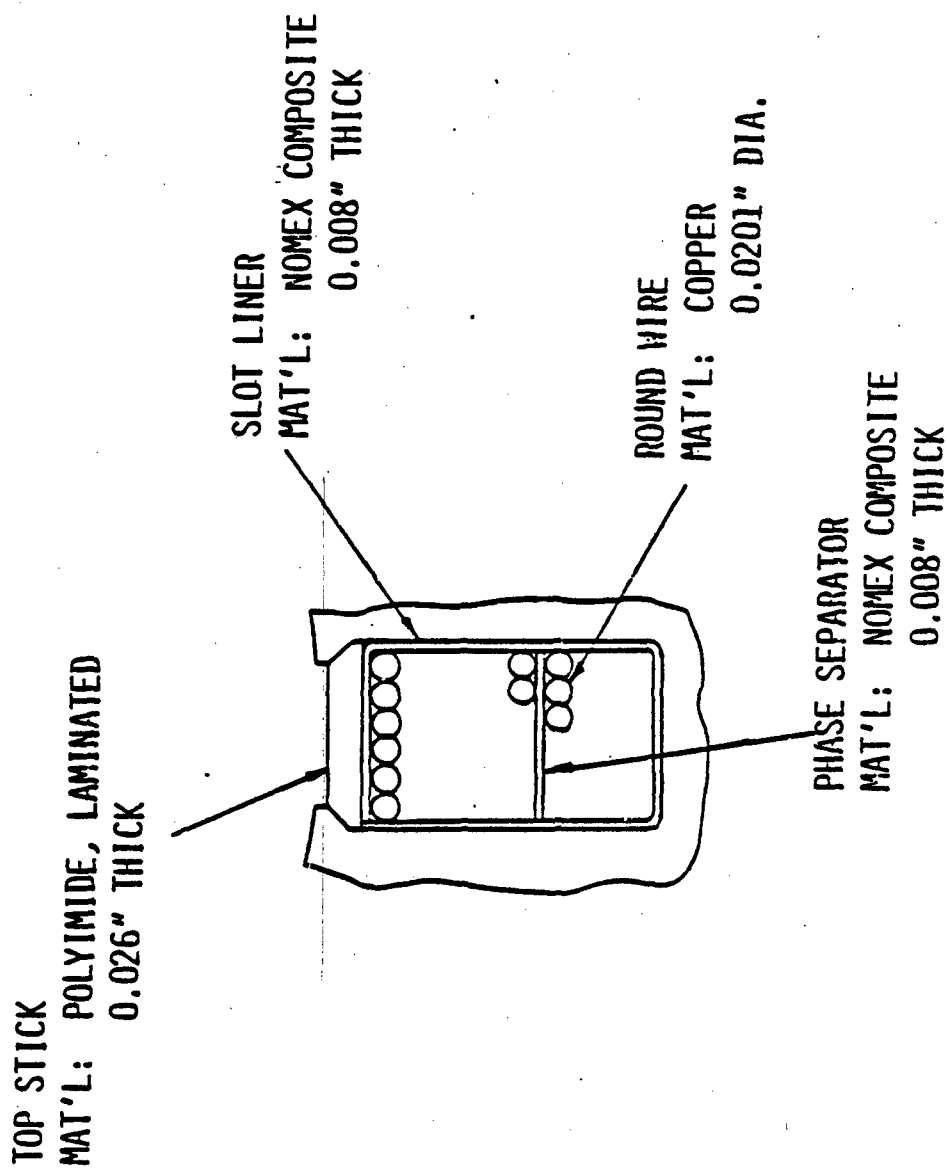MAT'L: NOMEX COMPOSITE
0.008" THICK

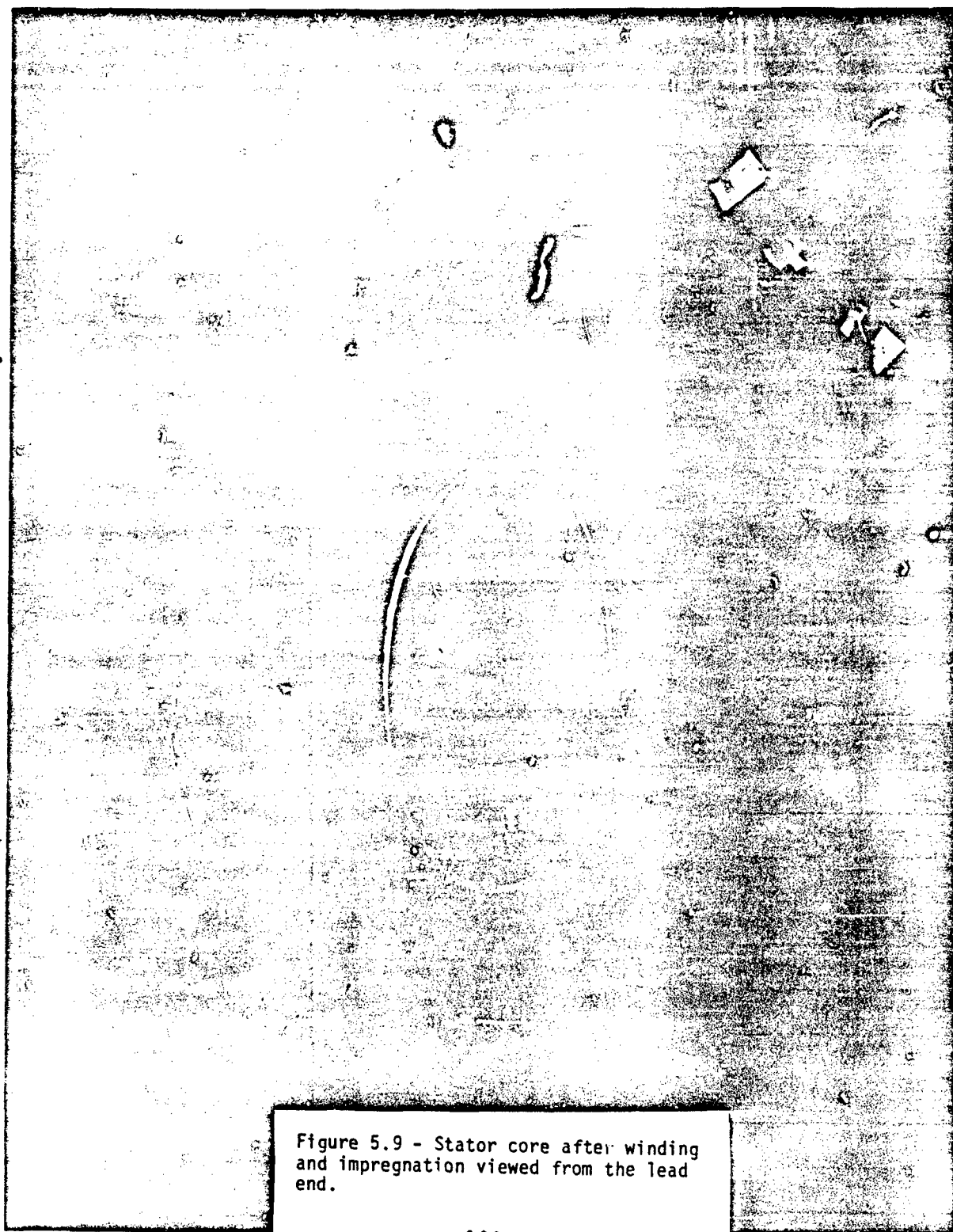Figure 5.8 - Stator slot configuration showing the insulation details

122

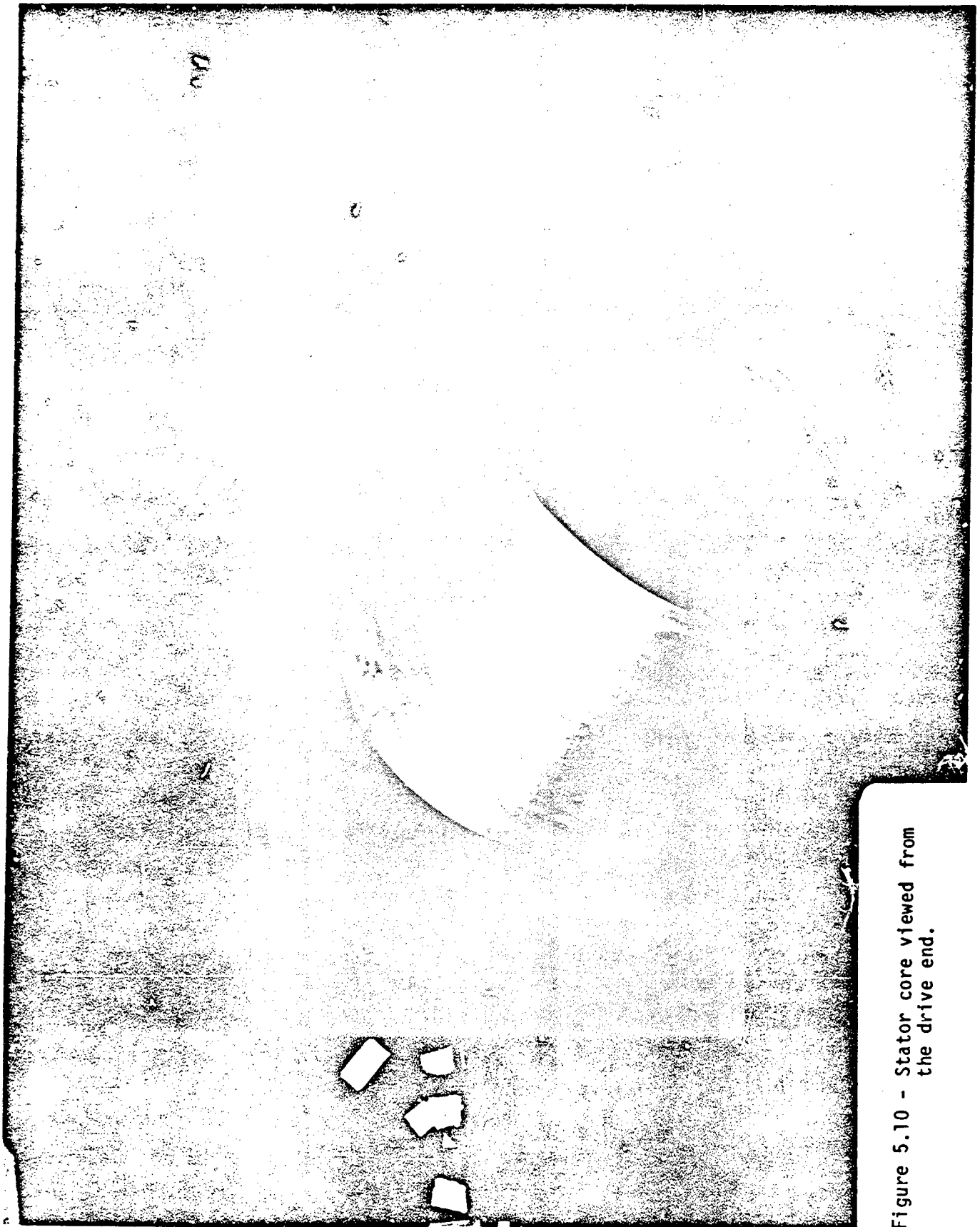Figure 5.9 - Stator core after winding and impregnation viewed from the lead end.

Figure 5.10 - Stator core viewed from the drive end.

DISCONNECT

Since the permanent magnets provide a continuous excitation a mechanical disconnect was required to disengage the generator from its drive. This disconnect was located in the cavity between the mounting pad and the drive end bell and comprised of the following parts:

o a solenoid which when excited by a 24 volt signal retracts the pin that holds the pawl in place.

o a pawl, shown in Figure 5.11, which is mounted on a rod and pivots about it. This pawl is under a constant spring force pulling it towards the shaft but, in the normal state, is restrained by the solenoid pin.

o a disconnect shaft which also serves as the input shaft and is splined at both ends. This shaft has two shear section on either side of the cam.

When the solenoid is energized by a 24 volt DC signal, the pin holding the pawl is retracted. The pawl then swings down, because of the spring action, and strikes the face of the cam on the input shaft. This causes the shaft to shear on the two planes on either side of the cam thus disengaging the generator from the drive. While the generator coasts down after disconnect, the drive can keep on rotating with the sheared sections held in place by the rod inside the stub shaft. The sheared shaft is shown in Figures 5.12 and 5.13.

To reset the disconnect mechanism, the generator is first backed off from the mounting pad and the sheared output shaft removed. The pawl is lifted upwards till the solenoid pin drops back in and holds it in place. The stub shaft is then replaced and properly positioned.
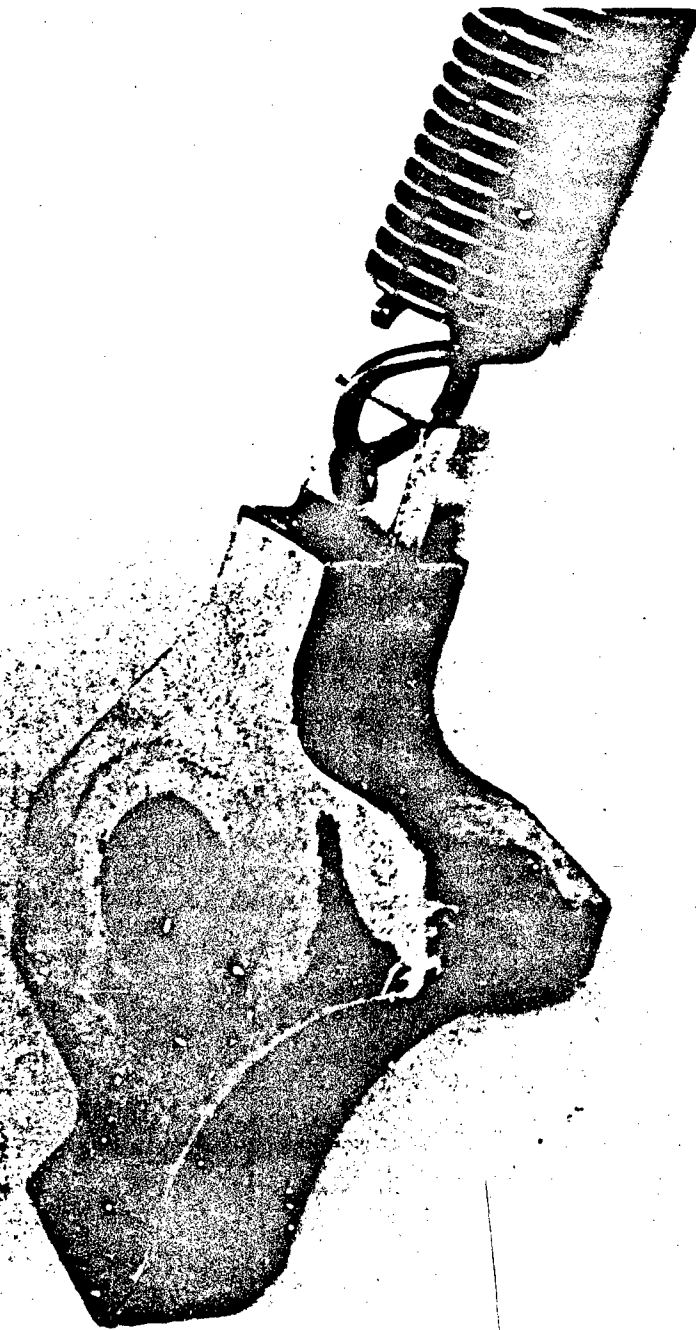
125

Figure 5.11 - Pawl used in the dis-
connect mechanism.

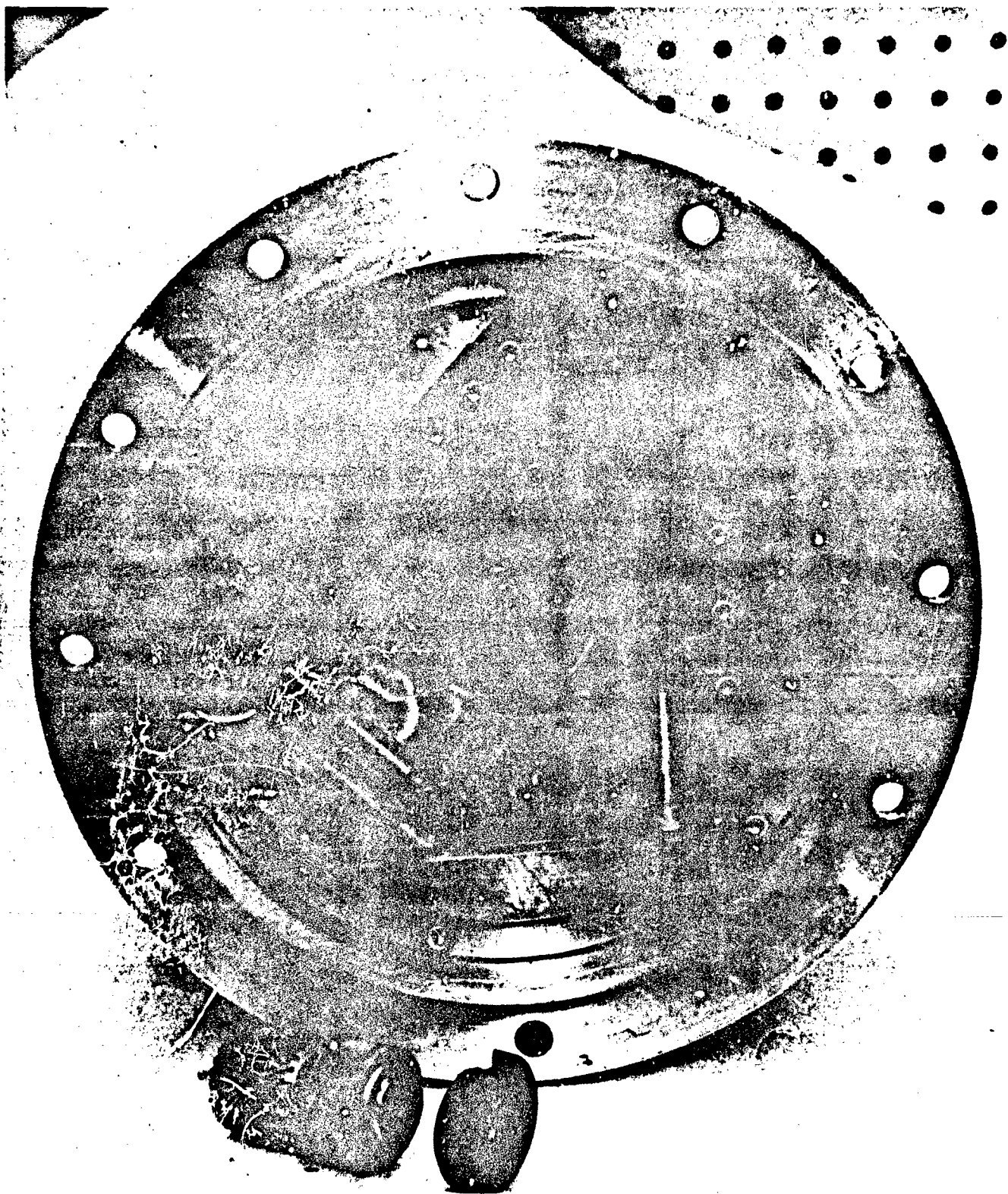Figure 5.12 - Input shaft shown after
disconnect.

127

Figure 5.13 - View of the disconnect
cavity after actuation of the mechanism.

128

5.5   GENERATOR WEIGHT ANALYSIS

The weight breakdown of the generator package is as follows:

Rotor:

Discs with end plates	13.20 lbs.	
Shaft	3.46 lbs.	
Inner shaft	1.20 lbs.	
Rotor hardware	0.58 lbs.	
Total		18.4+ lbs.

Stator:

Core with windings and leads	8.31 lbs.	
Stator frame	2.50 lbs.	
Stator hadware	0.91 lbs.	
Total		11.00 lbs.

Assembly Components:

End bells	3.73 lbs.	
Bearings	0.74 lbs.	
Seals	0.50 lbs.	
Clamps	0.46 lbs.	
Supports	0.90 lbs.	
Stub shaft	0.95 lbs.	
Misc. hardware	0.53 lbs.	
Total		7.81 lbs.

Generator Weight: 37.25 lbs.

Disconnect:

Plate	1.02 lbs.	
Solenoid	0.40 lbs.	
Hardware	0.83 lbs.	
Total		2.25 lbs.

Total Generator Package: 39.5 lbs.

The total generator package has not been optimized from a weight standpoint and, thus, substantial weight reduction is possible through more efficient packaging of components. The physical dimensions of the converter are estimated as follows:

Size	11" x 5" x 17"
Weigth	38 lbs.

Thus the system weight would be approximately 75 lbs. or about 1.4 lbs./KVA.

5.6 GENERATOR TEST PLAN

Prior to the testing of the generator, a test procedure was written per paragraph 4.0 of MIL-E-23001. Since only tests applicable to the generator were to be accomplished, the following items were identified:

o <u>Dielectric test</u>: The generator shall withstand the following 60 Hz RMS voltages when hot as a result of operating at rated load.

solenoid - 500 V for 1 minute or 600 V for 1 second to ground

stator winding - 1640 V for 1 minute or 1970 V for 1 second to ground

o <u>Heating and Overload</u>: With minimum rated rpm and maximum oil temperature, the generator shall operate at 1 PU and 0.75-0.95 pf. The generator will also be required to produce 1.5 PU for 5 minutes and 2 PU for 5 seconds at the above speed.

o <u>Heat rejection</u>: The rate of heat rejection to the cooling oil will be recorded at various shaft speeds and used as an alternate approach for determining generator efficiency.

o <u>Factors affecting voltage</u>: The generator voltage will be recorded with the cooling oil temperature varied between 25°C and 80°C and the generator operated at no load, ½ PU and 1 PU.

o <u>Operation of protective devices</u>: The shaft shear disconnect will be operated at 26,250 rpm to demonstrate its capability of decoupling the generator from the drive mechanism. The disconnect shall be actuated immediately upon application of 24 volts to the solenoid.

o <u>Performance and endurance</u>: The generator shall be demonstrated to operate failure free for 25 hours during which the shaft speed and load will be varied. Also included as part of this test will

be the overload conditions as follows:

a) with the generator stabilized at minimum rpm, the generator shall be operated at 1.5 PU for five minutes.

b) with the generator stabilized at minimum rpm, the generator shall be operated at 2.0 PU for five seconds.

o Commutating inductance: The commutating inductance of the generator will be measured using both the bridge method and the notch method.

o Harmonic content: The harmonic content of the generator will be measured at 15300 rpm for no load, ½ PU and 1 PU conditions.

5.7   GENERATOR TESTING

5.7.1 Test Set-Up

For the purposes of this test, the generator was assembled inside the test frame and mounted on the drive stand. The set up shown in Figure 5.14 was identical to the one used during the rotor spin test. Thus, stator and rotor oil flows, pressures and temperatures could be controlled independently. The accelerometer, mounted on the anti-drive end recorded the vibration level and was monitored to detect any resonances. Two iron constantan thermocouples were potted, diametrically opposite to one another, in the stator end turn area. The test frame was wrapped with insulation to prevent heat loss to the atmosphere which enabled the generator losses to be estimated from the oil temperature rise. The limits established for the test were as follows:

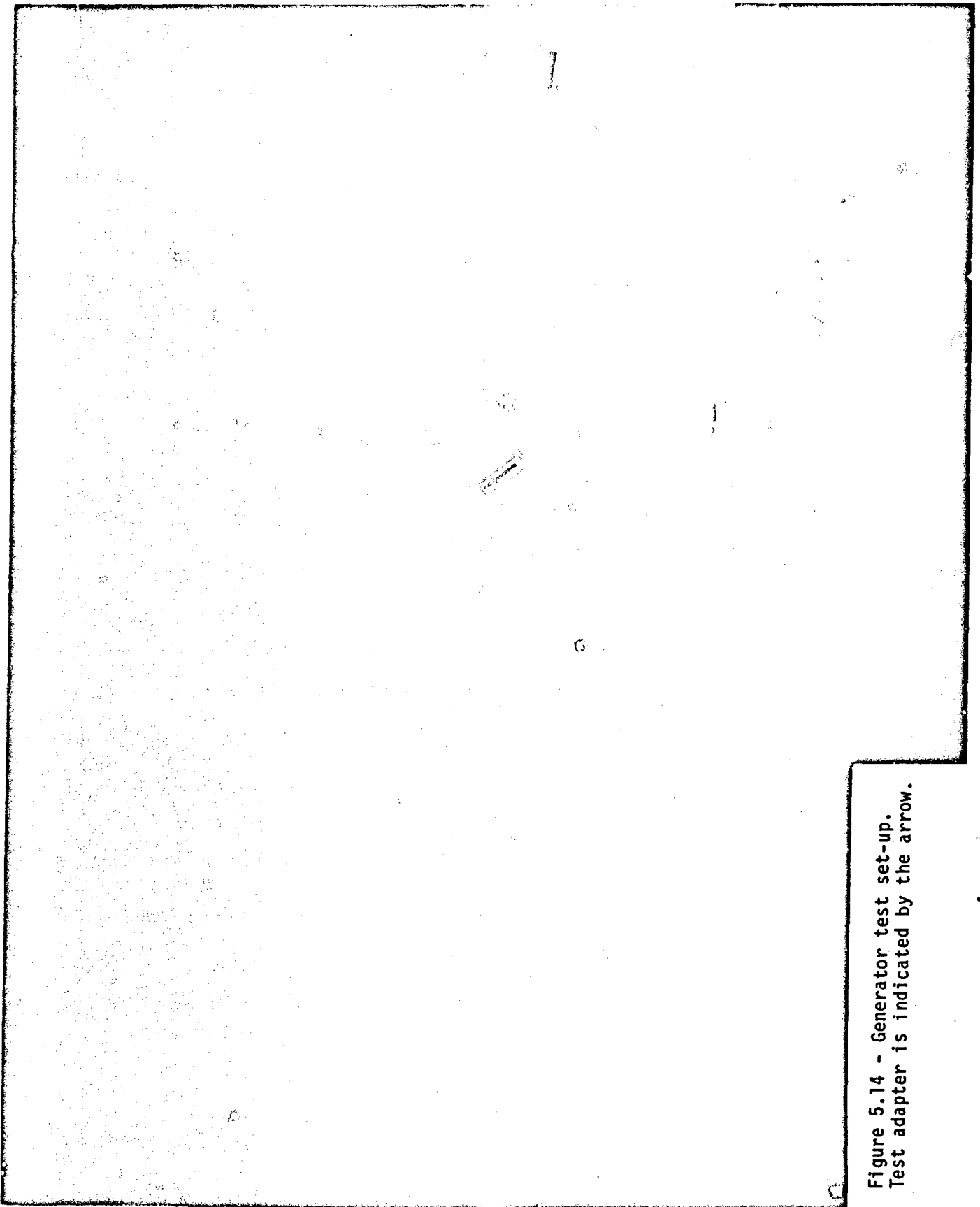|	
maximum vibration at anti-drive end	10 g's
maximum stator winding temperature	250°C
maximum rotor speed	29,000 rpm
maximum oil inlet temperature	85°C

131

Figure 5.14 - Generator test set-up.
Test adapter is indicated by the arrow.

The various ratings used for the generator tests are given in
Table 5.1.

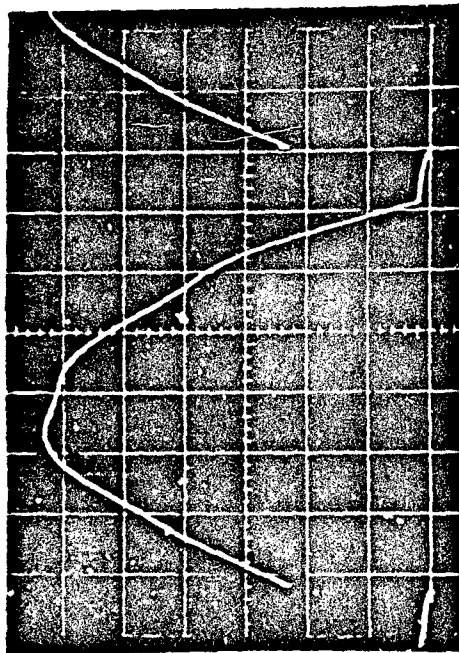| LOAD	PHASE CURRENT	GEN. PF
0 PU	27A	0.1
½PU	40A	0.75
1 PU	47A	0.74
1 PU	57A	0.76
1½PU	53A	0.74
1½PU	63A	0.78
2 PU	74A	0.74
2 PU	83A	0.83

Table 5.1. Generator Ratings

The results of the tests are described below.

5.7.2 Commutating Inductance

The saturated inductance of the stator windings was measured
using a general RLC bridge. The individual phase inductance measure-
ments were taken with the rotor in the direct axis as well as in the
quadrature axis. Thus, the high and the low values of the inductance
were recorded for each phase and are as follows:

STATOR PHASES	L-L INDUCTANCE	
	MIN.	MAX.
1-3	67.5	90.5
3-5	67.5	90.5
5-1	67.5	90.5
2-4	67.5	90.5
4-6	68.5	91.5
6-2	68.5	91.5

I = 15.1 Amps Dc
N = 2734 RPM
Scale: V - 5V/cm
       H - 200 sec/cm

I = 27.9 Amps DC
N = 5300 RPM
Scale: V - 10 V/cm
       H - 100 sec/cm

Figure 5.15 - Oscilloscope pictures to determine commutating
   inductance using a half-rectified bridge.

From these values, the commutating inductance per phase was deter-
mined to be 39.6 uH. Considering a saturation factor of 1.2, this
correlates very well with the predicted value of 47 uH.

The commutating inductance was also measured using the half
rectified bridge approach, commonly referred to as the notch method.
The inductance value calculated from the oscilloscope pictures,
shown in Figure 5-15, was 38.7 uH. Thus, both the bridge and the
notch methods yielded approximately the same inductance value as
expected.

5.7.3 Harmonic Content

The voltage waveforms were photographed and the harmonic
content analyzed at base speed (15,300 rpm) and NL, ½ PU and 1 PU
condition. The higher order harmonics were very low and the maximum
value of the 5th harmonic was measured as 1.2% of the fundamental at
no load. The voltage waveform improved as the load was increased
and virtually no ripple could be seen at full load (Figure 5.16). The
harmonic content analysis is given in Table 5.2.

HARMONIC	FREQUENCY	NO LOAD	½ PU 45.77 KVA	1 PU 52.23 KVA	1 PU 61.32 KVA
1	1275	100	100	100	100
3	2825	4	3.5	3.4	4.0
5	6375	1.2	0.6	0.5	0.5
7	8925	0.4	0.2	0.3	0.4
9	11475	1.0	0.6	0.6	0.6
11	14025	0.8	0.3	0.3	0.3
13	16575	0.6	0.1	0.1	0.2
15	19125	0.1	-	-	-
23	29325	0.1	-	-	-
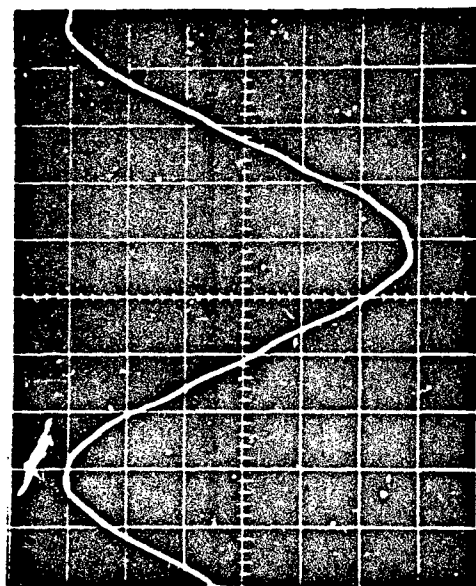
½ PU @ 0.75 PF

1 PU @ 0.76 PF

N = 15,300 RPM
Scale:
V - 100 V/cm
H - 0.1 msec/cm

No Load
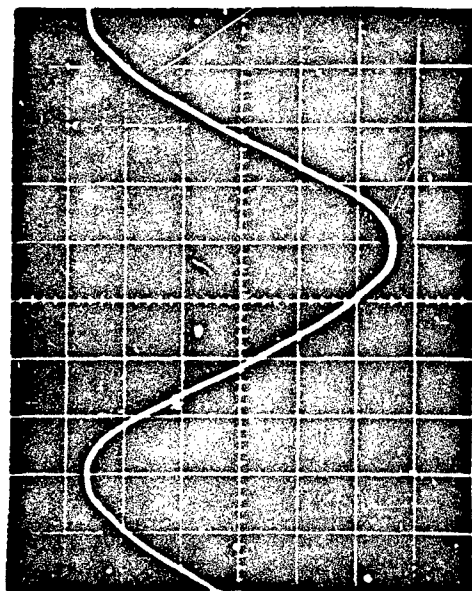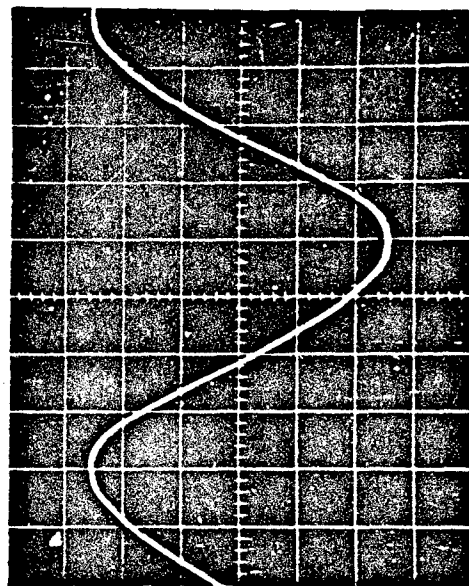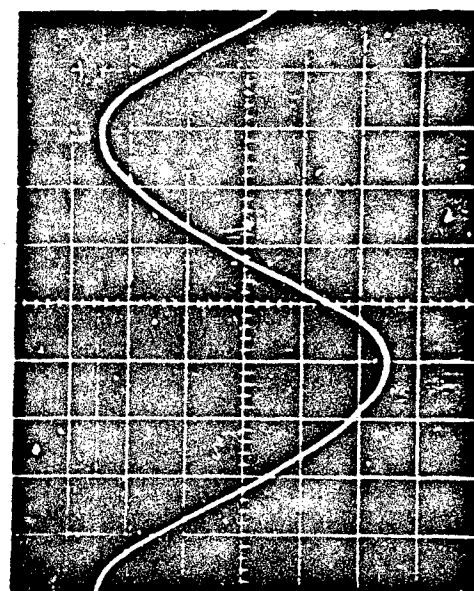
1 PU @ 0.74 PF

Figure 5.16 - Voltage waveforms at different load conditions.

136

5.7.4   Generator Efficiency

The input power to the generator was measured using a 100 in-lb torque tube. No readings could be taken above 21,000 rpm because of excessive vibration induced by the torque tube extension. The efficiency data is as follows:

SPEED	GEN. KVA	PF	GEN. KW	INPUT KW	EFF.
15,300	45.6	.757	34.5	36.8	0.94
15,300	52.2	.742	38.8	41.1	0.94
15.300	61.1	.766	46.8	50.2	0.93

The losses determined from the torque tube readings were verified by calculations using the cooling oil temperature rise.

5.7.5   Endurance Testing

A 30 hour endurance test was conducted according to Table 5.3. During the test, the load, oil temperature and speed were continuously varied and the following measurements were recorded:

i)	stator pressure - inlet and exit
ii)	stator temperature - inlet and exit
iii)	stator flow
iv)	rotor pressure - inlet and exit
v)	rotor temperature - inlet and exit
vi)	rotor flow
vii)	vibration at the anti-drive end
viii)	generator L-N volts
ix)	generator amps
x)	power factor
xi)	stator end turn temperature

The performance curve for the generator is plotted in Figure 5.17. Also shown in dotted are the calculated values based on a 21 MGOe magnet strength and a 250°C magnet temperature. Since the actual operating temperature was lower, the output of the generator was substantially improved. At the design point, 2 PU at base speed, the output voltage was 156.3 volts whereas the specification requirement was 149.2 volts. In short, the generator met all performance requirements.

ELECTRICAL PERFORMANCE

26,250 RPM

15,300 RPM

L-N Voltage

350

300

250

200

150

100

50

Actual Data
Theoretical

0   10   20   30   40   50   60   70   80   90
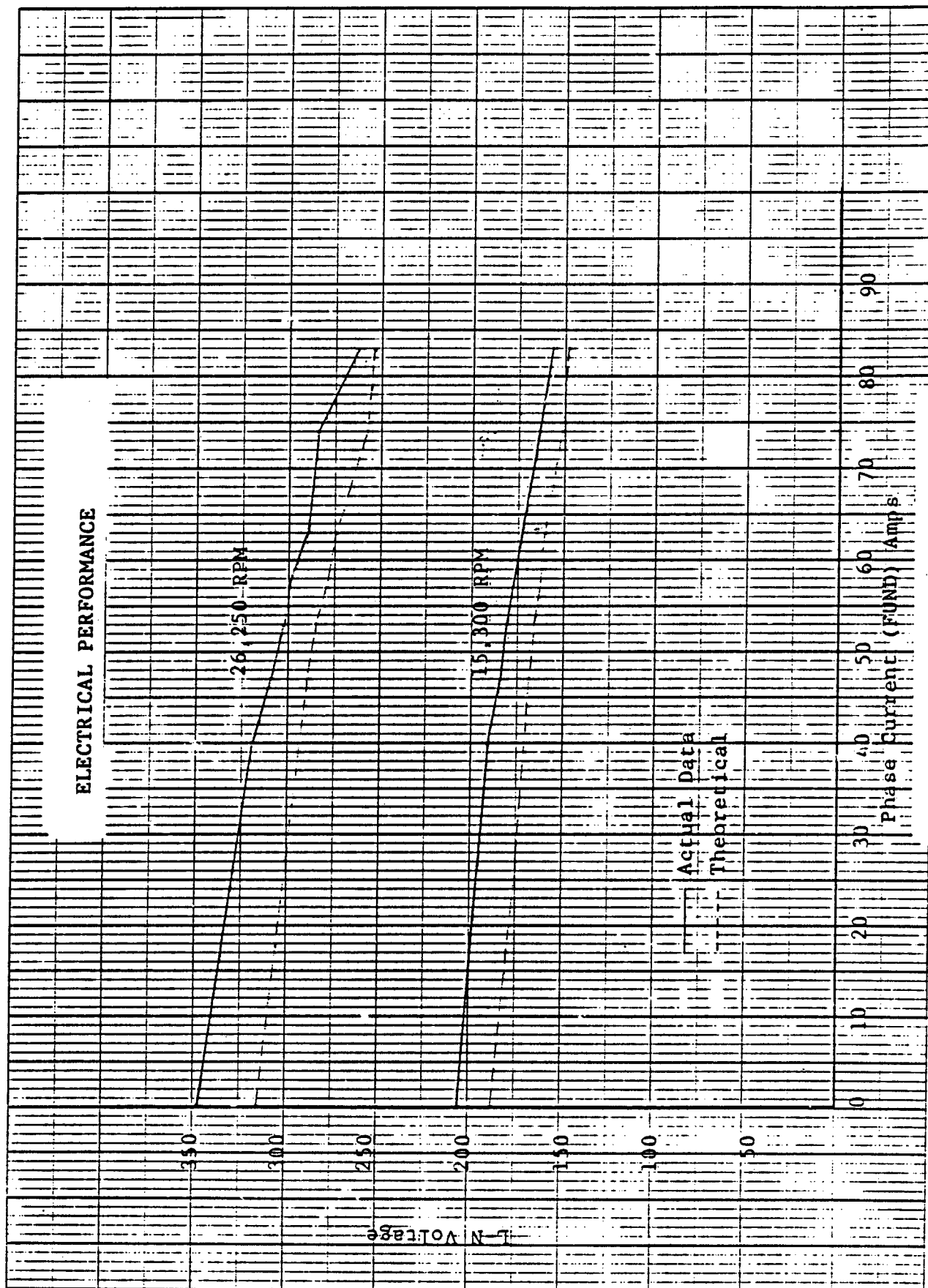
Phase Current (FUND) Amps.

Figure 5.17 - Performance curve.

The no load voltage is plotted as a function of speed in Figure 5.18. The maximum value is approximately 350 volts which corresponds to a line-to-line voltage of 700 volts. Assuming a 40% margin for harmonic content and waveform distortion peaks, the line-to-line voltage will be approximately 980 volts which is well within the operational limit of the SCR's in the cycloconverter.

The oil inlet temperature was varied between 25°C and 80°C and the change in generator voltage recorded. At no load condition, the generator voltage decreased by approximately 2 volts. This rather small change in generator voltage is due to the operating temperature being in a range where no substantial derating of the magnet takes place.

While the machine was hot due to operation at full load, a dielectric test was performed. The stator windings were subject to 1970 volts for 1 second and the solenoid coil was subjected to 600 volts. Both the windings and the solenoid passed this test and further testing of the generator was continued.

During the endurance testing, the themocouple readings were monitored and the stator end turn temperatures recorded. The thermocouples had an inherent lag which was found by putting direct current in the windings and noting the thermocouple readings. This lag was determined to be about 20°C and thus the temperatures recorded in actual test were accordingly adjusted. Table 5.3 compares the actual copper temperatures to the predicted values at three data points taken at base speed and 80°C oil inlet temperature.

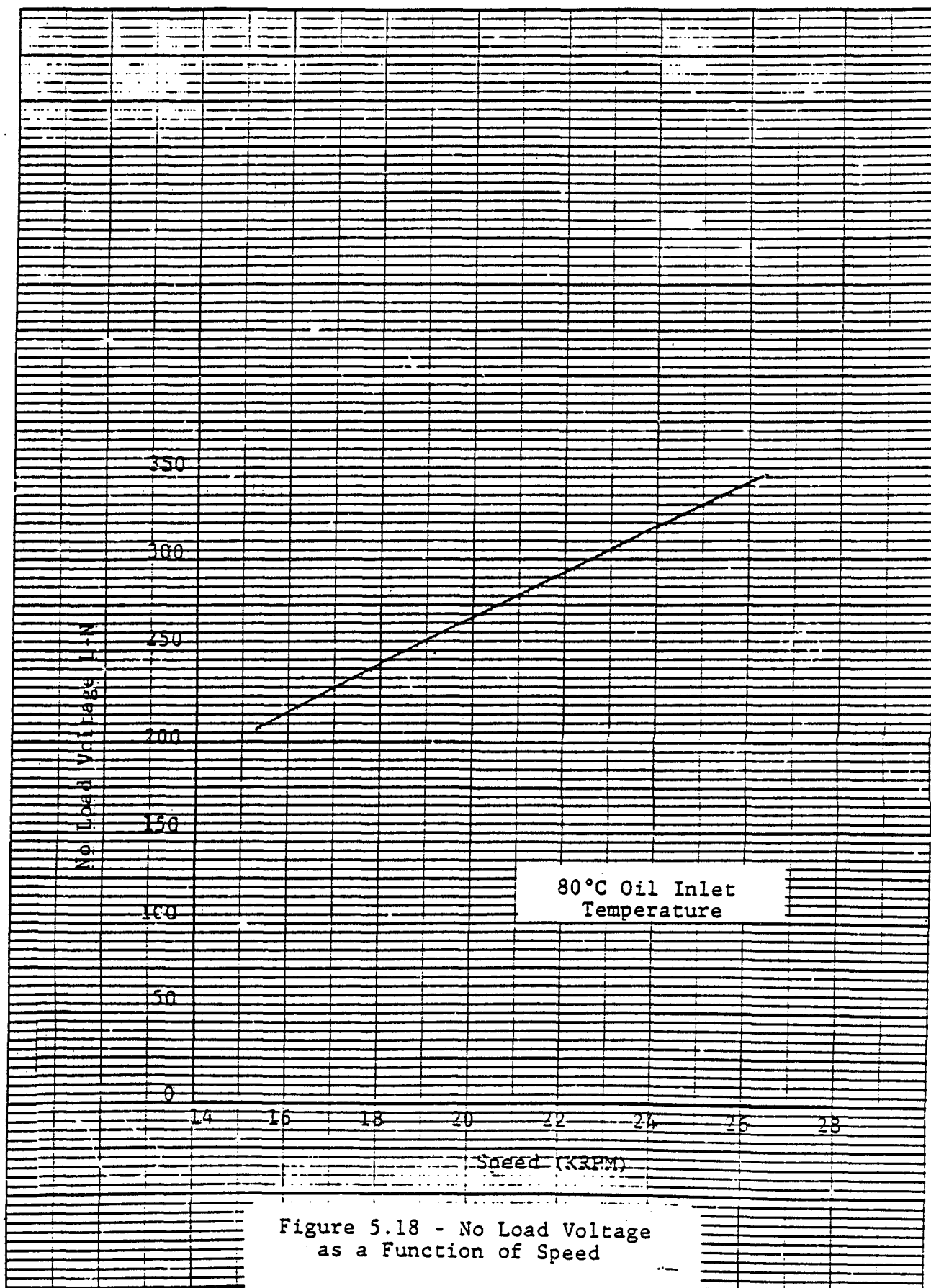| GEN. KW	PREDICTED LOSSES KW	ACTUAL LOSSES	PREDICTED CU TEMP. °C	ACTUAL ADJ. CU TEMP.
46.79	3.52	3.39	150	129
38.76	3.14	2.37	132	121
34.53	2.79	2.26	120	115

Table 5.3. Generator Losses and Copper Temperatures

Figure 5.18 - No Load Voltage
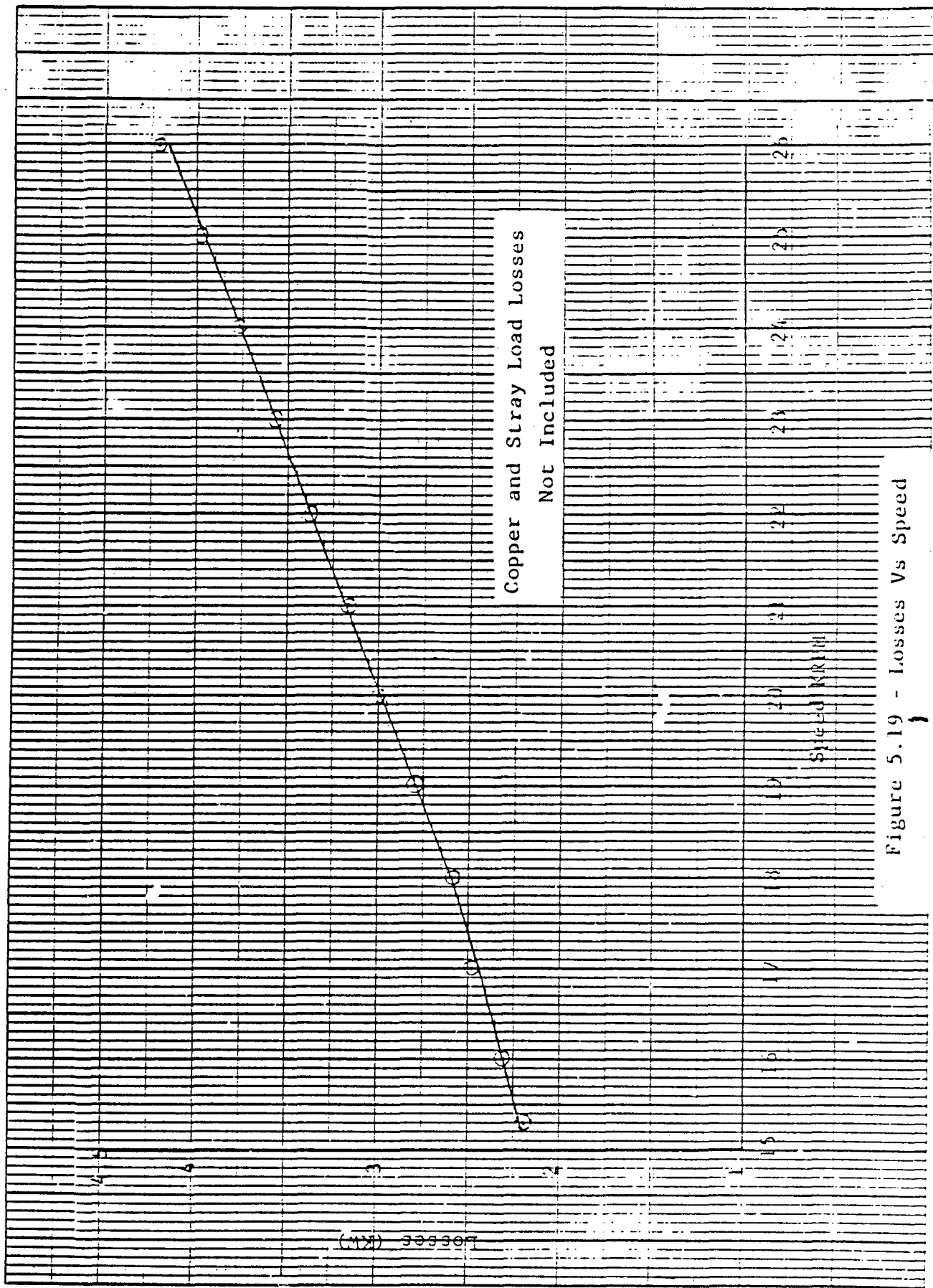as a Function of Speed

Figure 5.19 - Losses Vs Speed

141

Figure 5.19 shows a plot of core loss, pole face loss and friction and windage loss as a function of speed.

5.7.6 Disconnect

With the generator operating at maximum speed (26,250 rpm) the solenoid was energized. The pawl came down and struck the face of the cam causing a shearing of the input shaft. Thus, the generator was disengaged from the drive within 50 milliseconds as expected. The generator was removed from the drive stand for replacement of the sheared shaft and the resetting of the disconnec mechanism.

5.8   SUMMARY

In summary, the generator was tested over the entire spectru of speed and load conditions for over 50 hours. No problems were en countered during this testing and the generator met all the sytem interface requirements. The efficiency of the generator was deter- mined to be 94% at base speed and 1 PU load. The winding temperatur as recorded, correlated well with the theoretical prediction. This confirmed the calculated values of electromagnetic and mechanical losses.